Non–equilibrium Dynamics in Lattice Systems: Epitaxial Growth and Time dependent Density Functional Theory

Dissertation
zur Erlangung des akademischen Grades
des Doktors der Naturwissenschaften (Dr. rer. nat.)
an der Universität Konstanz
Fachbereich Physik

vorgelegt von

Stefan Heinrichs

Dissertation der Universität Konstanz

Datum der mündlichen Prüfung: x.10.2005

Referenten: Prof. Dr. P. Maaß
Prof. Dr. W. Dieterich

Contents

1 Introduction **1**

I Epitaxial Growth **5**

2 Basic quantities and concepts **7**
2.1 Molecular Beam Epitaxy 7
2.2 Atomistic processes in thin film growth 7
2.3 Nucleation in the first layer 9
2.3.1 Island densities 9
2.3.2 Island size distribution 11

3 Second layer nucleation **13**
3.1 Introduction 13
3.2 Kinetic Monte Carlo Simulations 15
3.2.1 Multi-island model 16
3.2.2 Single-island model 19
3.2.3 Equivalence of single-island and multi-island models 20
3.3 TDT Approach 22
3.4 Stochastic description 24
3.4.1 Fundamental quantities 25
3.4.2 Nucleation Rates 29
3.4.3 Small critical nuclei ($i=1,2$) 31
3.4.4 Large critical nuclei ($i\geq 3$) 36
3.5 Rate equation theory 39
3.5.1 General Procedure 39
3.5.2 Negligible Lifetimes of Unstable Clusters 41
3.6 Second layer nucleation with interactions 47
3.6.1 Metastable clusters 47
3.6.2 Ring barriers 50
3.6.3 Implications for Experiments 53
3.6.4 Case study: Ag/Pt(111) 55
3.7 Applications 57
3.8 Summary and Discussion 59

4 Growth of binary alloys **61**
4.1 Motivation . . . 61
4.2 Experiments . . . 61
4.3 Simulation Model . . . 63
4.3.1 Chemical interactions . . . 63
4.3.2 Kinetic parameters . . . 65
4.3.3 Exchange Processes . . . 66
4.3.4 Implementation . . . 66
4.4 Connection between structural order and magnetic properties . . . 67
4.4.1 Parameters for the bond anisotropy constants . . . 69
4.5 Simulation results for nanoclusters . . . 70
4.5.1 Anisotropy parameters . . . 70
4.5.2 Cluster shape . . . 71
4.5.3 Surface segregation . . . 74
4.5.4 Dipolar Interaction energy and total anisotropy . . . 76
4.5.5 $L1_2$ order parameter . . . 79
4.5.6 Layer resolved analysis . . . 81
4.5.7 Ensemble fluctuations of parameters . . . 82
4.5.8 Details of the growth process . . . 83
4.6 Summary and Discussion . . . 86

II TDFT **89**

5 Time Dependent Density Functional Theory **91**
5.1 Introduction . . . 91
5.2 DFT for Lattice Gases with Internal Degrees of Freedom . . . 92
5.3 Application to the 1D Potts model . . . 94
5.3.1 Exact density functional . . . 94
5.3.2 Mean spherical approximation (MSA) . . . 95
5.3.3 Kinetics of density profiles . . . 98
5.4 Basic Limitations of TDFT . . . 101
5.5 Summary and Discussion . . . 103

6 Summary and Outlook **105**

A Rates of Processes in second layer nucleation **109**
A.1 Encounter rates $\omega_n(R)$ . . . 109
A.2 Lifetime $\tau_n(R)$ . . . 110

B Continuous–Time Monte–Carlo simulations **117**
B.1 General description . . . 117
B.2 Implementation for 3d growth . . . 119

C Fundamentals of Density Functional Theory **121**

Bibliography **123**

1 Introduction

Structures of nanoscale dimensions open a wide field of new physics and materials with novel properties. In particular, self-organized structure formation by deposition of metals on surfaces has received much attention recently because the interplay of diffusion, aggregation, deposition, segregation and superlattice ordering yields a rich variety of phenomena. The resulting structures are usually frozen-in and metastable which is good on one hand, since it allows more latitude in tailoring materials for specific needs because extra dynamic parameters come into play which may be tweaked, but at the same time makes a theoretical description harder.

An important case is the process of molecular beam epitaxy (MBE), where atoms attach to a cleaned surface exposed to a small flux of atoms in ultra-high vacuum. Atoms move to potential minima of the surface located at lattice sites and can perform thermally activated jumps to neighboring sites. The separation of timescales of vibration at a specific lattice site from the one for the hopping process, allows for a description based on the hopping processes alone[HTB90]. The transition rates are provided by more microscopic theories such as molecular dynamics simulations or density functional theory (DFT)[**review**], or complementary, by experiments. This work deals with timescales much longer than the individual processes so that the collective properties of many atoms can be studied as they form structures. Description of the growth process can proceed on different levels of detail. The most microscopic method used in this work is to follow the individual jumps of atoms in the framework of Kinetic Monte–Carlo (KMC) simulations[**review**], which generates possible realizations of the dynamics and is exact for a given set of microscopic rates. The KMC method serves as a reference for testing the validity of less microscopic methods, which are usually much less computationally intensive and may provide more physical insight.

The first stage of structure formation in MBE usually proceeds by the assembly of two-dimensional islands composed of adsorbate atoms on the substrate. For this nucleation in the first layer, mean field theories successfully describe important quantities, such as the island density[Bru98, MK04]. They are summarized in sec. 2. The parameters in these theories are the densities of islands of various sizes which are coupled by differential equations describing deposition, diffusion and attachment. An important question during further growth is, whether the resulting surface morphology is smooth, which is the case when islands coalesce before layer completion, or becomes rough when nuclei form on top of islands

so that three dimensional clusters result. Nucleation in the second layer differs from nucleation in the first layer because of the confined geometry as encountered on top of a growing island. In addition, more parameters enter in the form of the energy barrier needed to overcome the step edge. With the limited effective system size in the confined geometry, fluctuations in the number of atoms on top of an island can become important and the mean field approach ceases to be valid in general (somewhat reminiscent of fluctuations in the vicinity of a critical point invalidating mean-field theory in the case of phase transitions). Chapter 3 of this work is therefore devoted to a stochastic description of the nucleation process on top of an island that includes fluctuations, also in the presence of certain short and medium range interactions. In the process of second layer nucleation for a given island, the possible states of atomic configurations can be partitioned into equivalence classes belonging to similar configurations of atoms and a new master equation can be set up that describes transitions between such states (this is quite different from a coarse graining procedure over length scales). We derive the rates for such transitions, e.g. the attachment to subcritical clusters and loss of atoms from the island by surmounting the step edge barrier at the perimeter. With the greatly reduced number of possible states, the master equation can be solved numerically. The rates are also employed to derive scaling relations between the key parameters. This scaling theory provides insight into the sequence of events and which factors limit nucleation depending on parameters. The validity of the scaling theory and the more general rate equation theory are checked with KMC simulations.

Chapter 4 deals with the growth of clusters consisting of a binary alloy with a magnetic component as used for recording devices. This system is well studied experimentally and shows some interesting features which are not fully understood. For this system, the magnetic properties depend on the local arrangement of the magnetic species and are believed not to be important for the structure formation during the growth process. In the description of binary alloys, bond counting schemes with nearest neighbor interactions have been successfully used in many simulations. In studies of ordering in binary alloys, the kinetics are driven by vacancy diffusion, and three-dimensional models with fixed surfaces were studied[Sch98, FVCP97, KDM01]. Growing surfaces are also studied in continuum models (e.g. phase field models for crystal growth from a melt), as well as more microscopic models which usually make simplifying assumptions, e.g. the use of a solid on solid model (SOS) where the surface is described by a two dimensional height profile that precludes overhangs. SOS models are popular because implementation in a simulation is easy and analytical results for large scale features can be obtained for some cases. However, due to the asymmetry in lateral to vertical directions, facets on the sides of mounds or clusters are usually not equivalent to the corresponding surface of the equivalent crystallographic orientation (e.g. all $\{111\}$ facets, including the surface). To date, fully 3-dimensional growth is only rarely studied and then only for systems with one atomic species,

as e.g. in a simulation of sputtering experiments, where the deposition rate is much higher than in MBE, so that far fewer jumps of the particles need to be simulated[HGdlR98]. In order to study growth of binary alloys on weakly binding surfaces which facilitate cluster formation, a sound modeling of the facets is required. We therefore developed an efficient fully three dimensional KMC program where diffusion on self-organized facets is automatically equivalent for equivalent facet orientations and additional barriers emerge for moving between neighboring facets of arbitrary orientation. We simulate MBE growth with parameters chosen for the $CoPt_3$ system and make the connection between structural and magnetic properties based on properties of single bonds. We find that the dominant contribution to the magnetic anisotropy is a type of form anisotropy that arises from segregation of Pt to the surface combined with cluster shape. This anisotropy is different from the usual dipolar form anisotropy.

More generally, ordering and non-equilibrium effects are studied with classical Density Functional Theory (DFT) and its time-dependent variant (TDFT). They are powerful methods to derive phase diagrams, the kinetics of phase transformations and interfacial properties [L9̈4, Eva79, GPDM03] in condensed matter systems and were also formulated for lattice systems in order to match the discrete nature of structures encountered e.g. in the description of metallic alloys, adsorbate layers, and complex pattern formation on atomic scales[NDM93, RD96]. The starting point is the uniqueness theorem that states that for given interactions, the mean occupation numbers of all sites uniquely determine the site energies, so that thermodynamic potentials can be expressed as functionals of the occupation numbers. In the TDFT approach, deviations from equilibrium are represented by additional single particle site energies that are determined self-consistently. Since materials with constituents that have internal degrees of freedom are of great interest (e.g. magnetic atoms), we developed an extension of the DFT formalism for lattice gases to systems with internal degrees of freedom in sec. 5. In order to test approximations commonly used in DFT approaches, we investigate the statics and dynamics of occupation (density) profiles in the one-dimensional Potts model. In particular, by taking the exact functional for this model we can directly evaluate the quality of the local equilibrium approximation used in TDFT. Excellent agreement is found in comparison with KMC simulations. Finally, principal limitations of TDFT are demonstrated.

Part I

Epitaxial Growth

2 Basic quantities and concepts

2.1 Molecular Beam Epitaxy

Molecular Beam Epitaxy (MBE) is a well established technique for production of thin films and is especially important when a fine control over the growth process is desired. In this technique, adsorbate materials are heated in an evaporation chamber and the resulting beam is directed to the substrate. Ultrahigh vacuum with pressures $p < 10^{-10}$ mbar is needed to avoid contamination by residual vapor. With typical deposition rates below 1 monolayer per second, a precise control over the composition is possible. Applications include the fabrication of layered semiconductor heterostructures for electronic devices, and metallic multilayers of atomic thickness which show properties not found in the alloy of the constituents. Nanostructures can be produced by self-organized growth or using templates, e.g. colloidal or lithographic masks.

MBE growth usually proceeds far from equilibrium and the kinetics are governed by diffusion and aggregation processes. The most important parameters that can be controlled externally are the deposition flux and temperature. Determining the film morphology in this situation is a problem of stochastic dynamics. Review articles are available from an experimental viewpoint[Bru98] and theoretical viewpoint focusing on both kinetically and thermodynamically induced instabilities [PGM+00], as well as books, e.g.[MK04]

2.2 Atomistic processes in thin film growth

Before deposition in MBE experiments, substrate surfaces can be prepared by choice of the cutting or cleavage direction so that low index surfaces are obtained. Initial growth can then start on large terraces which are flat down to the atomic scale. Atoms are then deposited on the substrate with a rate F per unit area. At high substrate temperatures the adatoms reevaporate, but under ordinary conditions this reevaporation can be neglected or effectively taken into account by a reduced deposition rate. Under the usual conditions, far below the melting temperature, once an adatom is deposited, it equilibrates locally to a lattice position by the coupling between adatom vibration and excitations of the substrate. It will spend most of its time by vibrating about the lattice position

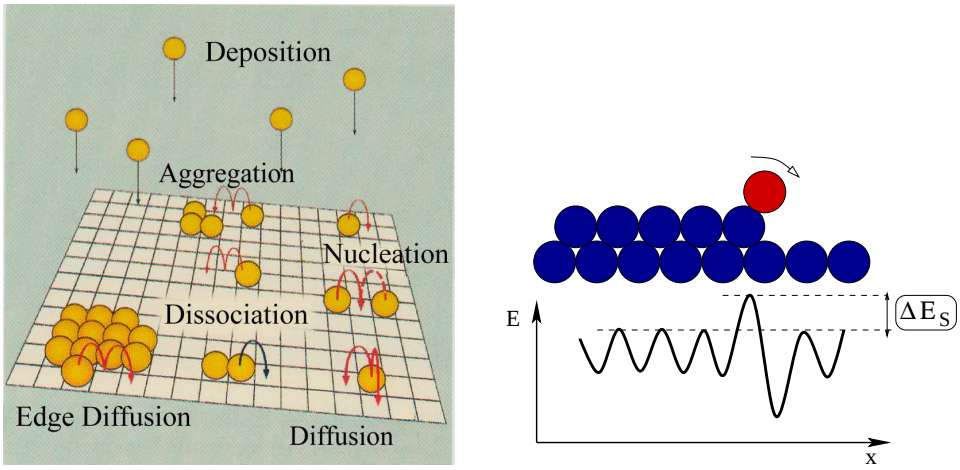

Figure 2.1: TODO: sollte noch durch eigenes Bild ersetzt werden a) Typical processes occurring in MBE: diffusion, aggregation, breakup of subcritical clusters and deposition events. b) Illustration of the potential for an atom moving over a step edge. ΔE_{S} is the barrier that has to be surmounted in addition to the diffusion barrier for crossing the edge.

and performs thermally activated jumps to neighboring free lattice sites over an energy barrier $\Delta E \gg k_{\mathrm{B}}T$ with a comparatively short time needed for the jump process. In this case transition state theory applies[HTB90]. It describes motion with a jump rate $W = \nu \exp(-E_{\mathrm{D}}/k_{\mathrm{B}}T)$ for attempt frequency ν and an energy barrier E_{D} at temperature T. Note that W is the total rate for jumps to *any* of the neighboring lattice sites.

Diffusion on an ideal surface can be regarded as a random walk on a two-dimensional lattice. The mean square displacement of the position $\mathbf{r}(t)$ grows linearly in time according to

$$\langle(\mathbf{r}(t) - \mathbf{r}(0))^2\rangle = Wa^2t = 2d\,\hat{D}\,t \tag{2.1}$$

where a is the distance covered by a single jump (usually the nearest neighbor distance) and d is the dimensionality of the motion. For unconstrained motion on a surface, $d = 2$ and $\hat{D} = \frac{1}{4}a^2W$ coincides with the surface diffusion coefficient D entering the diffusion equation $\partial n/\partial t = D\nabla^2 n$ for the density of adatoms. Since the exact prefactor is not important for most of the following arguments if used consistently, we will also use the symbol D for $4\hat{D}$ (so that $W = D/a^2$) unless the distinction is needed, as in A.2. The description of the migration process with the diffusion equation and the right boundary conditions will be very useful in the following.

The adatoms diffusing on the surface will come into contact as time progresses, and form islands that are held together by some bonding energy. While islands

of small size (number of atoms) $s \leq i$ are unstable and dissociate, islands with size $s > i$ are stable on the relevant time scales of the experiment. An island of size $s = i$ is called a critical nucleus. More precisely, the critical nucleus should be defined by referring to a particular atomic configuration. For simplicity we do not distinguish between the various possible configurations for a given island size. The concept of the critical nucleus is a dynamical one, and changes of i can indeed be observed, e.g. when the temperature is varied[Bru98].

In addition to the energies needed for breakup of subcritical clusters, other types of interactions can influence the growth, see sec. 3.6. An important factor controlling the film morphology is the additional step edge barrier $\Delta E_{\mathrm{S}} = E_{\mathrm{S}} - E_{\mathrm{D}}$ (Ehrlich-Schwoebel barrier[EH66, Sch69]) that has to be surmounted by an adatom in addition to the bare surface diffusion barrier E_{D}, when it crosses an island edge from the upper terrace.

2.3 Nucleation in the first layer

Most of the islands typically nucleate during the first stages of growth in the sub-monolayer regime, where only a small fraction of the surface is covered by adatoms. The most important quantities describing initial growth are the evolution of the island density $\rho_x(t)$ of stable islands on the substrate surface at time t and more generally the distribution $\Upsilon(s,t)$ of island sizes s (with s being the number of atoms forming the island). These quantities have been extensively studied in the past, both by experiment and theory. We will briefly summarize those results, which are relevant for the following analysis.

2.3.1 Island densities

The typical behavior of $\rho_x(t)$ is depicted in fig. 2.2. Also shown is the density of individual adatoms $\rho_1(t)$. As suggested by Amar and Family[AF96], one may distinguish between four different time regimes from small to large coverage $\theta \equiv Fa^2t$: The low-coverage regime L where $\rho_x(t)$ increases with t and $\rho_x(t) < \rho_1(t)$, the intermediate coverage regime I, where $\rho_x(t)$ increases with t and $\rho_x(t) > \rho_1(t)$, the saturation regime S (called aggregation regime A in [AF96]), where $\rho_x(t)$ stays approximately constant, and the coalescence regime C, where $\rho_x(t)$ strongly decreases due to coalescence of stable clusters. After the initial nucleation phase, the monomer density $\rho_1(t)$ decreases in regime I (see fig. 2.2), and the standard rate equations for sub-monolayer growth [VSH84] predict ρ_x to evolve as

$$\begin{aligned} \rho_x(t) \quad &\propto \quad \left(\frac{D}{Fa^4}\right)^{-\frac{i}{i+2}} (Fa^2t)^{\frac{1}{i+2}}\, e^{E_i/(i+2)k_{\mathrm{B}}T} \\ &= \Gamma^{-\frac{i}{i+2}}\, \theta^{\frac{1}{i+2}}\, e^{E_i/(i+2)k_{\mathrm{B}}T}\,, \end{aligned} \tag{2.2}$$

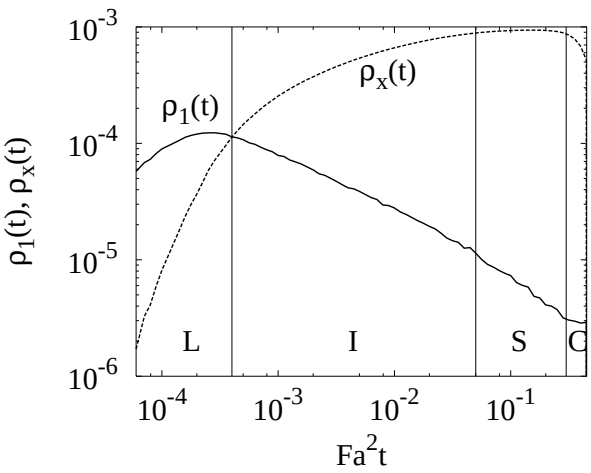

Figure 2.2: The densities $\rho_1(t)$ and $\rho_x(t)$ of adatoms and stable islands with increasing coverage $\theta \equiv Fa^2t$ as obtained from a kinetic Monte Carlo simulation of sub-monolayer growth. The different time regimes of low coverage L, intermediate coverage I, saturation S and coalescence C are indicated.

where E_i is the bonding energy of the critical nucleus in its preferred atomic configuration and

$$\Gamma = \frac{D}{Fa^4} \tag{2.3}$$

is a key parameter which represents the timescales for aggregation and deposition. It determines how many diffusion jumps an atom can perform on average until the next atom is deposited. With typical values for Γ ranging from 10^5 to 10^{10}, this implies about $10 - 10^6$ jumps for each free adatom between deposition events into an area of 100×100 deposition sites.

It should be noted that in regime S, the time dependence according to eq. (2.2) is not valid, because almost all adatoms being deposited attach to preexisting stable islands, so that $\rho_x(t)$ stays constant, $\rho_x(t) = \rho_x$. Within the standard rate equation approach, this effect may be accounted for by a proper dependence of the "capture areas" on the adatom density $\rho_1(t)$ (for a detailed discussion of this point in relation to experiments see [BBJ+99]). The scaling of ρ_x with Γ as given in (2.2), however, is still correct in regime S,

$$\rho_x \propto \Gamma^{-\frac{i}{i+2}} \,. \tag{2.4}$$

The capture area is given by the Voronoi cell associated with an island. In principle one should define the "dividing lines" in the Voronoi construction with respect to the island *boundaries*, which would lead to curved perimeters of capture areas. This definition amounts to capture areas which are very close to the results of an even more refined treatment based on the diffusion equation with absorbing boundary condition at the island perimeters[BSJ+99].

Since the time intervals between attachment events are usually much larger than the time required for a local rearrangement of atoms at the island boundary, the resulting shapes are usually compact. However, in cases where local relaxation of atoms due to fast edge diffusion is suppressed, one obtains dendritic or random fractal structures[BE94]. Dendritic growth (symmetrically branched, like snowflakes) is preferred at low T or high F, and a shape transition from dendritic to random fractal structures has been found e.g. for Ag/Pt(111) upon lowering the deposition flux[RBBK93, BRRK94]. At high temperatures, edge diffusion becomes relevant, and polygonal or "irregular" compact island morphologies develop (see e.g. [MHBC93]). In the case of reversible aggregation, theoretical scaling arguments supported by KMC simulations also predict a more complicated reentrant scenario where compact islands are only found for intermediate values of F[PF99]. In the case of dendritic growth, diffusion of adatoms on the islands becomes a rather complex phenomenon due to the confined motion along branches of various lengths[HA87]. We restrict our discussion to the case of compact islands here. Moreover, it should be noted that even for compact shapes, the island boundaries may have a fractal or, more precisely, self-affine [SB95] structure (this is the case e.g. for Eden clusters [PR84]).

2.3.2 Island size distribution

With $\rho_s(t)$ for the density of islands with size s and $\rho_{\text{tot}}(t)$ for the total island density including subcritical islands, the probability that an island has size s is $\Upsilon(s,t) = \rho_s(t)/\rho_{\text{tot}}(t)$. For this distribution the scaling ansatz

$$\Upsilon(s,t) = \frac{1}{\langle s(t)\rangle}\,\chi\Big(\frac{s}{\langle s(t)\rangle}\Big)\,. \tag{2.5}$$

could be matched successfully to simulations and experiments[BE92, BC94]. $\langle\ldots\rangle = \sum_{s=1}^{\infty}\ldots\Upsilon(s,t)$ denotes an average over s with respect to $\Upsilon(s,t)$. Treating the argument of the scaling function χ as a continuous variable, we find from (2.5) the relation $\langle s^m\rangle = \langle s\rangle^m \int_0^\infty dx\, x^m\chi(x)$ (as long as $\langle s^m\rangle < \infty$). Taking $m = 0, 1$ one obtains the normalization properties $\int dx\chi(x) = \int dx\, x\chi(x) = 1$. The mean island size $\langle s(t)\rangle$ is given by $\langle s(t)\rangle = \sum_{s=1}^{\infty} s\rho_s(t)/\rho_{\text{tot}}(t) = \theta/\rho_{\text{tot}}(t)a^2$. For the saturation regime S the density of islands with subcritical and critical size is small and thus $\rho_{\text{tot}} \simeq \rho_x$. Then eq. (2.4) implies

$$\langle s(t)\rangle \simeq \frac{\theta}{\rho_x a^2} \propto \theta\,\Gamma^{\frac{i}{i+2}}\,. \tag{2.6}$$

The relation $\langle s(t)\rangle \simeq \theta/\rho_x a^2 = Ft/\rho_x$ can also be understood more directly, since the increase of $\langle s(t)\rangle$ with t is given by the flux times the mean capture area ρ_x^{-1} of adatoms. For compact island growth, the island radius is $R(t) \sim \langle s(t)\rangle^{1/2}$ and thus from eq. (2.6)

$$\frac{R(t)}{a} = A(Fa^2t)^{1/2}\Gamma^{i/2(i+2)} \tag{2.7}$$

with A being some constant.

While mean-field theories for island nucleation in the first layer work remarkably well for predicting island densities, no analytical derivation of a closed form for the scaling function $\chi(x)$ is known that approximates experiments and simulations reasonably well. However, a good fit to results can be obtained with the empirical form

$$\chi(x) = C_i x^i \exp(-i a_i x^{1/a_i}) \tag{2.8}$$

which was proposed[AF95] for regime S. The function has a maximum at $x = 1$ and the two conditions $\int dx \chi(x) = \int dx\, x\chi(x) = 1$ determine the parameters C_i and a_i.

More refined ways of analysis[PAF01, EB01] that take into account correlations between the island size and its capture area by coupling sets of evolution equations for both quantities, succeed in reproducing simulated size distributions without supposing an explicit form for the scaling function. In theory, dimer mobility should affect the scaling properties of the island density and the size distribution [BGK+96], but the effects are difficult to find experimentally.

3 Second layer nucleation

3.1 Introduction

During the MBE process, two-dimensional islands composed of adsorbate atoms form on the substrate. If these islands coalesce before stable clusters nucleate on top of the islands in the second layer, a flat two-dimensional film results. By contrast, if the onset of second layer nucleation precedes island coalescence, three-dimensional cluster formation is obtained. The term "second layer nucleation" should not be taken literally here but rather should apply to the formation of stable nuclei on top of islands in general. Nuclei are considered to be stable once their size exceeds a critical number of i atoms, as defined in sec. 2.2. As in the case of nucleation in the first layer, the incoming atom flux F and the jump rate D/a^2 of adatoms enter with the ratio $\Gamma \equiv \frac{D}{Fa^4}$. In addition, the step edge barrier ΔE_{S}, and various dissociation rates of unstable clusters of size $s \leq i$ are important parameters. If the bond energies of the unstable clusters (i.e. of clusters of size $s \leq i$) are negligibly small, then the nucleation rate Ω depends only on two dimensionless parameters, which are the edge crossing probability

$$\alpha \equiv \exp\left(-\frac{\Delta E_{\mathrm{S}}}{k_{\mathrm{B}}T}\right) \tag{3.1}$$

and $\Gamma = D/Fa^4$ which was already discussed in the context of nucleation in the first layer in sec. 2.3. For larger step edge barriers ΔE_{S} one expects adatoms to remain longer on islands and therefore to accumulate more easily, which would lead to an increased second layer nucleation rate $\Omega(R)$ and smaller typical island sizes R_c (defined more precisely below) at the nucleation event. In fact, the theory predicts that only for sufficiently large ΔE_{S} three-dimensional clusters can occur on the substrate (for an alternative possibility see however [SPT]). In the case of strongly ramified or fractal island boundaries, the microscopic step edge barrier can vary strongly along the island boundary[Fei98]. In any case we will always understand ΔE_{S} as an effective barrier (see below and the footnote on page 17). For the study of second layer nucleation we will focus on compact island shapes. Moreover, second layer nucleation in the intermediate regime I of first layer nucleation (see fig. 2.2) is unlikely to occur, since the island radii in this regime are typically smaller than the critical radius R_c. We therefore consider the second layer nucleation in the saturation regime S, where eqs. (2.4)-(2.8) apply.

For the equilibrium case, the question whether three dimensional or layer-by layer growth can be expected was answered long ago: If the interfacial tension between the substrate and adsorbate is larger than the difference of the respective surface free energies, then cluster formation is preferred ("Volmer-Weber growth" [VW26]), while a smaller (or equal) interfacial tension leads to the formation of flat films ("Van-der Merwe growth"). An intermediate case is the "Stranski-Krastanov growth" mode[SK38], where cluster formation sets in after the thickness of an initially smooth film exceeds a critical height. This case may be understood from an interfacial tension that varies with the film thickness. More recently, the influence of strain effects on equilibrium film morphologies has been investigated by various authors[BvdM86]. As for the equilibrium structures, it might be possible that also in the non-equilibrium situation cluster formation sets in above a certain film thickness, when the relevant parameters governing the nucleation of stable clusters on top of islands (see below) depend sensitively on the film thickness. However, despite this similarity of the possible growth processes with the equilibrium growth modes, it should be noted that the dynamic problem is very different. In MBE, flat films can be produced even if the adsorbate does not wet the substrate[Bru98].

The first theory for second layer nucleation in MBE was set up by J. Tersoff, A. W. Denier van der Gon, and R. M. Tromp[TvdGT94], which will be referred to as "TDT approach" in the following. Solving the stationary diffusion equation in the presence of an incoming flux and employing classical nucleation theory[VSH84], these authors succeeded in deriving an explicit expression for the rate of nucleation $\Omega(R)$ on top of circular shaped islands of radius R. They assumed that all island radii evolve approximately as the mean island radius $R(t)$ at time t. This situation will be referred to as the "single-island model" in the following and will be checked by simulation. In the single-island model, they calculated from $\Omega(R)$ the fraction $f(t)$ of islands on top of which a stable cluster has nucleated ("covered islands"). It turned out that $f(t)$ rises from zero to one in the vicinity of a "critical time" t_c, which allows one to define a critical island radius $R_c \equiv R(t_c)$ for second layer nucleation. A simple criterion for the occurrence of "rough multilayer" as opposed to smooth "layer-by-layer growth" is that R_c is smaller than the mean distance l between islands in the first layer. Using the TDT approach and experimental results for $f(t)$, ΔE_{s} was estimated for a variety of different systems [BBRK95, MVvdV$^+$95, SH95, Mar96, RT98].

An alternative approach for treating the problem of second layer nucleation within a stochastic description based on scaling arguments was developed recently [RM99]. It was shown that for $i=1$ the TDT approach is not applicable, but the detailed treatment of fluctuations with only two atoms on top of the island yields a correct description of the process (see also [KPM00]; for an earlier approach focusing on one dimension see [EV94]). In this work we will extend the former study of second layer nucleation and show under what circumstances the TDT approach becomes valid again. In particular, we will show that the mean-field

assumptions underlying the TDT approach are valid for larger critical nuclei $i \geq 3$, while for small critical nuclei $i = 1, 2$ second layer nucleation is dominated by fluctuations[HRM00].

Moreover, we will discuss in sec. 3.2.3 how to derive the fraction $f_{\mathrm{m}}(t)$ of covered islands, when one relaxes the assumption that all island radii evolve as the mean radius $R(t)$. In the time regime of almost constant island density ("saturation regime" preceeding island coalescence[AF96]) we can define an effective "capture area" for adatoms (see sec. 2.3.2). In order to calculate $f_{\mathrm{m}}(t)$ for the "multi-island model" from $f(t)$, one needs to know the probability distribution of islands with a certain size and capture area, when the saturation regime is reached.

This chapter is organized as follows: In the next section we use Kinetic Monte Carlo (KMC) simulations to test the equivalence of the multi-island and single-island models. This provides a base for testing theories, beginning with the TDT approach in sec. 3.3 which turns out to be in contradiction to the simulation results in important cases. Then a simplified stochastic description of second layer nucleation is first presented in its general methodology and subsequently applied to small and large critical nuclei in sec. 3.4. It is instructive to observe the different physical conditions that lead to the nucleation event in the two cases. We develop in sec. 3.5 a general theory for second layer nucleation on the basis of novel rate equations, which allows one to calculate the time-development of cluster configurations on compact two-dimensional islands, and apply it to the cases discussed in the previous sections. Additional rates for two important types of interactions are derived and incorporated into the theory in sec. 3.6. Experimentally, second layer nucleation is also employed to measure step edge barriers in cases where other methods (e.g. field ion microscopy) cannot be applied. The significance of interaction effects for experiments measuring the step edge barrier is demonstrated and further applications are discussed. Sec. 3.8 concludes the chapter with a summary and discussion of the most important results as well as an outlook to further research.

3.2 Kinetic Monte Carlo Simulations

Kinetic Monte Carlo simulations are a well-established technique for modeling MBE experiments [BE99, BHM$^+$96, AF95, CSL$^+$01]. In our investigation of second layer nucleation, we adopt a simulation scheme similar to previous, successful models of surface growth kinetics[AF95, BC94]. We choose a substrate with fcc(111) symmetry, since surfaces of that kind are often studied in metal epitaxy, and commonly exhibit high ΔE_{S}. The multi-island model simulates the growth kinetics for a part of the surface large enough to allow for self-organized island formation. It includes all processes of diffusion and aggregation occurring in the MBE experiment. By analyzing the set of islands of various sizes on the substrate, we determine the fraction $f_{\mathrm{m}}(t)$ of islands covered with a stable nucleus

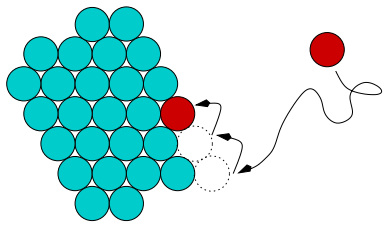

Figure 3.1: Illustration of the local relaxation process when an adatom arrives at an island edge.

at time t. On the other hand, we consider, as in the TDT approach, only one island with the mean radius $R(t)$ evolving deterministically in time. The fraction $f(t)$ of covered islands in this single-island model is then determined by calculating the probability for second layer nucleation up to time t from a large set of independent simulations. By examining both models we are able to quantify the influence of the cluster size distribution under generic growth conditions. The data for the multi-island simulations presented here were kindly provided by Jörg Rottler[Rot99].

3.2.1 Multi-island model

Atoms are randomly deposited with a rate Fa^2 per unit cell onto a triangular lattice. Only one atom is allowed to occupy a given lattice site. After instantaneously relaxing to a position, where they are supported by three nearest neighbors in the layer below ("downward funneling"), the atoms can change their position by performing thermally activated jumps to a vacant nearest neighbor site in the same layer. The rate for such an event is $\nu e^{-(E_\mathrm{D}+nE_\mathrm{b})/k_\mathrm{B}T}$ for a process that requires breaking n bonds of energy E_b to neighboring atoms in the same layer. E_D is the energy of the transition state and the resulting rate for diffusion is $D/a^2 = \nu e^{E_\mathrm{D}/k_\mathrm{B}T}$. This jump rate only depends on the initial configuration of the atom, in contrast to the rates used in chapter 4, where they depend on both initial and final neighborhoods. This choice implies that diffusion along an edge requires the same total activation energy as dissociation from the edge. Compact island morphologies are known to emerge if a fast diffusion process is present along island edges. Here we include the initial stages of this process similar as in earlier approaches (see e.g. refs. [AF96, BE95]) by including a local relaxation mechanism. In this method an atom being in contact with at least one nearest neighbor after a jump, is immediately transferred to a nearest neighbor site, if it can increase its coordination number. This procedure is repeated until the atom can no longer increase its local coordination (see fig. 3.1). This algorithm

is sufficient to preclude the occurrence of fractal structures[Rot99].

A situation with $i = 1$ can be realized when $E_b/k_BT \gg 1$. For $10^5 \leq \Gamma \leq 10^9$, a value $E_b/k_BT > 10$ is sufficient. In the following, we study this case with an effective $i = 1$ for the multi-island model. Once a stable cluster of size $s > i$ has formed, adatoms can attach to it.

Interlayer diffusion of atoms deposited onto islands is hindered by the Ehrlich-Schwoebel barrier ΔE_S, which reduces the jump rate $D/6a^2$ by the edge crossing probability $\alpha = \exp(-\Delta E_S/k_BT)$.[1] For computational convenience, we model the crossing by a two-step process in the simulation: First, when an atom passes the boundary by a simple diffusion move, it remains in the same layer but moves to a place, where it is supported by only two atoms underneath. Then, an additional move becomes possible where the atom changes the layer with a rate $\nu e^{E_D+\Delta E_S/k_BT}$ (for similar simulations including ΔE_S, see, e.g. [SH95, RZSV94]). We do not distinguish between crossing of A and B steps or facilitation of processes at kinks and have not attempted to model any more realistic scenarios, as e.g. collective rearrangements of atoms including exchange processes[WE91, SS94, JJSN95]. This is well justified as long as one is interested in the influence of an effective Schwoebel barrier. [2] The implementation also does not account correctly for diffusion on side facets of 3-dimensional clusters, where the layer may change in a diffusion jump without involving a step edge barrier (see also chapter 4). Such a fully 3-dimensional simulation is not needed in this case, because the substrate is modeled with a sufficiently high binding energy so that islands remain flat.

The fraction $f_m(t)$ of covered islands as a function of the total coverage Fa^2t is shown in fig. 3.2 for some representative parameters (full symbols). As expected, $f_m(t)$ first is close to zero, then increases strongly in some time interval around a "critical time" t_c, and finally saturates at one. In the inset of fig. 3.2 we show the dependence of the mean island radius $R(t) \equiv (\langle s(t)\rangle/\pi)^{1/2}a$ on Fa^2t during the growth process. In agreement with (2.7), we find $R(t) = A(Fa^2t)^{1/2}\Gamma^{1/6}$ with $A \cong 0.78$.

To be specific, let us define the critical time t_c via the condition $f_m(t_c) = 1/2$,

[1] Writing $D/6a^2 = \nu \exp(-E_0/k_BT)$ for the in-layer hopping rate and $\alpha D/6a^2 = \nu' \exp(-E_S/k_BT) = [(\nu'/\nu)\exp(-\Delta E_S/k_BT)](D/6a^2)$ for the hopping rate over the step edge, one should more generally take $\alpha = (\nu'/\nu)\exp(-\Delta E_S/k_BT)$, if the attempt frequencies ν and ν' are different. For a general discussion on analyzing experimental data for attempt frequencies, see [OBWL01].

[2] For the calculation of the effective step edge barrier ΔE_S that determines the total escape rate from an island, one should average over the local escape rates $\Gamma_\mu \propto \exp[-\Delta E_\mu/k_BT]$ associated with the set of microscopic barriers $\{\Delta E_\mu\}$ along the island edge. Accordingly, $\Delta E_S = -k_BT \ln\langle\exp[-\Delta E_\mu/k_BT]\rangle$, where $\langle\ldots\rangle$ denotes an average over the ΔE_μ (with an appropriate weighting by the probabilities of an adatom to be at the corresponding boundary sites). Note that for fractal island boundaries this averaging may result in an effective ΔE_S that depends on R.

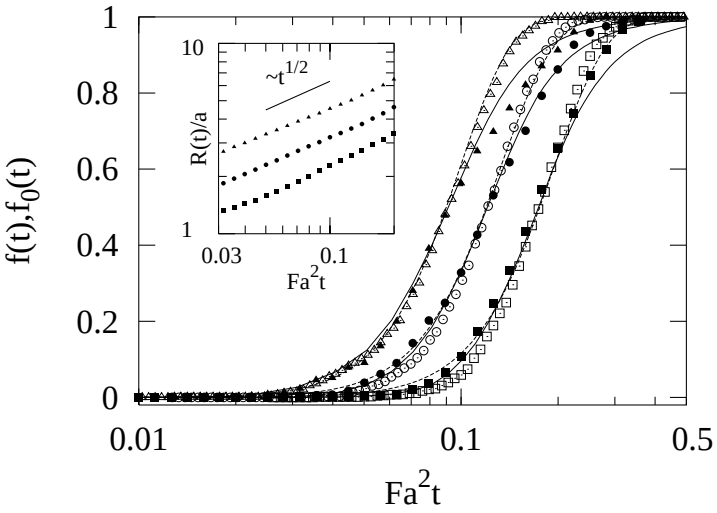

Figure 3.2: The fractions $f_{\mathrm{m}}(t)$ for the multi-island model (full symbols) and $f(t/1.21)$ for the single-island model (open symbols) of covered island as a function of the total coverage Fa^2t for $i=1$, $\alpha=10^{-5}$, and three different $\Gamma=10^5$ (■, □), 10^6 (●, ○), and 10^7 (▲, △). The dashed lines fitting $f(t/1.21)$ were calculated from the theoretical predictions for the second layer nucleation rate $\Omega(R(t))$ (eq. (3.25)). The solid lines fitting $f_{\mathrm{m}}(t/1.21)$ were calculated according to eq. (3.5) with $\Upsilon_\sigma(\sigma)\sim\sigma^2$ (see text). The inset displays the time-dependence of the mean island radius $R(t)\equiv(\langle s(t)\rangle/\pi)^{1/2}a$ (see eqs. (2.6,2.7)).

and the corresponding critical island radius R_c by $R_c=R(t_c)$,

$$f_{\mathrm{m}}(t_c)=1/2\,,\;\; R_c\equiv R(t_c)=A(Fa^2t_c)^{1/2}\Gamma^{i/2(i+2)}a\,. \tag{3.2}$$

Plots of R_c as a function of α for various fixed Γ are shown in fig. 3.3 (full symbols). With increasing step edge barrier, i.e. decreasing α, adatoms on average remain longer on an island and nucleation of stable dimers occurs at smaller island radii. Accordingly, R_c decreases with decreasing α (see "regime II" in the figure). For very small α, however, the step edge barrier is practically never surmounted and thus is in effect infinitely high. Therefore, R_c becomes independent of α ("regime I" in fig. 3.3). The crossover between the two regimes is marked by the thick solid line. The full symbols in fig. 3.3 terminate at the dashed line $\alpha_\star(\Gamma)$, which marks the onset of island coalescence. For $\alpha>\alpha_\star(\Gamma)$, islands in the first layer merge before second layer nucleation takes place and R_c can no longer be determined from the multi-island model. A good fit to the data in regime II can be obtained with slope 1/7 in the double logarithmic plot, corresponding to a power law $R_c\sim\alpha^{1/7}$. This will be found to be significantly different from $R_c\sim\alpha^{1/3}$ as predicted by the TDT approach summarized in sec. 3.3.

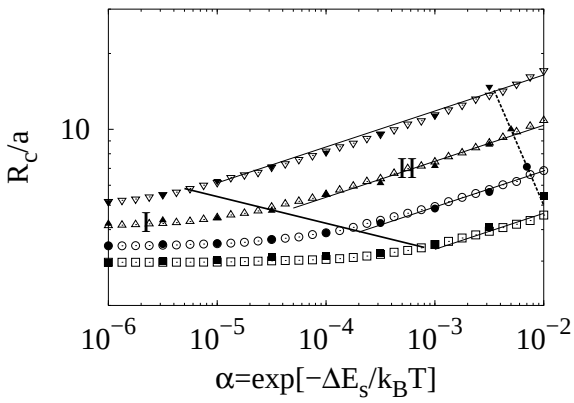

Figure 3.3: Dependence of the critical island radius R_c on α for $i = 1$ and various $\Gamma = 10^5$ (■, □), 10^6 (●, ○), 10^7 (▲, △), and 10^8 (▼, ▽). Full symbols refer to the results from the multi-island model, while open symbols refer to the results obtained from the single-island model ($R_c = 1.1R_c'$). The dashed line marks the onset of layer-by-layer growth, and the solid line with negative slope marks the crossover between regimes I and II; the solid lines fitting the data in regime II have slope 1/7.

3.2.2 Single-island model

Second layer nucleation can also be addressed in a simpler model, which does not attempt to describe the entire growth dynamics, but focuses on the decisive factors that determine nucleation in the presence of the step-edge barrier. In this model, the complicated nucleation and diffusion-mediated growth of the two-dimensional islands, on which the second layer nucleation takes place, is replaced by letting the radius of *one* circular island expand deterministically in time as $R(t)/a = A(Fa^2t)^{1/2}\Gamma^{i/2(i+2)}$, where A is taken from the full simulation of the multi-island model.

The island is embedded in a substrate area large enough to accommodate the island at all relevant times. Deposition and diffusion of adatoms take place in the same manner as in the multi-island model. Atoms inside the island boundary can escape by overcoming the step edge barrier. Those atoms that have surmounted the barrier or that have been deposited outside the island boundary are removed from the lattice. Thus the single-island model considers the deposition of random walkers within a time-dependent, circular boundary that is partially reflecting. Due to its greater simplicity, it allows for more specific analysis with a larger parameter space (there is no restriction due to coalescence of distinct islands).

In the non-interacting particle model, the "critical event" is to find (i+1) atoms on neighboring lattice sites. Analogous to the multi-island model we can define the fraction $f(t)$ of covered islands up to time t. The fraction now refers to an ensemble of islands obtained in independent simulation runs. All islands in

these runs grow with the same deterministic growth law. Results for $f(t)$ are shown in fig. 3.2 for the same parameters as in the multi-island model. Good agreement with $f_{\mathrm{m}}(t)$ is achieved for small times (corresponding to $f_{\mathrm{m}}(t) \lesssim 1/2$), when the time in the single-island model is rescaled by a constant factor, i.e. $f_{\mathrm{m}}(t) \simeq f(t')$ with $t' = t/1.21$. The factor is a consequence of the idealized circular island perimeter in the single-island model. In the multi-island model by contrast, the islands are far from being perfectly circular. They have rougher edges with more boundary sites, which causes adatoms to escape the islands more easily and second layer nucleation to occur at later times $t \cong 1.21t'$.

At larger times (corresponding to $f_{\mathrm{m}}(t) \gtrsim 1/2$), however, $f_{\mathrm{m}}(t)$ deviates from $f(t')$ and these deviations become more pronounced for larger Γ. The reason for this discrepancy is the presence of islands with size much smaller than $\langle s(t) \rangle$ in the multi-island model. Nucleation of stable clusters on top of these islands occurs at a later time, which causes $f_{\mathrm{m}}(t)$ to be smaller than $f(t') = f(t/1.21)$ at large t. In fact, we will show in sec. 3.2.3 that this effect can be accounted for by considering the probability distribution of islands with a certain size and capture area. When R_c approaches the mean distance l, coalescences of larger islands also lead to modifications of $f_{\mathrm{m}}(t)$ for $t \gtrsim t_c$.

The critical radius R'_c in the single-island model can be defined as in the many island model by $R'_c = R(t'_c)$, where $f(t'_c) = 1/2$. Due to the fact that $t_c = 1.21t'_c$ we expect $R_c = 1.21^{1/2} R'_c = 1.1R'_c$. Results for $1.1R'_c$ as a function of α are shown in fig. 3.3 (open symbols) for the same parameters as in the multi-island model (full symbols). As can be seen from the figure, there is almost perfect agreement between both data sets. Moreover, the data for R'_c can be obtained also beyond the dashed line marking the onset of layer-by-layer growth. Let us also note that, as long as one is interested only in R'_c (or $R_c = 1.1R'_c$), one may obtain it even more simply in the single-island model (without calculating $f(t)$) by determining the average radius of the island at the time of the nucleation event,

$$R'_c = R(t'_c) \simeq \int_0^\infty dt \, \frac{df(t)}{dt} \, R(t) \, . \tag{3.3}$$

Note that $df(t)/dt$ is the probability density of the second layer nucleation times and that the average of $R(t)$ with respect to $df(t)/dt$ is approximately equal to $R(t'_c)$, since $df(t)/dt$ is sharply peaked around t'_c.

3.2.3 Equivalence of single-island and multi-island models

In order to determine $f_{\mathrm{m}}(t)$ from $f(t)$ we define by $\psi(s, \sigma, t) \, ds \, d\sigma$ the probability for an island to have a size in the interval $[s, s + ds]$ and a capture area (see sec. 2.3.2) in the interval $[\sigma, \sigma + d\sigma]$ at time t.

Let us consider $f(t)$ to be a functional of the growth law $R(t)$ only, as it is the case, for example, when one approximates the second layer nucleation by a

Poisson process with a time dependent nucleation rate $\Omega(R(t))$. Then $f(t) = G_0[R(t)] = 1 - \exp[-\int_0^t dt'\,\Omega(R(t'))]$ (see eq. 3.10). In the saturation regime the growth law for an island can be written as $\pi R^2(t) = s_\times + F\sigma(t - t_\times)$, where $t_\times$ is the time when the saturation is reached (see fig. 2.2) and $s_\times$ is the island size at that time. (We restrict ourselves to film-morphologies far from coalescence here, so that σ can be regarded as time-independent.) With the specified growth law, the functional $G_0[R(t)]$ can be expressed by a function $g_0 = g_0(t; s_\times, \sigma, t_\times)$, and $f_\mathrm{m}(t)$ is calculated via

$$f_\mathrm{m}(t) = \int_0^\infty ds_\times \int_0^\infty d\sigma\, \psi(s_\times, \sigma, t_\times)\; g_0(t; s_\times, \sigma, t_\times)\,. \tag{3.4}$$

A detailed investigation of the probability distribution $\psi(s, \sigma, t)$ is certainly of interest but beyond the scope of the present work. A simple idea would be to neglect correlations between the stochastic variables s and σ, $\psi(s, \sigma, t) \simeq \Upsilon(s, t)\,\Upsilon_\sigma(\sigma, t)$, and to use previously derived scaling forms for the island size distribution $\Upsilon(s, t)$ (see e.g. refs. [BE99, AF96]) and the capture area distribution $\Upsilon_\sigma(\sigma, t)$ (see e.g. refs. [BE92, SP94]).

Here we will follow a simpler approach. Since for typical situations we find both $s_\times$ and $t_\times$ to be significantly smaller than $s_c = \pi R_c^2$ and t_c, respectively, we use the growth law $s(t) = F\sigma t$ for an island with capture area σ in the full simulation. The on-top nucleation probabilities $\tilde{g}_0(t; \sigma)$ for islands exhibiting different capture areas can then be related by a rescaling of time, i.e. $\tilde{g}_0(t; \sigma_1) = \tilde{g}_0(\sigma_1 t/\sigma_2; \sigma_2)$. Moreover, since for film morphologies far from coalescence ($\alpha \ll \alpha_\star(\Gamma)$), $\Upsilon(\sigma, t)$ is approximately independent of time, we have $f(t) = \tilde{g}_0(t; \bar{\sigma})$, where $\bar{\sigma} = \int d\sigma\, \Upsilon_\sigma(\sigma, t)\sigma \simeq \rho_x^{-1}$. Hence,

$$f_\mathrm{m}(t) = \int_0^\infty d\sigma\; \Upsilon_\sigma(\sigma)\, \tilde{g}_0(t; \sigma) = \int_0^\infty d\sigma\; \Upsilon_\sigma(\sigma)\, f_0\Big(\frac{\bar{\sigma}}{\sigma} t\Big)\,. \tag{3.5}$$

In this simplified eq. (3.5) knowledge of the nucleation rate $\Omega(R)$ is not necessary and $f_\mathrm{m}(t)$ can be directly obtained from $f(t)$ when $\Upsilon_\sigma(\sigma)$ is known.

Writing $\Upsilon_\sigma(\sigma) = \bar{\sigma}^{-1} h(\sigma/\bar{\sigma})$, where $\int dx\, h(x) = \int dx h(x) x = 1$, the transformation (3.5) becomes $f_\mathrm{m}(t) = \int_0^\infty dx h(x) f(xt)$. For a random distribution of point islands, we would have $h(x) = \exp(-x)$. However, since there is a depletion zone of adatoms near an island, the probability for other islands to nucleate in an area close to an existing one is reduced and not exponential. For an isolated island, dimensional analysis predicts the extension ξ of the depletion zone to be of order $(D/F)^{1/4}$ (alternatively it was suggested [MKWL92] that the linear size of the depletion zone should scale as the mean island distance l, i.e. $\xi \sim l$). By comparing ξ with $l \sim \rho_x^{-1/2} \sim \Gamma^{i/2(i+2)}$ between islands, we expect that $h(x)$ does not exhibit a large x regime with $h(x) \sim \exp(-x)$ for $i = 1$. We thus are satisfied with a simple power law ansatz $h(x) = Cx^\phi$ for $x \leq x_\star$, where C and $x_\star$ follow from the two conditions imposed on $h(x)$, and ϕ is a fitting parameter.

To test this ansatz we take $f(t)$ for $\Gamma = 10^7$ from fig. 3.2 (open symbols or dotted lines) and compare $f_{\mathrm{m}}(t)$ as calculated from eq. (3.5) (solid lines in fig. 3.2) with the corresponding $f_{\mathrm{m}}(t)$ as obtained in the simulation (full symbols in fig. 3.2). As can be seen from fig. 3.2, for $\Gamma = 10^6$ and $\Gamma = 10^7$ a fairly good account of the differences between $f(t)$ and $f_{\mathrm{m}}(t)$ can be obtained by choosing $\phi = 2$. However, for $\Gamma = 10^5$ the theoretical curve underestimates the fraction of covered islands at large times (where $f_{\mathrm{m}}(t) \gtrsim 1/2$). Better agreement between theory and simulation can only be obtained if one would allow ϕ to depend on Γ. Alternatively, we have tried an ansatz for $h(x)$ similar to that used by Amar and Family [AF95] for the scaling function characterizing the island size distribution (see eq. (2.8)). This ansatz yields comparable results, but is also not successful in accounting for the changes with Γ. It should therefore be interesting to use more detailed theoretical accounts for $\psi(s, \sigma, t)$[MR00, PAF01].

Having shown that the single-island and multi-island models are essentially equivalent, except for differences between $f_{\mathrm{m}}(t)$ from $f(t)$ for large times that can be attributed to the island size distribution, we will focus on the single-island model in the remaining part of the chapter.

3.3 TDT Approach

In the TDT approach, [TvdGT94] one starts by calculating the adatom density ρ_1^{st} on a circular island with radius R in the stationary state. The stationary diffusion equation with the incoming atom flux acting as a source term reads

$$D\left[\frac{\partial^2}{\partial r^2} + \frac{1}{r}\frac{\partial}{\partial r}\right]\rho_1^{\mathrm{st}} + F = 0\,, \tag{3.6}$$

and it is supplemented by the boundary conditions ($\alpha = \exp(-\Delta E_{\mathrm{S}}/k_{\mathrm{B}}T)$)

$$\left.\frac{\partial \rho_1^{\mathrm{st}}}{\partial r}\right|_{r=0} = 0\,, \quad -\left.\frac{\partial \rho_1^{\mathrm{st}}}{\partial r}\right|_{r=R} = \frac{\alpha}{a}\,\rho_1^{\mathrm{st}}\Big|_{r=R}\,, \tag{3.7}$$

where a/α is commonly referred to as the "Schwoebel length" (see also the footnote on page 111). The boundary conditions express the fact that the current density $-D\partial\rho_1^{\mathrm{st}}/\partial r$ must vanish at the origin and that at the edge it is given by the density ρ_1 times the "velocity" (rate times lattice spacing) $(D\alpha/a^2)a$ to cross the step edge barrier. The solution of eqs. (3.6,3.7) is

$$\rho_1^{\mathrm{st}}(r) = \rho_1^{\mathrm{st}}(0) - \frac{Fr^2}{4D}\,, \quad \rho_1^{\mathrm{st}}(0) = \frac{FR^2}{4D}\left(1 + \frac{2a}{\alpha R}\right)\,. \tag{3.8}$$

According to standard rate equation theory [VSH84] the local nucleation rate is proportional to $D\rho_1^{i+1}$. Hence we obtain from eq. (3.8) for the total nucleation

rate $\Omega(R)$ on top of the island

$$\begin{aligned}\Omega(R) &= \kappa\frac{D}{a^2}\int_0^R \frac{2\pi r dr}{a^2}[\rho_1^{\rm st}(r)a^2]^{i+1} \\ &= \frac{4\pi\kappa\Gamma^{-(i+1)}}{(i+2)\alpha^{2(i+2)}}\frac{D}{a^2}\left(\frac{\alpha R}{2a}\right)^{i+2}\left[\left(1+\frac{\alpha R}{2a}\right)^{i+2}-1\right] \\ &\simeq \begin{cases} 4\pi\kappa\Gamma^{-(i+1)}\alpha^{-(i+1)}\dfrac{D}{a^2}\left(\dfrac{R}{2a}\right)^{i+3}, & \alpha \ll \dfrac{2a}{R} \\ \dfrac{4\pi\kappa\Gamma^{-(i+1)}}{i+2}\dfrac{D}{a^2}\left(\dfrac{R}{2a}\right)^{2(i+2)}, & \alpha \gg \dfrac{2a}{R}\end{cases}\end{aligned} \tag{3.9}$$

where κ is a constant.

For a given time evolution of the island radius $R=R(t)$, one can calculate the probability $f(t)$ for a stable nucleus to have formed on top of the island up to time t as follows: The increase $f(t+\Delta t)-f(t)$ in a small time interval Δt is equal to the probability $[1-f(t)]$ that up to time t no stable nucleus has formed times the probability $\Omega(R(t))\Delta t$ that the nucleation takes place in the time interval $[t, t+\Delta t]$. Taking the limit $\Delta t \to 0$ and solving the corresponding differential equation with the initial condition $f(0)=0$ yields

$$f(t) = 1 - \exp\left[-\int_0^t dt'\,\Omega(R(t'))\right]. \tag{3.10}$$

Inserting the growth law for $R(t)$ given by (2.7) into (3.9,3.10) yields

$$\begin{aligned} f(t) &= 1-\exp\left[-\frac{2\Gamma^{-\frac{i}{i+2}}}{A^2Fa^4}\int_0^{R(t)} dr\, r\Omega(r)\right] \\ &\simeq \begin{cases} 1-\exp\left[-C_<\Gamma^{-\frac{i(i+3)}{i+2}}\alpha^{-(i+1)}\left(\dfrac{R}{a}\right)^{i+5}\right], & \alpha \ll \dfrac{2a}{R(t)} \\ 1-\exp\left[-C_>\Gamma^{-\frac{i(i+3)}{i+2}}\left(\dfrac{R}{a}\right)^{2(i+3)}\right], & \alpha \gg \dfrac{2a}{R(t)}\end{cases}\end{aligned} \tag{3.11}$$

where $C_> \equiv (2^{-2(i+1)}\pi\kappa A^{-2})/[(i+2)(i+3)]$ and $C_< \equiv 2^{-i}\pi\kappa A^{-2}$. In going from the first to the second line in (3.11) we have used that the integral over r is dominated by the upper integration bound $R(t)$ (for $R(t)/a \gg 1$). It follows that the critical radius scales as

$$R_c \sim \Gamma^\gamma \alpha^\mu, \tag{3.12}$$

where

$$\gamma = \begin{cases} \dfrac{i(i+3)}{(i+2)(i+5)}, & \alpha \ll \Gamma^{i/[2(i+2)]} \\ \dfrac{i}{2(i+2)}, & \alpha \gg \Gamma^{i/[2(i+2)]}\end{cases} \tag{3.13}$$

and

$$\mu = \begin{cases} \dfrac{(i+1)}{(i+5)}\,, & \alpha \ll \Gamma^{i/[2(i+2)]} \\ 0\,, & \alpha \gg \Gamma^{i/[2(i+2)]} \end{cases} \tag{3.14}$$

Equations (3.12-3.14) predict that for large step edge barriers, R_c depends strongly on ΔE_{S}, $R_c \sim \exp[-(i+1)\Delta E_{\mathrm{S}}/(i+5)k_{\mathrm{B}}T]$, while for small barriers, R_c becomes independent of ΔE_{S}. For $i = 1$ in particular, one finds $R_c \sim \Gamma^{2/9}\alpha^{1/3}$ for $\alpha \ll \Gamma^{1/6}$ and $R_c \sim \Gamma^{1/6}$ for $\alpha \gg \Gamma^{1/6}$. The exponent $\mu = 1/3$ for α is in contradiction to the simulation result where $R_c \sim \alpha^{1/7}$ was obtained (see also fig. 3.3). In the next chapter a stochastic description is developed that does not assume the local nucleation rate to be simply proportional to $D\rho_1^{i+1}$.

3.4 Stochastic description

In this section we develop a stochastic description of the nucleation process based on the scaling approach for second layer nucleation presented in [RM99] (see also Krug *et al.* [KPM00]). The procedure focuses on the non-interacting particle model, although formally it is possible to extend scaling concepts to situations, where the lifetimes of unstable clusters become important. This is discussed in a more general context in sec. 3.6.1. The treatment of the non-interacting particle model outlined in this section already captures the salient features of the problem in terms of lifetimes, occupation probabilities and encounter rates. We will show that there exist two possible mechanisms for the formation of a stable cluster: In the first case, there is typically no atom on top of the island and a stable cluster is formed due to fluctuations, in which by chance $i+1$ atoms are present on the island. In the second case by contrast, there are on average more than $i+1$ atoms on top of the island during the formation of a stable cluster so that the nucleation process can be described in a mean-field type manner.

It turns out that the fluctuation-dominated case takes place for $i \leq 2$, while the mean-field situation occurs for $i \geq 3$. The TDT approach corresponds to the mean-field case with the notable supplement that for very large step edge barriers one should deal with the time-dependent adatom density $\rho_1(r,t)$ (solution of eqs. (3.6),(3.7)) to calculate the nucleation rate $\Omega(R)$ from eq. (3.9). In the language of critical phenomena, one may regard $i = 2$ as the upper critical size of the critical nucleus above which mean-field theory becomes applicable. The existence of this upper critical size was not yet established in [RM99], and accordingly, the extension of the scaling arguments for the fluctuation-dominated situation to $i = 3$ was not allowed. The scaling arguments presented here and published in [HRM00] were generalized to nucleation on terraces with arbitrary dimensions d [Kru00]. In accordance with general trends in critical phenomena, fluctuations become less important in higher dimensions and the size of the upper

critical nucleus size, where fluctuations are important, decreases with increasing dimension d.

In the stochastic formulation presented below we will develop many of the necessary ingredients for the general treatment of second layer nucleation in the next sec. 3.5. Moreover, it is discussed under which conditions mean-field type expressions for local nucleation rates $\propto D\rho_1^{i+1}$ can be used.

3.4.1 Fundamental quantities

Nucleation rate $\Omega(R)$ and time scale $\Delta t(R)$

Based on a simplified stochastic description[RM99] we will argue that for small critical nuclei $i = 1, 2$ the mean number of atoms on top of the island is smaller than one and the stable nucleus is formed due to fluctuations. This gives rise to four scaling regimes in an $\alpha - \Gamma$ diagram, where $R_c \sim \Gamma^\gamma \alpha^\mu$ with different exponents γ and μ. For $i \geq 3$ by contrast, nucleation starts out from a situation with many atoms present on the island. Under these circumstances, three different scaling regimes can be identified, and two of them correspond to the ones predicted by the TDT approach. By comparing R_c with the mean distance l between islands on the substrate surface, the transition line separating rough multilayer from smooth layer-by-layer growth is identified in the $\alpha - \Gamma$ diagram. When the bond energies of unstable clusters become appreciable, the corresponding dissociation rates enter the problem as additional relevant parameters. It then becomes difficult to separate scaling regimes in practice, and the simplified stochastic description becomes of limited value. However, by employing the novel rate equation approach it is still possible to determine $f(t)$ and R_c in a simple manner.

In order to determine a second layer nucleation rate $\Omega(R)$ we start by considering a time interval $\Delta t(R)$, during which $R(t)$ does not change significantly. For example, for the generic growth law (2.7) we may require $\Delta t(R)$ to correspond to a 10% change of R, which would give $\Delta t(R) = 0.21(R/a)^2/[A^2 F a^2 \Gamma^{i/(i+2)}]$, i.e.

$$\Delta t(R) \sim F^{-1}\Gamma^{-i/(i+2)} R^2 \tag{3.15}$$

The nucleation rate $\Omega(R)$ is the mean number $n_{\text{nuc}}(R)$ of nucleation events in time $\Delta t(R)$ divided by $\Delta t(R)$,

$$\Omega(R) = \frac{n_{\text{nuc}}(R)}{\Delta t(R)} \,. \tag{3.16}$$

Encounter rate $\omega_n(R)$

A nucleation event occurs, if $i+1$ atoms encounter each other on nearest neighboring sites.

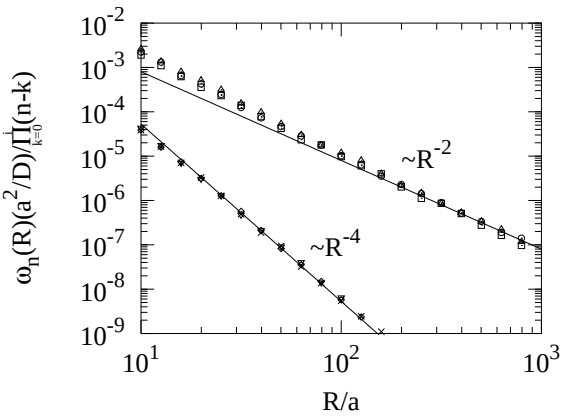

Figure 3.4: Scaled rate $\omega_n(R)(a^2/D)/\prod_{k=0}^{i}(n-k)$ of the encounter of $i+1$ atoms out of n atoms on an island with radius R and infinite step edge barrier. The upper curve with slope (-2) refers to $i=1$ and $n=2$ (□), 3 (○), and 4 (△), and the lower curve with slope (-4) refers to $i=2$ and $n=3$ (▽), 4 (◇), and 5 (×).

For an island with radius R and infinite step edge barrier ($\alpha = 0$), and in total n single atoms on top of it, let us approximate the encounter dynamics by a Poisson process, where $\omega_n(R)$ denotes the encounter rate of exactly $i+1$ atoms. Within the Poisson approximation this rate can be precisely defined as the inverse average time for $i+1$ atoms to encounter each other for the first time, when initially n atoms are randomly distributed on top of the island. A simple scaling argument yields

$$\omega_n(R) = \kappa_{\mathrm{e}} \left[\prod_{k=0}^{i}(n-k)\right] \frac{D}{a^2} \left(\frac{a^2}{\pi R^2}\right)^{i+1} \frac{\pi R^2}{a^2}\,, \tag{3.17}$$

where κ_{e} is a constant. The term $(a^2/\pi R^2)^{i+1}$ is proportional to the probability to find $i+1$ atoms on nearest neighbor sites, and the factor $(\pi R^2/a^2)$ takes into account that the encounter can occur everywhere on the island. The combinatorial factor $\prod_{k=0}^{i}(n-k)$ is slightly more subtle. At first sight, one may think that one should include the number $\binom{n}{i+1}$ of possibilities to choose any $i+1$ atoms out of the n atoms, but this is not correct, since the accumulation of $i+1$ atoms does not happen "in parallel" at a certain instant of time but in order: First a dimer forms out of n single atoms (combinatorial factor $n(n-1)/2$) and then some of the remaining $n-k$ atoms ($k = 2, 3, \ldots, i$) have to attach one after another to an intermediate cluster of size k before this cluster dissociates (the intermediate cluster is assumed to be much less mobile than single adatoms). The sequential attachment process yields an additional combinatorial factor $\prod_{k=2}^{i}(n-k)$. Clearly, the scaling argument gives only a rough approximation for $\omega_n(R)$ and a more refined treatment justifying eq. (3.17) is presented in Appendix A.1.

Determination of $\omega_n(R)$ for $i = 1, 2$ and various n in our simulations confirms

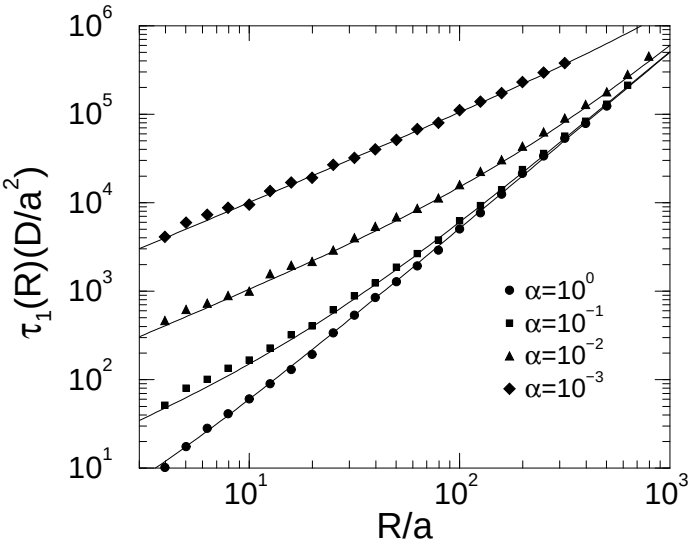

Figure 3.5: Lifetime $\tau_1(R)$ of a single atom on an island with radius R in units of a^2/D for various edge crossing probabilities $\alpha = \exp(-\Delta E_{\mathrm{S}}/k_{\mathrm{B}}T)$. The solid lines are drawn according to eq. (3.18) with $\kappa_1 = 1$ and $\kappa_2 = 1/2$.

the behavior predicted by eq. (3.17), see fig. 3.4. For $i = 1$ the scaling law is only valid for large $R \gtrsim 100a$, because at smaller R, two atoms typically encounter each other before the delta-functions characterizing the initial occupancy smear out to a uniform distribution (for larger i this effect becomes less important). Moreover, we find $\kappa_{\mathrm{e}} \cong 0.087$ for $i = 1$ and $\kappa_{\mathrm{e}} \cong 0.53$ for $i = 2$, i.e. the coefficient κ_{e} is constant for fixed i, but changes strongly with i. This dependence is expected, since we neglected the memory effect that, when n atoms, $2 \leq n \leq i$, are already close to each other, they keep close together for a while so that the encounter of i+1 atoms during this intermediate time becomes more likely. This memory effect is not included in the treatment in Appendix A.1, where after each "dissociation" of an unstable cluster of size $k \leq i$ a configuration is assumed to emerge, where a cluster of size $k-1$ is left and the remaining $n-k$ atoms are assumed to be randomly distributed. Accordingly, κ_{e} should increase with increasing i as it is the case.

Lifetime $\tau_n(R)$

Equation (3.17) has been derived for an infinite step edge barrier. For finite step edge barriers, we have to take into account that a state corresponding to an island with n atoms on top of it has a finite lifetime $\tau_n(R)$ only. This lifetime is defined by the average time required for the *first* of the n atoms to escape from the island (if any encounter processes are neglected). To a good approximation, $\tau_n(R)$ is the nth fraction of the lifetime $\tau_1(R)$ of a single atom, $\tau_n(R) \simeq \tau_1(R)/n$ (this

approximation would become exact, if the escape were a simple Poisson process). In the limit of large α, $\tau_1(R)$ is proportional to the characteristic time R^2/D for an atom to reach the boundary, while for small α an atom typically returns many times to the boundary before escaping from the island. Thus, in the latter limit, the characteristic escape rate (inverse lifetime τ_1^{-1}) is approximately given by the product of the probability $2\pi Ra/\pi R^2$ for the atom to be at the boundary and the rate $\alpha D/6a^2$ to overcome the step edge barrier. Combining these results gives

$$\tau_n(R) = \frac{1}{n}\frac{R^2}{D}\left(\kappa_1\frac{a}{\alpha R} + \kappa_2\right) , \tag{3.18}$$

where κ_1 and κ_2 are constants. Indeed, an exact solution of the corresponding diffusion problem [Har95] allows one to derive $\tau_n(R)$ exactly in the continuum limit, as we have shown in Appendix A.2. In particular, when the escape is approximated by a Poisson process, one finds $\kappa_1 \cong 1$ and $\kappa_2 = 1/2$ after proper renormalization and taking into account the lattice corrections (see Appendix A.2). Direct determination of $\tau_1(R)$ in our simulations confirms this result, see fig. 3.5.

Mean number of atoms $\bar{n}(R)$

Knowing $\tau_n(R)$ we can calculate the probability $p_n(R) = p_n(R(t))$ to find exactly n atoms on top of the island at time t *before* onset of second layer nucleation. This is achieved by considering the time evolution of $p_n(R(t))$, which is described by the master equation

$$\frac{dp_n}{dt} = \pi F R(t)^2 \left[(1-\delta_{n,0})p_{n-1} - p_n\right] + \frac{p_{n+1}}{\tau_{n+1}(R(t))} - \frac{p_n}{\tau_n(R(t))} \tag{3.19}$$

with the initial condition $p_n(0) = \delta_{n,0}$. Note that we have formally introduced p_{-1} and that $1/\tau_n \propto n$ so that the last term on the right hand side of (3.19) does not contribute for $n = 0$. As can be expected and is explicitly shown in Appendix A.2, the solution of eq. (3.20) is the Poisson distribution

$$p_n(R) = \frac{\bar{n}(R)^n}{n!}\exp[-\bar{n}(R)] , \tag{3.20}$$

where the mean number $\bar{n}(R)$ of atoms on top of the island *before* onset of nucleation is

$$\bar{n}(R) = \frac{2\pi}{A^2\Gamma^{\frac{i}{i+2}}}(1+\tilde{\alpha}R)^{-\varphi}\int_0^R dx\, x^3\,(1+\tilde{\alpha}x)^{\varphi} . \tag{3.21}$$

Here $\tilde{\alpha} \equiv \kappa_2\alpha/\kappa_1$ and $\varphi \equiv 2A^{-2}\Gamma^{2/(i+2)}/\kappa_2$. An explicit solution after evaluating the integral in eq. (3.21) is given in eq. (A.22) of Appendix A.2. For fixed α and Γ, three distinct R regimes can be identified from eq. (3.21): For $\varphi\tilde{\alpha}R \ll 1$ we can use $(1+\tilde{\alpha}x)^{\varphi} \simeq 1$ in (3.21), while for $\alpha R \ll 1$ but $\varphi\tilde{\alpha}R \gg 1$ we can use $(1+\tilde{\alpha}x)^{\varphi} \simeq \exp(\varphi\tilde{\alpha}x)$. For $\tilde{\alpha}R \gg 1$, we can set $(1+\tilde{\alpha}R) \simeq \tilde{\alpha}R$ in (3.21), and, since

the integral over x is dominated by the upper bound, $(1+\tilde{\alpha}x)\simeq\tilde{\alpha}x$ also. We thus obtain

$$\bar{n}(R) \sim \begin{cases} \Gamma^{-i/(i+2)}R^4\,, & R/a \ll \Gamma^{-2/(i+2)}\alpha^{-1} & \leftrightarrow\ \tau \sim R/\alpha D \gg \Delta t \\ \Gamma^{-1}\alpha^{-1}R^3\,, & \Gamma^{-2/(i+2)}\alpha^{-1} \ll R/a \ll \alpha^{-1} & \leftrightarrow\ \tau \sim R/\alpha D \ll \Delta t \\ \Gamma^{-1}R^4\,, & \alpha^{-1} \ll R/a & \leftrightarrow\ \tau \sim R^2/D \ll \Delta t \end{cases} \tag{3.22}$$

The two regimes for large R correspond to a quasi-stationary situation ($dp_n/dt=0$ in eq. (3.19)), where $p_n(R)$ from eq. (3.20) equals the stationary distribution for $R=R(t)$ with $\bar{n}(R)=\pi F R^2\tau_1(R)$. In these regimes the same result (3.22) can be obtained also by integrating $\rho_1^{\rm st}$ from eq. (3.8) over the island area. In fact, we used this connection to renormalize the constants κ_1 and κ_2 in eq. (3.18), see Appendix A.2. The small R regime in eq. (3.22) corresponds to a non-stationary situation, where p_n in general depends on the function $R(t')$ at all times $0\leq t'\leq t$ and not only on its value $R(t)$ at time $t'=t$. This fact, however, which also concerns the crossover value $R_\times\sim\Gamma^{-2/(i+2)}\alpha^{-1}$ to the non-stationary regime, is of minor importance here, since we consider the generic growth law (2.7) throughout the chapter. We thus can use R and t interchangeably. Note that the crossover from the non-stationary to the quasi-stationary situation occurs when $\tau_1(R_\times)\sim\Delta t(R_\times)$, that means in the non-stationary small R regime the changes in the radius occur on a faster scale than the escape of an atom from the island, $\Delta t(R)\ll\tau_1(R)$, while in the two quasi-stationary large R regimes $\Delta t(R)\gg\tau_1(R)$.

3.4.2 Nucleation Rates

Mean field nucleation rate

Let us now return to the different scenarios discussed in the introductory part of this Section. When $\bar{n}(R)\gtrsim i+1$, nucleation of a stable cluster can take place at any instant of time. The number of nucleation events in $\Delta t(R)$ that result from states with exactly n atoms on top of the island is proportional to $\omega_n(R)\Delta t(R)$. The total number of nucleation events $n_{\rm nuc}(R)$ is the weighted sum of $\omega_n(R)\Delta t(R)$ over n, i.e. we find $n_{\rm nuc}(R)=\sum_{n=i+1}^{\infty}p_n(R)\omega_n(R)\Delta t(R)$ with $p_n(R)$ given by eq. (3.20). [3] With eq. (3.16) we thus obtain for the mean-field nucleation rate

$$\begin{aligned}\Omega_{\rm mf}(R) &= \sum_{n=i+1}^{\infty} p_n(R)\,\omega_n(R) \\ &= \kappa_{\rm e}\,\frac{D}{a^2}\left(\frac{\bar{n}(R)}{\pi R^2}a^2\right)^{i+1}\left(\frac{\pi R^2}{a^2}\right)\,.\end{aligned} \tag{3.23}$$

[3] We are allowed to extend the sum up to infinity due to the sharp decrease of the Poisson distribution for $n\gg\bar{n}(R)$.

Equation (3.23) can be interpreted as resulting from a local nucleation rate $\propto D\rho_1^{i+1} = D[\bar{n}(R)/\pi R^2]^{i+1}$ integrated over the island area (factor πR^2). Compared to the TDT approach the radial variation of the diffusion profile $\rho_1 = \rho_1(r)$ is neglected in the stochastic description, so that $\Omega(R)$ from eq. (3.9) may be preferred over eq. (3.23). However, for small α, the profile in (3.8) becomes flat, in contrast to an exact calculation of the nucleation profile in a square[CP01], which shows a strongly enhanced nucleation probability in the center. In addition, as will be discussed further in sec. 3.4.4 below, for large α one should use the non-stationary solution of eqs. (3.6),(3.7) for calculating $\Omega(R)$ from (3.9) corresponding to the small R regime of $\bar{n}(R)$ in eq. (3.22).

Fluctuation dominated nucleation rate

More important, eq. (3.23) (or (3.9)) can be used only if $\bar{n}(R_c) \gtrsim i+1$ in the relevant time interval $\Delta t(R_c)$ at the onset of second layer nucleation. The stochastic description allows us to treat also the fluctuation dominated case, where $\bar{n}(R_c) \ll i+1$. In this situation $i+1$ adatoms have to be deposited and to encounter each other on the island. We can restrict our consideration to the deposition of exactly $i+1$ atoms, since for $\bar{n}(R_c) \ll i+1$, fluctuations corresponding to more than $i+1$ atoms on the island occur with a probability $\sum_{n=i+2}^{\infty} p_n(R) < \exp(1) p_{i+1}(R)\bar{n}(R)/(i+2) \ll p_{i+1}(R)$. If an atom is deposited on the island already containing i atoms, we view this as the start of a nucleation trial. The number $n_{\rm tr}(R)$ of nucleation trials in time $\Delta t(R)$ is $n_{\rm tr}(R) = \pi F R^2 \Delta t(R) p_i(R)$. For a trial to be successful, the $i+1$ atoms on the island right after its start have to encounter each other before any of the atoms escapes by passing the step-edge barrier. The probability $p_{\rm enc}(R)$ for this to happen is

$$p_{\rm enc}(R) = 1 - \exp[-\omega_{i+1}(R)\tau_{i+1}(R)]\,. \tag{3.24}$$

Accordingly, the total number $n_{\rm nuc}(R)$ of nucleation events in time $\Delta t(R)$ is now $n_{\rm nuc}(R) = n_{\rm tr}(R) p_{\rm enc}(R)$, and using eq. (3.16) we obtain for the fluctuation-dominated nucleation rate

$$\begin{aligned} \Omega_{\rm fl}(R) &= \pi F R^2\, p_i(R)\, p_{\rm enc}(R) \\ &= \pi F R^2 \frac{\bar{n}(R)^i}{i!} e^{-\bar{n}(R)} \Big(1 - \exp[-\omega_{i+1}(R)\tau_{i+1}(R)]\Big)\,. \end{aligned} \tag{3.25}$$

We note that in both formulae (3.23),(3.25) the only parameter not known a priori is the coefficient $\kappa_{\rm e}$, which has to be taken from simple simulations of the encounter process (see fig. 3.4 and the discussion above). Hence they do not require more input parameters than the expression (3.9) resulting from the TDT approach.

Self-consistency conditions

It remains to clarify under which conditions the mean-field or the fluctuation dominated situation occurs, i.e. when $\Omega_{\rm mf}(R)$ or $\Omega_{\rm fl}(R)$ has to be used as second layer nucleation rate. The answer to this question can be found by self-consistency requirements: Suppose first that the fluctuation dominated case takes place. Then, using (3.25), one can calculate the critical radius R_c and check if the condition $\bar{n}(R_c) \ll i+1$ is fulfilled. In addition, the condition $\omega_{i+1}(R_c)\Delta t(R_c) \gtrsim 1$ should also be fulfilled, since the encounter of $i+1$ atoms in the characteristic time $\omega_{i+1}(R_c)^{-1}$ should happen before R_c changes. If these necessary conditions for the fluctuation-dominated case are obeyed, then the mean-field situation is ruled out. This conclusion can be drawn, since $\bar{n}(R)$ is monotonously increasing with R, which implies that R_c following from $\Omega_{\rm fl}(R)$ is always smaller than R_c resulting from $\Omega_{\rm mf}(R)$. Hence, when the fluctuations are likely enough to initiate second layer nucleation, they lead to the formation of stable clusters at an earlier time t_c than that expected from the mean-field approach.

Using $\Omega_{\rm fl}(R)$ from eq. (3.25) or $\Omega_{\rm mf}(R)$ from eq. (3.23) we can determine the critical radius R_c (or, more precisely, R_c') by calculating $f(t)$ as in the TDT approach (see eq. (3.10)). However, for discussing the scaling of R_c with Γ and α, it is easier to obtain R_c from the condition

$$\Omega(R_c)\Delta t(R_c) \simeq 1\,, \tag{3.26}$$

which expresses the fact that the probability of second layer nucleation in $\Delta t(R_c)$ becomes of the order of one.

The following scaling analysis evaluates the relationships between R_c, α and Γ in terms of power laws. This is possible, because all relevant quantities can be expressed as powers of the three variables in appropriate limits. The expression for $\bar{n}$ in eq. 3.22 already has the form of power laws depending on scaling regions delimited by power law relations between the three variables. The encounter probability $p_{\rm enc} = 1-\exp[-\omega_{i+1}\tau_{i+1}]$ in $\Omega_{\rm fl}(R)$ also assumes the form of a power law *(i)* when $\omega_{i+1}\tau_{i+1} \to \infty$, so that $p_{\rm enc} = 1$, and *(ii)* when $\omega_{i+1}\tau_{i+1} \to 0$, one has $p_{\rm enc} = \omega_{i+1}\tau_{i+1}$. In case *(ii)* two different power law relationships are possible, depending on which scaling applies for τ_{i+1}. For $\Omega_{\rm fl}(R_c)$ there are now $3 \times (2+1) = 9$ possible candidate scaling regimes and the task is now to eliminate those combinations that are not self-consistent or violate the requirement $\omega_{i+1}(R_c)\Delta t(R_c) \gtrsim 1$. The valid regimes can be identified by starting with small α and tracking the transitions between scaling regimes caused by modified scaling with R, α and Γ in the factors $\bar{n}$ and $p_{\rm enc}$ when α is increased.

3.4.3 Small critical nuclei ($i = 1, 2$)

We will now show that the fluctuation-dominated case occurs for $i = 1, 2$. The detailed analysis is a bit technical and the reader, who is interested in the main

findings only, may skip the discussion of the various regimes I-IV in the following and proceed with the summary of the results given at the end of this section.

Since we consider the fluctuation-dominated case for small critical nuclei here ($i = 1, 2$), we assume $\bar{n}(R_c) \ll 1$ and thus set $\exp[-\bar{n}(R_c)] \simeq 1$, when inserting $\Omega_{\rm fl}(R_c)$ from eq. (3.25) into eq. (3.26). Starting from small α, four different regimes are predicted by eq. (3.26) with $\Omega(R_c) = \Omega_{\rm fl}(R_c)$:

Regime I: In the limit $\alpha \to 0$ we have $\bar{n}(R) \sim \Gamma^{-i/(i+2)} R^4$ and $\tau_{i+1} \to \infty$. Hence we obtain from eqs. (3.15),(3.25),(3.26) $F R_c^2 \Gamma^{-i^2/(i+2)} R_c^{4i} F^{-1} \Gamma^{-i/(i+2)} R_c^2 \sim R_c^{4(i+1)} \Gamma^{-i(i+1)/(i+2)} \sim$ const., i.e.

$$R_c \sim \Gamma^{i/[4(i+2)]} \tag{3.27}$$

From (3.27) follows $\bar{n}(R_c) \sim$ const., which means that the assumption of a fluctuation-dominated situation is not necessarily justified. In fact, eq. (3.27) appears here as the result of a rather lengthy calculation, but in the limit $\alpha \to 0$, the same scaling behavior (3.27) can be obtained very simply by calculating the average time needed for the deposition of $i+1$ atoms (see [RM99]). Hence, despite $\bar{n}(R_c) \simeq i+1$, eq. (3.27) gives the correct scaling behavior. However, eq. (3.27) predicts $\omega_{i+1}(R_c)\Delta t(R_c) \sim D R_c^{-2i} F^{-1} \Gamma^{-i/(i+2)} R_c^2 \sim \Gamma^{-(i^2-i-4)/[2(i+2)]}$ and since $\Gamma = D/Fa^4 \gg 1$, the inequality $\omega_{i+1}(R)\Delta t(R_c) \gtrsim 1$ becomes violated for $i \geq 3$ (if $\Gamma = D/Fa^4 \lesssim 1$ one would deal with a physical situation not considered in this work, where the mobility of adatoms is irrelevant). For $i \geq 3$ therefore, the condition $\omega_{i+1}(R_c)\Delta t(R_c) \sim 1$ should be used for calculating R_c, and because this yields $\bar{n}(R_c) > i+1$, one may alternatively use $\Omega_{\rm mf}(R_c)\Delta t(R_c) \simeq 1$ as the determining relation (see sec. 3.4.4).

Regime II: With increasing α, for $i \leq 2$, either the non-stationarity condition $\tau_1(R_c) \gg \Delta t(R_c)$ ($\bar{n}(R_c) \sim \Gamma^{-i/(i+2)} R_c^4$ in eq. (3.25)) or the condition $\omega_{i+1}(R_c)\tau_{i+1}(R_c) \gg 1$ ($p_{enc} \simeq 1$ in eq. (3.25)) breaks down first. Taking R_c from eq. (3.27), the first condition implies $\alpha \ll \Gamma^{-(i+8)/[4(i+2)]}$, while the second implies $\alpha \ll \Gamma^{-i(2i-1)/[4(i+2)]}$. Since the first condition is more restrictive for $i \leq 2$, regime I ceases to be valid when α becomes larger than $\Gamma^{-(i+8)/[4(i+2)]}$ and the quasi-stationarity situation is reached. In eq. (3.25) we now have to take $\bar{n}(R_c) = \pi F R^2 \tau_1(R) \sim \Gamma^{-1} \alpha^{-1} R^3$ (see eq. (3.22)) and it follows $\Omega_{\rm fl}(R_c)\Delta t(R_c) \sim \alpha^{-i} \Gamma^{-i(i+3)/(i+2)} R_c^{3i+4} \sim$ const., i.e.

$$R_c \sim \alpha^{i/(3i+4)} \Gamma^{i(i+3)/[(i+2)(3i+4)]} \,. \tag{3.28}$$

Since $\bar{n}(R_c) \sim (\Gamma^{-(i+8)/4(i+2)} \alpha^{-1})^{4/(3i+4)} \ll 1$ the condition for a fluctuation-dominated situation is fulfilled, and since $\Delta t(R_c) \gg \tau_1(R_c) \simeq \tau_{i+1}(R_c)$ and $\omega_{i+1}(R_c)\tau_{i+1}(R_c) \gg 1$ the condition $\omega_{i+1}(R_c)\Delta t(R_c) \gtrsim 1$ is obeyed too.

Regime III: By further increasing α we obtain $\omega_{i+1}(R_c)\tau_{i+1}(R_c) \ll 1$ for $\alpha \gg \Gamma^{-i(i+3)(2i-1)/[2(i+2)(i^2+i+2)]}$. Hence we now have to use $p_{enc} \simeq \omega_{i+1}(R_c)\tau_{i+1}(R_c)$ when inserting eq. (3.25) into eq. (3.26) and find

$$R_c \sim \alpha^{(i+1)/(i+5)} \Gamma^{i(i+3)/[(i+2)(i+5)]} \,. \tag{3.29}$$

The condition $\bar{n}(R_c) \sim \Gamma^{-1}\alpha^{-1}R_c^3 \ll 1$ requires $\alpha^{i-1} \ll \Gamma^{-(i^2+i-5)/(i+2)}$ and is fulfilled for $i=1$. For $i=2$, it is valid for $\alpha \ll \Gamma^{-1/4} \sim a/R_c$. The second requirement $\omega_{i+1}(R_c)\Delta t(R_c) \gtrsim 1$ gives $\alpha^{i-1} \ll \Gamma^{-(i^3+2i^2-4i-5)/[(i+1)(i+2)]}$ and again is obeyed for $i=1$ and valid for $i=2$ as long as $\alpha \ll \Gamma^{-1/4} \sim a/R_c$.

Regime IV: In this last regime α becomes larger than a/R_c, that means eq. (3.29) predicts the regime to occur for $\alpha \gg \Gamma^{-i/[2(i+2)]}$. Taking $\bar{n}(R_c) \sim \Gamma^{-1}R_c^4$ from eq. (3.22) and $\omega_{i+1}(R_c)\tau_{i+1}(R_c) \sim R_c^{-2(i-1)}$ from eqs. (3.17),(3.18), we find

$$R_c \sim \Gamma^{i/[2(i+2)]} \,. \tag{3.30}$$

We used $\omega_{i+1}(R_c)\tau_{i+1}(R_c) \ll 1$ ($p_{\text{enc}}(R_c) \ll 1$) to derive (3.30), which for $i=2$ is valid and for $i=1$ is obeyed when taking into account the prefactors (for $i=1$, $\omega_{i+1}(R_c)\tau_{i+1}(R_c) = \kappa_{\text{e}}\kappa_2$, where κ_2 is the coefficient defined in eq. (3.18)). Moreover, eq. (3.30) gives $\bar{n}(R_c) \sim \Gamma^{(i-2)/(i+2)}$, which is much smaller than one for $i=1$. For $i=2$, a decision on whether the fluctuation-dominated or the mean-field situation occurs would require a closer inspection of the prefactors (in the present case we find the mean-field description to be the adequate one). However, since for $\alpha \gg a/R_c$ one finds the same scaling (3.30) in the mean-field situation (see sec. 3.4.4), eq. (3.30) is valid in any case. The second condition $\omega_{i+1}(R_c)\Delta t(R_c) \gtrsim 1$ is fulfilled for $i=1$, and for $i=2$ the situation again depends on the prefactors.

In summary we have found that the second layer nucleation for $i=1,2$ occurs due to various mechanisms in four distinct regimes I-IV: In regime I ($\alpha \ll \Gamma^{-(i+8)/[4(i+2)]}$), the nucleation takes place once $i+1$ atoms have been deposited on the island, in regime II ($\Gamma^{-(i+8)/[4(i+2)]} \ll \alpha \ll \Gamma^{-i(i+3)(2i-1)/[2(i+2)(i^2+i+2)]}$) the loss of atoms becomes important and the nucleation takes place once the probability for finding $i+1$ atoms on the island at some time instant in $\Delta t(R)$ becomes of the order of one, in regime III ($\Gamma^{-i(i+3)(2i-1)/[2(i+2)(i^2+i+2)]} \ll \alpha \ll \Gamma^{-i/[2(i+2)]}$) the probability p_{enc} for the encounter of $i+1$ atoms during a nucleation trial has to be taken into account in addition to the probability for the occurrence of $i+1$ atoms, and in regime IV ($\alpha \gg \Gamma^{-i/[2(i+2)]}$) both the occurrence and encounter probability matter but these probabilities no longer depend on the step edge barrier. For convenient reference, we provide the exponents γ and μ defined in eq. (3.12) and their corresponding ranges of validity in table 3.1. When comparing the scaling in the fluctuation-dominated situation with that predicted by eqs. (3.13),(3.14) of the TDT approach it is remarkable that the same behavior is found in regime III and IV. We believe this to be caused by the fortunate circumstance that local nucleation rates of form $\propto D\rho_1^{i+1}$ might be *effectively* applicable even if the requirements for the mean-field situation are not fulfilled (see however [KKW98]).

Moreover, we have to note that for $i=1$ the lower and upper crossovers α_2 and α_3 specifying regime III (see table 3.1) both scale as $\Gamma^{-1/6}$. This is due to the fact that when $\omega_{i+1}(R_c)\tau_{i+1}(R_c)$ becomes less than one, we already obtain $\alpha \gg a/R_c$,

Regime	$\bar{n}$	$p_{\mathrm{nuc}}(R_c)$	γ	μ
I	$\tau \sim R/\alpha D \gg \Delta t$	1	$i/4(i+2)$	0
II	$\tau \sim R/\alpha D \ll \Delta t$	1	$i(i+3)/(i+2)(3i+4)$	$i/(3i+4)$
III	$\tau \sim R/\alpha D \ll \Delta t$	$\omega_{i+1}\tau_{i+1}$	$i(i+3)/(i+2)(i+5)$	$(i+1)/(i+5)$
IV	$\tau \sim R^2/D \ll \Delta t$	$\omega_{i+1}\tau_{i+1}$	$i/2(i+2)$	0

Table 3.1: The exponents γ and μ characterizing the scaling $R_c \sim \Gamma^{\gamma}\alpha^{\mu}$ in the regimes I-IV for increasing α ($0 \leq \alpha \leq 1$) and $i=1,2$. The crossover values scale as $\alpha_k \sim \Gamma^{-\delta_k}$ where $\delta_{\mathrm{I}\to\,\mathrm{II}} \equiv (i+8)/4(i+2)$, $\delta_{\mathrm{II}\to\,\mathrm{III}} \equiv i(i+3)(2i-1)/2(i+2)(i^2+i+2)$, and $\delta_{\mathrm{III}\to\,\mathrm{IV}} \equiv i/2(i+2)$. For example, regime II can be found for $\Gamma^{-\delta_{\mathrm{I}\to\,\mathrm{II}}} \ll \alpha \ll \Gamma^{-\delta_{\mathrm{II}\to\,\mathrm{III}}}$.

Regime	$\bar{n}$	γ	μ
I	$\tau \sim R/\alpha D \gg \Delta t$	$(i-1)/2(i+3)$	0
II	$\tau \sim R/\alpha D \ll \Delta t$	$i(i+3)/(i+2)(i+5)$	$(i+1)/(i+5)$
III	$\tau \sim R^2/D \ll \Delta t$	$i/2(i+2)$	0

Table 3.2: The exponents γ and μ characterizing the scaling $R_c \sim \Gamma^{\gamma}\alpha^{\mu}$ in the regimes I-III for increasing α and $i \geq 3$. The crossover values scale as $\alpha_k \sim \Gamma^{-\delta_k}$, where $\delta_{\mathrm{I}\to\,\mathrm{II}} \equiv (i^2+5i+10)/2(i+2)(i+3)$, and $\delta_{\mathrm{II}\to\,\mathrm{III}} \equiv i/2(i+2)$. For example, regime II can be found for $\Gamma^{-\delta_{\mathrm{I}\to\,\mathrm{II}}} \ll \alpha \ll \Gamma^{-\delta_{\mathrm{II}\to\,\mathrm{III}}}$.

which is the condition for regime IV. Nevertheless, due to the pronounced small R corrections to eq. (3.17) for $i=1$ (see fig. 3.4) both conditions $\omega_{i+1}(R_c)\tau_{i+1}(R_c) \ll 1$ and $\alpha \ll a/R_c$ can be fulfilled in a small transient regime III. However, for $i=1$ this is no longer a true scaling regime, where a simple power law dependence of R_c on Γ and α can be identified. In this respect, the small α regime of the TDT approach does not occur for $i=1$, also not at larger α.

Comparison with simulations for i=1,2

Taking Ω_{fl} from eq. (3.25) we can calculate $f(t)$ according to eq. (3.10). Representative results for $i=1$ are shown in fig. 3.2 (dashed lines), and the comparison with the Monte Carlo data yields a very good agreement. The R_c values derived from $f(t)$ are plotted as a function of α for Γ values in the range $10^5 - 10^8$ in fig. 3.6. Note that, compared to the results of the full island model shown in fig. 3.3, the data cover the full α range from zero to one, since the restrictions imposed by island coalescence in the multi-island model are not present in the single-island model (see also the discussion in sec. 3.2 above). Moreover the simpler single-island model allows one to explore the behavior for larger Γ values in the range $\Gamma = 10^9 - 10^{12}$ also. It is possible to fit the R_c curves over the entire

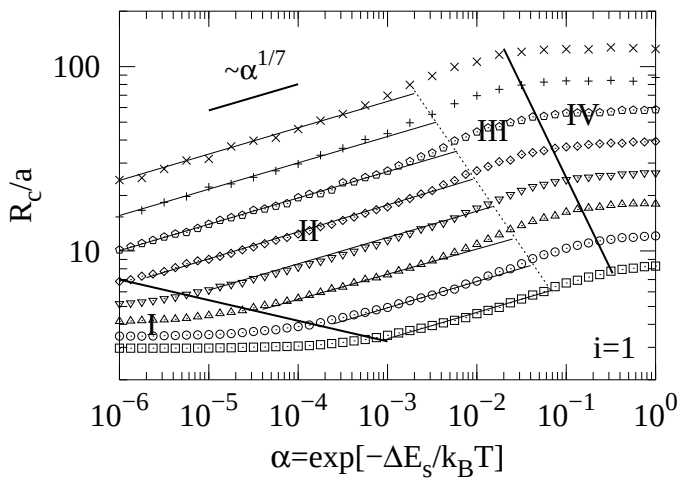

Figure 3.6: Critical island size R_c as a function of α obtained from simulation of the single-island model for 8 different Γ values starting from 10^5 ($\square$) and ending at 10^{12} ($\times$). Between these values, Γ is increased by a factor of 10. The various regimes I-IV are indicated together with the border line with slope (-1/9) between regimes I and II and the border line with slope (-1) between regimes III and IV. The dashed border line separating the transient regime III from regime II was calculated numerically from the condition $\omega_2(R_c)\tau_2(R_c) \simeq 1$ (see text).

range of α and Γ values (see sec. 3.5.2) but we focus on the scaling behavior of R_c in the following in order to demonstrate the various scaling regimes associated with the different physical mechanisms of second layer nucleation.

Indeed, the simulated data in fig. 3.6 confirm the theoretical predictions. For small $\alpha \ll \alpha_{\mathrm{I}\to\,\mathrm{II}}$ (regime I), R_c is independent of α, while for $\alpha \gg \alpha_{\mathrm{I}\to\,\mathrm{II}} \sim \Gamma^{-3/4}$ (regime II) we find $R_c \sim \Gamma^{4/21}\alpha^{1/7}$. Since $R_c(\alpha_1) \sim \alpha_{\mathrm{I}\to\,\mathrm{II}}^{-1/9}$ at the crossover, the boundary line between regimes I and II has slope (-1/9). The correctness of the scaling of R_c with Γ in regimes I and II can be deduced from the offset of the curves for various Γ in fig. 3.6 (alternatively, one can collapse the data onto a common master curve by a proper rescaling as it was shown in [RM99]). Regime II is followed by the transient regime III, and the dashed border line separating regime III from regime II was determined numerically from the condition $\omega_2(R_c)\tau_2(R_c) \simeq 1$ by using the results for $\omega_2(R_c)$ and $\tau_2(R_c)$ displayed in figs. 3.4,3.5. For $\alpha \gg \Gamma^{-i/[2(i+2)]}$ (regime IV), we find $R_c \sim \Gamma^{i/[2(i+2)]}$ independent of α, and the boundary line between regimes III and IV has slope (-1). Figure 3.7 depicts the various regions characterizing the mechanism of second layer nucleation for $i = 1$ in an $\alpha - \Gamma$ diagram[RM99]. Varying Γ and α within one of the regions results in the corresponding behavior of R_c according to eqs. (3.27),(3.28),(3.30). The border line between regions I and II has slope $(-4/3)$, between regions III and IV slope (-6), and the dashed line marks the border line between regions II and III. In

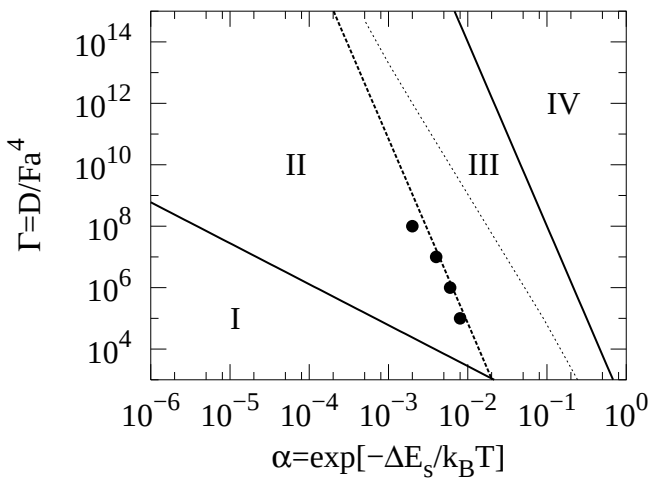

Figure 3.7: The various regions characterizing the mechanism of second layer nucleation for $i=1$ in an $\alpha-\Gamma$ diagram. The thick dashed line with slope (-6) marks the onset of layer-by-layer growth (the circles refer to the onset of island coalescence obtained in the full simulation, see fig. 3.3).

addition, we have drawn the transition line from rough multilayer to smooth layer-by-layer growth into the diagram. In our simulations island coalescence occurs in regime II (see fig. 3.3), where $R_c \sim \Gamma^{4/21}\alpha^{1/7}$. The criterion $R_c \simeq l \sim \rho_x^{-1/2} \sim \Gamma^{1/6}$ thus yields $\alpha_\star(\Gamma) \sim \Gamma^{-1/6}$[Rot99].

Results for R_c obtained from simulations for a critical nucleus of size $i = 2$ are shown in fig. 3.8. Again the results confirm the predictions of the theory. In particular, for large Γ, the exponents $\mu = 1/5$ in regime II and $\mu = 3/7$ in regime III can be clearly identified. In contrast to the behavior for $i=1$ shown in fig. 3.6, regime III develops into a full scaling regime.

3.4.4 Large critical nuclei ($i \geq 3$)

Analogous to the fluctuation-dominated case treated in the previous subsection we can obtain the scaling of R_c with Γ and α from the condition $\Omega_{\rm mf}(R_c)\Delta t(R_c) \simeq 1$ with $\Omega_{\rm mf}(R)$ and $\Delta t(R_c)$ from eqs. (3.23),(3.15), respectively. For critical island radii belonging to the two quasi-stationary large R-regimes in eq. (3.22) this gives the same behavior (3.13),(3.14) as predicted by the TDT approach. However, for large step edge barriers corresponding to the non-stationary small α-regime in eq. (3.22) we find

$$\Omega_{\rm mf}(R_c)\Delta t(R_c) \sim D(\Gamma^{-i/(i+2)}R_c^4)^{i+1}R_c^{-2i}F^{-1}\Gamma^{-i/(i+2)}R_c^2 \sim R_c^{2(i+3)}\Gamma^{-(i-1)} \sim \text{const., i.e.}$$

$$R_c \sim \Gamma^{(i-1)/[2(i+3)]}\,. \tag{3.31}$$

With increasing α this scaling breaks down when R_c enters the quasi-stationary

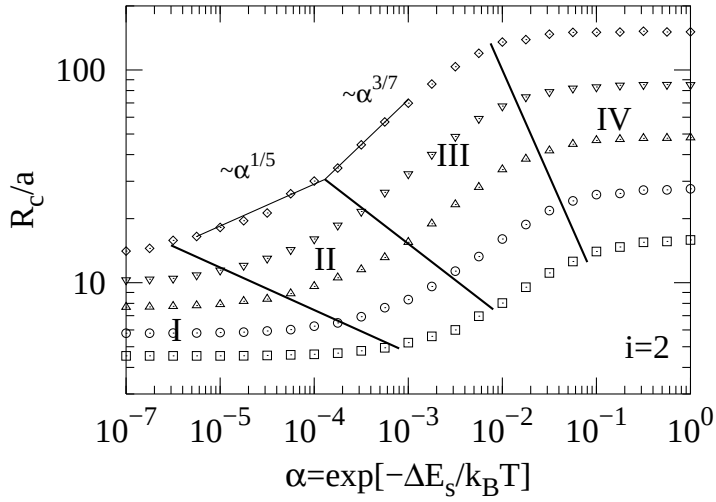

Figure 3.8: Critical island size R_c for $i=2$ obtained from the single-island model for 5 different Γ values between 10^5 (□) and 10^9 (◇). Between these values, Γ is increased by a factor of 10. The scaling regimes I-IV are indicated together with the respective border lines with slope (-1/5) between regimes I and II, slope (-1/3) between regime II and III and slope (-1) between regimes III and IV.

regime in eq. (3.22) that means for $\alpha \gg \Gamma^{-2/(i+2)} R_c^{-1} \sim \Gamma^{-(i^2+5i+10)/[2(i+2)(i+3)]}$.

For $i \geq 3$ we thus have in total three distinct regimes I-III with different mechanisms for second layer nucleation: In regime I ($\alpha \ll \Gamma^{-(i^2+5i+10)/[2(i+2)(i+3)]}$) the nucleation takes place once the island radius R has grown large enough so that the encounter of $i+1$ atoms out of typically $\bar{n}(R) \gtrsim i+1$ atoms happens in a time comparable to $\Delta t(R)$, in regime II $\bar{n}(R)$ becomes dependent on α, while in regime III, for large $\alpha \gg a/R_c$, $\tau_1(R)$ no longer depends on the step edge barrier and $\bar{n}(R)$ becomes independent of α again. The overall behavior characterized by the scaling exponents γ and μ is summarized in table 3.2 on page 34. Computer simulations for $i=3$ are in accordance with these theoretical predictions, see fig. 3.9. The predicted scaling $R_c \sim \alpha^{1/2}$ in regime II is not yet fully developed for the Γ-values in the range $10^5 - 10^8$ but it can be expected to become more clearly visible for larger Γ. However, we could not obtain reliable simulation results for larger Γ values, since the amount of CPU time for determining the onset of second layer nucleation becomes tremendous due to the increasing number of atoms contributing to the nucleation event.

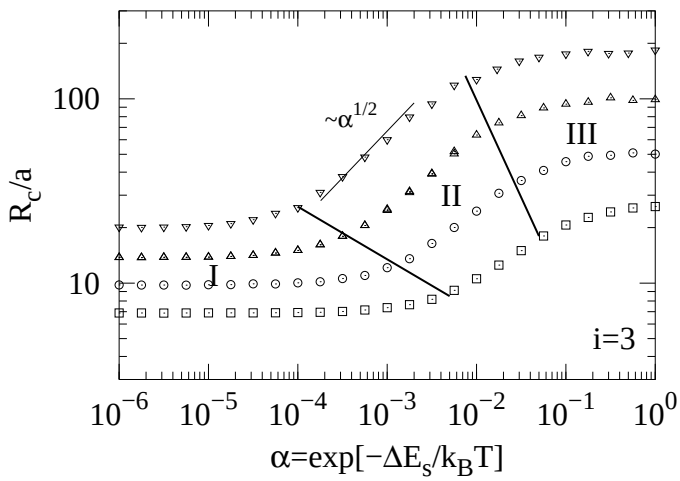

Figure 3.9: Critical island size R_c for $i = 3$ obtained from the single-island model for 4 different Γ values between 10^5 (□) and 10^8 (▽). The scaling regimes I-III are indicated together with the respective border lines with slope (-5/17) between regimes I and II and slope (-1) between regimes II and III.

3.5 Rate equation theory

In a more general approach to the problem of second layer nucleation we distinguish between different individual states of the island during its growth with respect to the number of atoms that are on top of the island and the way a given number of atoms is decomposed into clusters of various sizes. Employing a Poisson approximation, the transition processes between the states exhibit no (intrinsic) memory and can be characterized by elementary rates. For the non-interacting particle model these elementary transition rates are the deposition rate $\pi F R^2$, the rate for the attachments of a single atom to an intermediate cluster of size k, and the loss rate of adatoms. The latter is given by the inverse lifetime τ_1^{-1} of a single atom (see eq. (3.18)). Dissociation rates enter the problem as additional parameters, when the lifetimes of intermediate metastable clusters cannot be neglected. The consequences of such dissociation rates will be discussed in sec. 3.6.1. First, however, we will present the general procedure in the next section and show in sec. 3.5.2 how the results of the simplified stochastic description in sec. 3.4 can be recovered. In addition to these previously derived results, it is also discussed how the general treatment allows one to gain detailed insight into the dominant microscopic pathways that are followed to form a stable nucleus on top of the island.

3.5.1 General Procedure

Let us introduce a common notation for the elementary transition rates: W_{F} for the deposition rate, W_{l} for the loss rate, $W_{\mathrm{a},j}^{(n)}$ for the attachment rate for a single atom to an intermediate cluster of size j if in total n atoms are present on top of the island (see eq. A.1 in Appendix A.1; we formally include the case $j=1$), and $W_{\mathrm{d},j}$ for the dissociation rate of an unstable cluster composed of $j \leq i$ atoms (again we do not distinguish between different cluster configurations for the same cluster size, see also the definition in sec. 2.2). According to the results derived in sec. 3.4.1 and Appendix A.1 the transition rates are

$$W_{\mathrm{F}} = \pi F R^2 \,, \tag{3.32}$$

$$W_{\mathrm{l}} = \frac{D}{R^2} \left(\kappa_1 \frac{a}{\alpha R} + \kappa_2 \right)^{-1} , \tag{3.33}$$

$$W_{\mathrm{a},j}^{(n)} = \kappa_{\mathrm{a,j}}^{(n)} \begin{cases} \dfrac{n(n-1)}{2} \dfrac{2D}{\pi R^2} \,, & j=1 \\ (n-j) \dfrac{D}{\pi R^2} \,, & 2 \leq j \leq n \end{cases} \tag{3.34}$$

$$W_{\mathrm{d},j} = \kappa_{\mathrm{d,j}} \frac{D}{a^2} \exp\left(-\frac{\Delta E_j^{\mathrm{dis}}}{k_{\mathrm{B}} T} \right) , \quad 2 \leq j \leq i \,, \tag{3.35}$$

where $\Delta E_j^{\rm dis} = E_j^{\rm dis} - E_0$ is the dissociation energy of a *single* atom from an unstable cluster of size $j \leq i$. The prefactors $\kappa_{\rm a,j}^{(n)}$ and $\kappa_{\rm d,j}$ contain the effective sizes of cluster perimeters on one hand (see the discussion in Appendix A.1), and various corrections involved in the overall approximation scheme (Poisson approximation, cutoff $n_\star$ introduced below, etc.); they are considered to be independent of D, α and R. In principle one should also take into account the possibility that a subcluster composed of more than one atom can dissociate from an unstable cluster. In fact, it has been argued that such cluster dissociations are sometimes more likely to occur than the dissociation of single atoms, as e.g. for dimer dissociation from a tetramer on a (100) surface by a kind of "shearing mode" [SZSW96]. For simplicity we will take into account only the dissociation of single atoms here, although conceptually the inclusion of cluster dissociation processes into the general treatment poses no difficulty. Also, we do not consider the influence of cluster mobilities. If one would allow for a small jump rate D_j/a^2 of a cluster of size $j \geq 2$, the relative diffusion of a j cluster and a single atom would be larger by a factor $1 + D_j/D$ and accordingly we had to multiply $W_{{\rm a},j}^{(n)}$ in eq. (3.34) by this factor for $j \geq 2$.

The method is best introduced by an example. To this end, consider fig. 3.10 that illustrates the situation for a critical nucleus of size $i = 2$. Various states of the island are shown, which are distinguished according to the total number n of

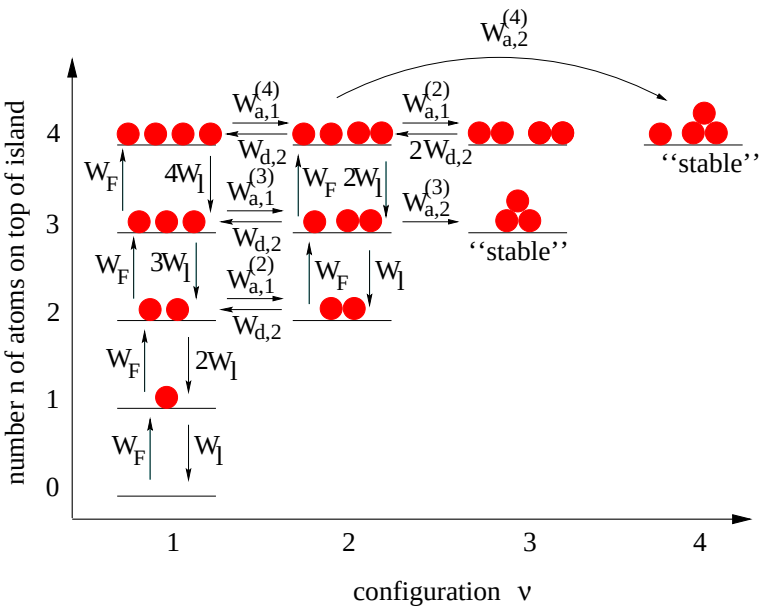

Figure 3.10: Various states and the corresponding transition rates (see eqs. (3.32)–(3.35)) involved in the second layer nucleation for a critical nucleus of size $i = 2$. Configurations with two atoms in a cluster are metastable, while configurations with three atoms in a cluster are stable.

atoms on top of the island, and the possible configurations that can be assumed for a given n. Between the states the possible transitions are marked by arrows that are labeled by the corresponding rates. Note that the loss from a state with n single atoms is n times larger than the loss from the state with one atom. It is clear that fig. 3.10 shows only a small part of the possible states and in principle can be extended by including larger numbers n. However, as will be pointed out below, these states with larger n do not contribute much to the onset of second layer nucleation. Moreover, we have not included states containing stable clusters of size $j > i+1$ and transitions between different states containing a stable nucleus of size $i+1$. These are irrelevant for the fraction $f(t)$ of covered islands at time t.

We denote by $p_{n,\nu}$ the probability for the island to be in state (n, ν), where n refers to the number of atoms on top of the island and ν to a specific configuration for a given n (see again fig. 3.10). A complete description of the stochastic process amounts to specifying the set $\{p_{n,\nu}(t)\}$ of state probabilities at all times t. The time evolution of the $\{p_{n,\nu}(t)\}$ is described by the master equation

$$\frac{dp_{n,\nu}}{dt} = \sum_{n',\nu'} \left[W(n', \nu' \to n, \nu)\, p_{n',\nu'} - W(n, \nu \to n', \nu')\, p_{n,\nu} \right] , \tag{3.36}$$

where for the rates $W(n, \nu \to n', \nu')$ the appropriate expressions from eqs. (3.32)–(3.35) have to be substituted. Note that transitions are possible only between a limited number of states. In the situation considered here, where only single atoms can leave the island, we have $W(n, \nu \to n', \nu') = 0$ for $|n - n'| \geq 2$.

To treat the problem of second layer nucleation under generic growth conditions one has to solve the set of eqs. (3.36) for $R = R(t)$ with $R(t)$ from eq. (2.7) subject to the initial condition $p_{n,\nu} = \delta_{n,0}$. To this end it is convenient to solve (3.36) using R as the independent variable. The integration of the differential equations (3.36) using standard solvers takes very little CPU time on ordinary workstations, so that results for $f(t)$ and $R_c(\alpha)$ can be obtained almost immediately. Numerical results are discussed in the following.

The approach outlined above provides a general framework to treat the problem of second layer nucleation and may be applied and extended to a variety of situations. It furthermore allows one to gain detailed insight into the microscopic pathways followed during the nucleation process.

3.5.2 Negligible Lifetimes of Unstable Clusters

In this subsection we consider the case $\Delta E_j^{\mathrm{dis}} = 0$ that was treated extensively in sec. 3.4. The fraction $f(t)$ of covered islands within our more general framework is given by

$$f(t) = \sum_{n=i+1}^{\infty} p_{n,\nu_n}(t) , \tag{3.37}$$

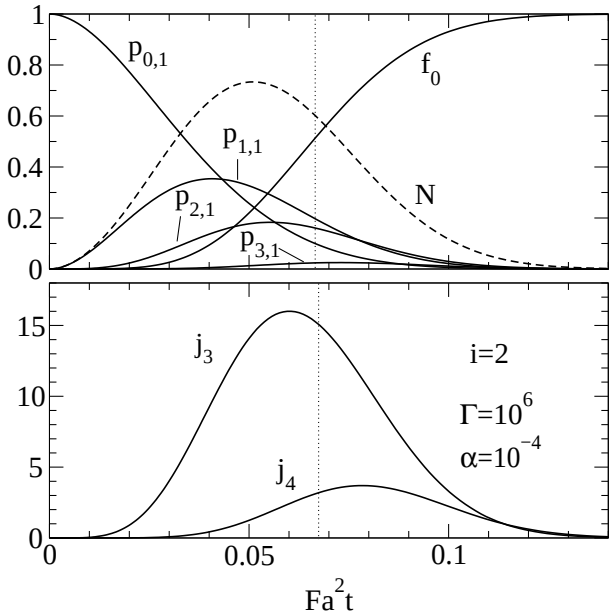

Figure 3.11: Time development of the fraction of covered islands $f(t)$, the mean number of atoms $N(t)$ in states containing no stable nucleus, the occupation probabilities $p_{n,1}$, and the currents j_3 and j_4 (see eq. 3.39) for $i=2$, $\alpha = 10^{-4}$ and $\Gamma = 10^6$. The maximum number of atoms is $n_\star = 4$ corresponding to the diagram shown in fig. 3.10. The vertical dotted line marks the coverage Fa^2t_c at the critical time t_c.

where ν_n is the configuration containing a stable nucleus for a given n (for example, $\nu_3 = 3$ and $\nu_4 = 4$ in fig. 3.10). Since we do not distinguish between possible substates of stable configurations for given n (e.g. clusters of three or four atoms in fig. 3.10), a single configuration ν_n is stable for each n. In practice, states corresponding to large n contribute a negligible amount up to times t_c, so that one needs to consider a finite maximum number of atoms $n_\star$ only ($n_\star = 4$ in fig. 3.10 turned out to be sufficient).

Figure 3.11a shows $f(t)$ and the probabilities $p_{n,\nu}(t)$ (labeled according to fig. 3.10) as a function of the coverage Fa^2t for $\alpha = 10^{-4}$, and $\Gamma = 10^6$. Also shown is the mean total number

$$N(t) \equiv \sum_{n=1}^{n_\star} \sum_{\nu \neq \nu_n} p_{n,\nu}(t)\, n \tag{3.38}$$

of atoms that are not in states possessing a stable nucleus. In accordance with the predictions of the simplified stochastic description, this number is less than one up to time t_c. Accordingly, the pathway followed by the system to form a stable nucleus is dominated by fluctuations as discussed in sec. 3.4. The important role of the fluctuations can even more clearly be recognized by looking at the state

probabilities $p_{n,\nu}$, $\nu \neq \nu_n$, and the currents

$$j_3(t) \equiv W^{(3)}_{\mathrm{a},2}\, p_{3,2}(t)\,, \qquad j_4(t) \equiv W^{(4)}_{\mathrm{a},2}\, p_{4,2}(t) \tag{3.39}$$

into the states containing a stable nucleus. As can be seen from fig. 3.11a, only the probabilities $p_{n,1}(t)$ are significant, while the other state probabilities $p_{n,2}(t)$ and $p_{4,3}(t)$ cannot be discerned on the scale used in the figure. On the other hand, we find that the current $j_3(t)$ from the state $(n=3, \nu=2)$ (which has a very small probability $p_{3,2}(t)$) contributes most to the growth of $f(t)$, see fig. 3.11b. The fact that $j_4(t)$ gives only a subdominant contribution to second layer nucleation, indicates that the incorporation of states with $n>5$ will not significantly change the behavior of $f(t)$.

The results for $f(t)$ compare well with the data obtained from kinetic Monte Carlo simulations, the quality of agreement between theory and simulation being as good as in fig. 3.2. The values of the optimal prefactors entering the transition rates displayed in fig. 3.10 are for $i=2$: $\kappa^{(2)}_{\mathrm{a},1} = 0.9$, $\kappa^{(3)}_{\mathrm{a},1} = 0.3$, $\kappa^{(3)}_{\mathrm{a},2} = 3$, $\kappa^{(4)}_{\mathrm{a},1} = 11$, $\kappa^{(4)}_{\mathrm{a},2} = 3$, and $\kappa_{\mathrm{d},2} = 0.5$. The relatively large factor $\kappa^{(4)}_{\mathrm{a},1} = 11$ may be understood as effectively taking into account the additional pathways resulting from states with $n > n_\star = 4$. For $i=1$ we found $\kappa^{(2)}_{\mathrm{a},1} = 1$ to give an optimal fit for a reduced diagram, in which only the states with $n \leq 2$ from fig. 3.10 are taken into account.

To exemplify the good agreement between theory and simulations, we have re-plotted in fig. 3.12 the critical radius R_c as a function of α for various Γ for $i = 1, 2$ from figs. 3.6,3.8. The solid lines referring to the numerical results give an excellent fit to the Monte Carlo data. For $i=1$, only the states with $n \leq 2$ in fig. 3.10 had to be included to achieve this almost perfect agreement.

For $i > 2$ we expect that a very large number $n_\star$ has to be chosen in order to obtain a correct description of second layer nucleation within the rate equation approach. Diagrams corresponding to that shown in fig. 3.10 then become very complicated and not easily tractable from the practical point of view. It is thus helpful to introduce the "renormalized" encounter rates ω_n defined in eq. (3.17) and to consider simplified diagrams as shown in fig. 3.13 for $i = 3$. For a given number $n \geq i+1$ of atoms on top of the island we have only included two states $\nu = 1, 2$: One of these refers to a state where all n atoms are separated ($\nu = 1$), and the other one to a state, where exactly $i+1$ atoms form a stable nucleus, while the remaining $n-(i+1)$ atoms are not bound to other atoms in the same layer ($\nu=2$).

Plots of $f(t)$, $p_{n,1}(t)$, $N(t)$, and $j_n(t) \equiv p_{n,1}(t)\omega_n(R(t))$ for $i = 3$ analogous to fig. 3.11 are shown in fig. 3.14. As expected from the discussion in sec. 3.4, we now had to take into account states with n up to $n_\star = 50 \gg i(i+1)/2 = 6$ before reaching the limit, where $f(t)$ as calculated from eq. (3.37) did not change much by incorporation of states with larger n. Near t_c, $N(t)$ is significantly larger than $i+1 = 4$ (at t_c we find $N(t_c) \cong 10$), and the dominant currents $j_n(t)$ initiating second layer nucleation are those for $n \simeq 15 \ldots 20 \gg 4$, see fig. 3.14.

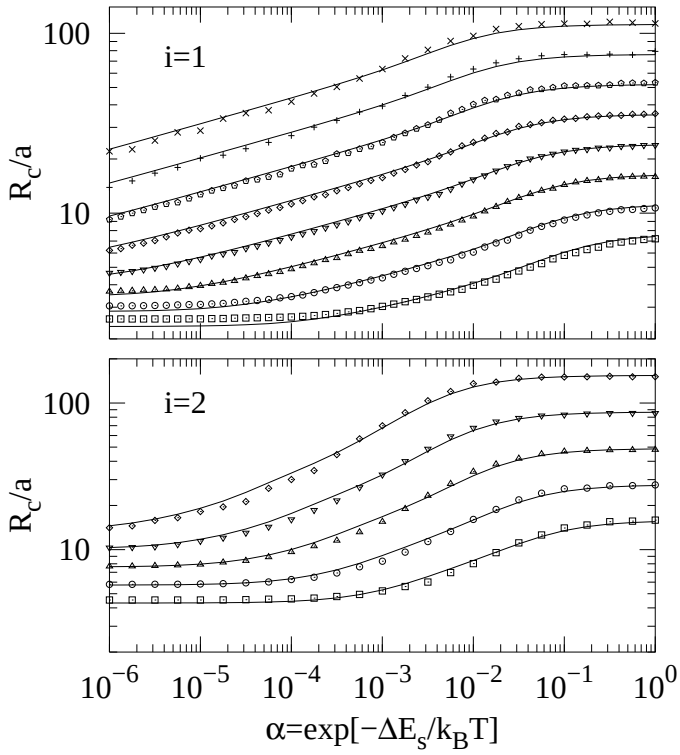

Figure 3.12: Comparison of critical island sizes R_c obtained from the rate-equation approach (solid lines) with Monte Carlo data for critical nuclei $i = 1, 2$ and different values of Γ (same symbols as in figs. 3.6,3.8).

In order to see how the preferred paths for second layer nucleation change with the step crossing probability α, we define the integrated current $j_n(t)$ up to t_c by

$$J_n \equiv \int_0^{t_c} dt\, j_n(t) = \int_0^{t_c} dt\, p_{n,1}(t)\omega_n(R(t))\,,\ n \geq i+1\,. \tag{3.40}$$

This quantity equals the fraction of covered islands at time t_c for which the stable nucleus originates from a state possessing exactly n adatoms. Figure 3.15 shows J_n as a function of n for fixed $\Gamma = 10^8$ and various α. We see that for all α states with $n \gg 4$ dominate the onset of the nucleation. The number of particles n_{peak} in the state where J_n has a maximum strongly increases with increasing α. For $\alpha = 10^{-3}$, the second layer nucleation is typically initiated by $n_{\text{peak}} \simeq 18$ adatoms on top of the island.

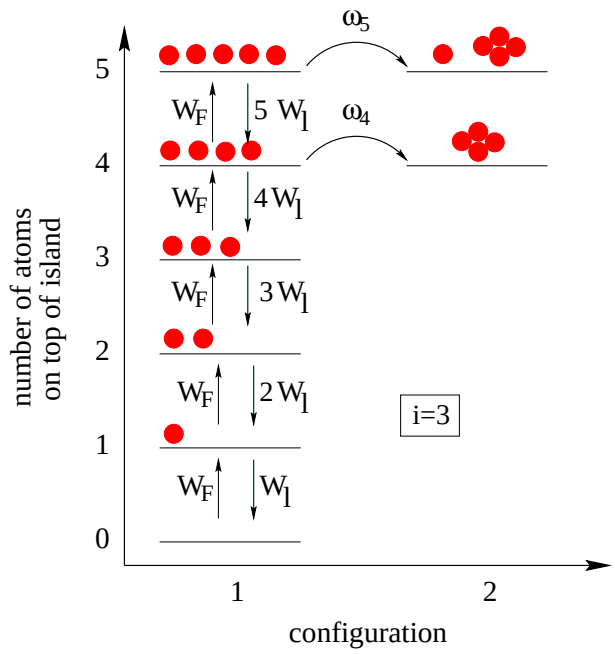

Figure 3.13: States and corresponding transition rates (see eqs. (3.32)–(3.35),(3.17)) involved in the second layer nucleation for a critical nucleus of size $i = 3$ when the lifetimes of unstable clusters are neglected. Only states corresponding to $n \leq 5$ atoms on top of the island are shown.

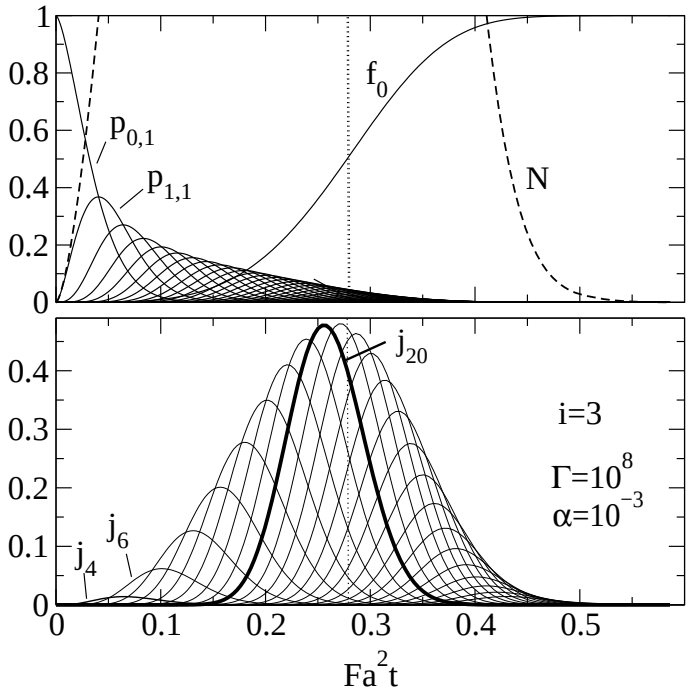

Figure 3.14: Time development of the fraction of covered islands $f(t)$, the mean number of atoms $N(t)$ in states containing no stable nucleus, the occupation probabilities $p_{n,1}$, and the currents $j_n(t) = \omega_n p_{n,1}$, $n \geq i+1$ for $i=3$, $\alpha = 10^{-3}$ and $\Gamma = 10^8$. The maximum number of atoms included in a diagram of the type shown in fig. 3.13 is $n_\star = 50$. The vertical dotted line marks the coverage $Fa^2 t_c$ at the critical time t_c. At t_c we find $N(t_c) \cong 10$.

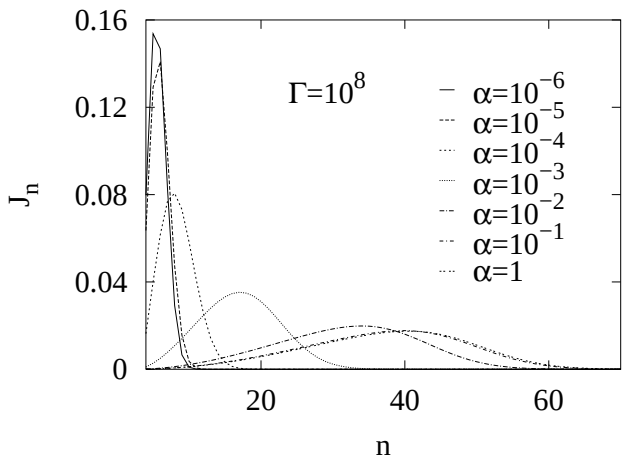

Figure 3.15: Integrated nucleation currents up to time t_c as a function of the number of particles n in the state from which the nucleation event took place ($i=3$).

3.6 Second layer nucleation with interactions

Interactions between atoms can have several origins and depend on the distance between adatoms. The strongest contribution of electronic interactions is localized and can be characterized by chemical bonds. Because the binding energy depends on the substrate electron density, additional indirect interactions are induced by polarization and screening effects around adatoms. These interactions are usually small and in the form of Friedel oscillations with a dependence on distance r as $\propto \cos(2k_{\mathrm{F}}r)/r^2$. Here k_{F} is the Fermi wavevector of the electronic surface band. For certain systems indirect electronic interactions can be much stronger[FS00] and become comparable to the diffusion barrier in magnitude. Other types of interactions are magnetic interactions in the presence of magnetic moments and the electrostatic dipole-dipole interaction, as well as elastic interactions through deformation of substrate, which are non-oscillatory with a decay of $1/r^3$.

We consider two consequences of these interactions: *(i)* a dissociation energy $E_{\mathrm{dis}} \gtrsim k_{\mathrm{B}}T$ that is required for the detachment of an adatom or the break up of clusters into two pieces in the next section *(ii)* additional barriers mediated by substrate electrons that impede the approach of two atoms by diffusion in sec. 3.6.2.

3.6.1 Metastable clusters

Scaling theory

diesen Abschnitt besser weglassen ??
To demonstrate how the presence of metastable nuclei may be included into the general procedure presented in sec. 3.4, we consider, as in [KPM00], the simplest case where a dimer is metastable with characteristic dissociation time τ_{dis} and trimers are stable ($i=2$). For $i=2$ we have to deal with the fluctuation-dominated situation. We note in passing that this can be true even for larger i when metastable clusters can form, since their presence tends to drive second layer nucleation into the fluctuation-dominated situation.

In contrast to the discussion leading to eq. (3.25) for the non-interacting particle model, the formation of the stable trimer is not necessarily the rate limiting process. It is possible that the dissociation time τ_{dis} becomes so large that the nucleation happens effectively instantaneously once the dimer has formed. To decide whether the formation of the stable trimer or metastable dimer is rate limiting, we have to compare $p_1(R)p^{(2)}_{\mathrm{enc}}(R)$ with $p_2(R)p^{(3)}_{\mathrm{enc}}(R)$, where $p^{(\mathrm{j})}_{\mathrm{enc}}(R)$ denotes the encounter probability of j atoms (in sec. 3.4.1 no superscript (j) was

introduced, since only $j=i+1$ had to be considered). Hence we write

$$\Omega_{\text{fl}}(R)=\begin{cases} \pi F R^2 p_2(R) p_{\text{enc}}^{(3)}(R)\,, & p_1 p_{\text{enc}}^{(2)} \gg p_2 p_{\text{enc}}^{(3)} \\ \pi F R^2 p_1(R) p_{\text{enc}}^{(2)}(R)\,, & p_1 p_{\text{enc}}^{(2)} \ll p_2 p_{\text{enc}}^{(3)} \end{cases} \tag{3.41}$$

To calculate the occupation probabilities $p_n(R)$, $n \leq 3$, we first need to know the modified lifetimes $\tau_n'(R)$ of states with exactly n atoms on top of the island. Clearly, $\tau_1'(R) = \tau_1(R)$ with $\tau_1(R)$ from eq. (3.18), since the metastable dimer has no influence on the lifetime of a single atom. The characteristic time $\tau_2'(R)$, however, will be enlarged in comparison to $\tau_2(R)$ from eq. (3.18) and can be estimated as follows (we disregard any prefactors): As in [KPM00] we consider the first deposited atom as immobile and the second deposited atom as diffusing (this simplifying view does not affect the scaling properties of $\tau_2'(R)$). Once the second atom has been deposited it needs a time of order $(R^2/D + \tau_{\text{dis}})$ to reach the step edge, since one encounter with the first deposited atom typically takes place during one traversal of the island within time $\tau_{\text{tr}} \equiv R^2/D$ [KPM00]. At the boundary the second atom is "reflected" a typical number $M \sim \alpha^{-1}$ of times before leaving the island. Between all reflections, the overall elapsed time is of order $(MRa/D + m\tau_{\text{dis}})$, where Ra/D is the typical time for a single atom to return to the edge and $m \sim (MRa/D)/\tau_{\text{tr}} \sim a/\alpha R$ is the typical number of times the second atom encounters the first atom [KPM00]. Summing up all time contributions we obtain (neglecting the prefactors belonging to the four individual terms)

$$\tau_2'(R) \sim (\tau_{\text{tr}} + \tau_{\text{dis}}) + \frac{a}{\alpha R}(\tau_{\text{tr}} + \tau_{\text{dis}})\,. \tag{3.42}$$

Note that for $\tau_{\text{dis}} \ll \tau_{\text{tr}} = R^2/D$, $\tau_2'(R)$ reduces to $\tau_2(R)$ from eq. (3.18) (without prefactors). To estimate $\tau_3'(R)$ we note that if the dimer state is the prevalent one, $\tau_3'(R) \sim \tau_1(R)$, whereas, if all three atoms are likely to be separated, $\tau_3'(R) \sim \tau_3(R)$. Since $\tau_3(R) \sim \tau_1(R)$, we find $\tau_3'(R) \sim \tau_1(R)$ in either case. In the strong barrier limit $\alpha \ll a/R$, in particular, the first two terms on the right hand side of eq. (3.42) can be neglected, and, since $\tau_1 \sim Ra/D\alpha \sim \tau_{\text{tr}} a/\alpha R$, we can simply write $\tau_2' \sim \tau_1(1 + \tau_{\text{dis}}/\tau_{\text{tr}})$ which agrees with the result derived in [KPM00]. This finding for strong step edge barriers implies that for $\tau_{\text{dis}}/\tau_{\text{tr}} \gg 1$ the two atoms are effectively always in the dimer state and $\tau_2' \sim \tau_2 \tau_{\text{dis}}/\tau_{\text{tr}}$, while for $\tau_{\text{dis}}/\tau_{\text{tr}} \ll 1$ they are effectively always separated and $\tau_2' \sim \tau_2$.

When inserting the modified lifetimes into eq. (3.19) and neglecting states with $n > i+1 = 3$ ($p_n \simeq 0$ for $n > 3$ until onset of nucleation in the fluctuation-dominated situation), we can calculate the occupation probabilities $p_n(t)$. In the quasi-stationary limit ($dp_n/dt = 0$ but $R = R(t)$), in particular, we obtain (for $0 \leq n \leq i+1 = 3$)

$$p_n = \frac{\prod_{j=1}^{n} q_j}{\sum_{j=0}^{i+1} \prod_{k=1}^{j} q_k}\,, \quad q_j \equiv \pi F R^2 \tau_j'\,. \tag{3.43}$$

To calculate the encounter probabilities $p^{(n)}_{\text{enc}}(R) = 1 - \exp[-\omega'_n(R)\tau'_n(R)]$, $n = 2, 3$, we furthermore need to know the modified encounter rates $\omega'_n(R)$. From eq. (A.7) in Appendix A.1 we find $\omega'_2 = w_1$ (eq. (A.7) for $i = 1$) and $\omega'_3 \simeq w_1 w_2 / v'_2$ (eq. (A.7) for $i = 2$), where $w_1 \sim w_2 \sim \tau_{\text{tr}}^{-1}$ from eq. (A.1) and $v'_2 = \tau_{\text{dis}}^{-1}$ (modification of eq. A.3), i.e. $\omega'_2 \sim 1/\tau_{\text{tr}}$ and $\omega'_3 \sim \tau_{\text{dis}}/\tau_{\text{tr}}^2$.

To discuss eq. (3.41) we may now distinguish various cases depending on whether we have to consider *(i)* the non-stationary or quasi-stationary situation, *(ii)* the strong ($\alpha \ll a/R$) or weak barrier ($\alpha \gg a/R$) limit, *(iii)* the formation of the metastable dimer or stable trimer as rate limiting, *(iv)* the encounter processes to be faster or slower than the escape process ($\omega'_n \tau'_n \ll 1$ or not for $n = 2, 3$), and *(v)* τ'_2 to be dominated by the metastable dimer state ($\tau'_2 \sim \tau_{\text{dis}}$ in the weak barrier limit and $\tau'_2 \sim \tau_1 \tau_{\text{dis}}/\tau_{\text{tr}}$ in the strong barrier limit) or to be dominated by the state of separated atoms ($\tau'_2 \sim \tau_2$). Rather than treating all these possible cases (and analyzing their possible occurrence for the generic growth law (2.7) by employing self-consistency requirements) we only remark that the results obtained by Krug *et al.*[KPM00] are entailed in our description. In this work, certain regimes corresponding to the quasi-stationary case in the strong barrier limit are considered for both $q_1 \sim q_3 \ll 1$ and $q_1 q_2 \ll 1$, where we obtain $p_1 \simeq q_1$ and $p_2 \simeq q_1 q_2$ from eq. (3.43). Since $\omega'_1 \tau'_1 = \tau_1/\tau_{\text{tr}} \sim a/\alpha R \gg 1$ in the strong barrier limit, we can always set $p^{(2)}_{\text{enc}} \simeq 1$ in eq. (3.41). The following regimes are then discussed in [KPM00] with increasing τ_{dis}:

(i) For $\tau_{\text{dis}} \ll \tau_{\text{tr}}^2/\tau_1$ we have $p^{(3)}_{\text{enc}} \simeq \omega'_3 \tau'_3 \sim \tau_{\text{dis}} \tau_1/\tau_{\text{tr}}^2$ and $\tau'_2 \sim \tau_1$, i.e. $p_2 \simeq q_1^2$ and $p_1 \gg p_2 p^{(3)}_{\text{enc}}$. Accordingly, we obtain $\Omega_{\text{fl}} \sim (\pi F R^2 \tau_1)^3 \tau_{\text{dis}}/\tau_{\text{tr}}^2$ corresponding to eq. (14) (regime I) in [KPM00].

(ii) For $\tau_{\text{tr}}^2/\tau_1 \ll \tau_{\text{dis}} \ll \tau_{\text{tr}}$, we find $p^{(3)}_{\text{enc}} \simeq 1$ and $\tau'_2 \sim \tau_1$, i.e. $p_2 \simeq q_1^2$ and $p_1 \gg p_2 p^{(3)}_{\text{enc}}$ as in *(i)*, and hence $\Omega_{\text{fl}} \sim (\pi F R^2)^3 \tau_1^2$ corresponding to eq. (15) (regime II) in [KPM00]. In the following cases, where τ_{dis} becomes even larger (and τ_1, τ_{tr} do not change), we still have $p^{(3)}_{\text{enc}} \simeq 1$.

(iii) For $\tau_{\text{tr}} \ll \tau_{\text{dis}} \ll \tau_{\text{tr}}/\pi F R^2 \tau_1$, $\tau'_2 \sim \tau_1 \tau_{\text{dis}}/\tau_{\text{tr}}$, i.e. $p_2 \sim q_1 q_2 \sim (\pi F R^2)^2 \tau_1^2 \tau_{\text{dis}}/\tau_{\text{tr}}$. The condition $\tau_{\text{dis}} \ll \tau_{\text{tr}}/\pi F R^2 \tau_1$ is equivalent to $p_1 \gg p_2 p^{(3)}_{\text{enc}} \simeq p_2$, and we thus find $\Omega_{\text{fl}} \simeq \pi F R^2 p_2 \simeq (\pi F R^2)^3 \tau_1^2 \tau_{\text{dis}}/\tau_{\text{tr}}$ corresponding to eq. (16) (regime III) in [KPM00].

(iv) For $\tau_{\text{tr}}/\pi F R^2 \tau_1 \ll \tau_{\text{dis}}$ finally, $p_1 \gg p_2$ and the formation of the stable trimer is no longer the rate limiting process. From eq. (3.41) we then obtain $\Omega_{\text{fl}} \simeq \pi F R^2 p_1 \sim (\pi F R^2)^2 \tau_1$ corresponding to eq. (17) (regime IV) in [KPM00]. As expected, the scaling behavior of Ω_{fl} in this limit reduces to the case $i = 1$ (see also the discussion in sec. 3.6.1).

It is clear that the above analysis is difficult to extend to even more complicated situations. Moreover, due to the growing number of characteristic time scales, we found it increasingly difficult to discern pronounced scaling regimes in practice, see e.g. fig. 3.16. We therefore prefer to treat the problem of second

layer nucleation in the presence of metastable clusters within the more general framework outlined in the sec. 3.5.1.

Rate equation approach

The general procedure outlined in sec. 3.5.1 allows us also to describe situations, where the binding energies of unstable clusters of size $j \leq i$ are not small compared to $k_{\mathrm{B}}T$. To demonstrate this we again consider the case $i = 2$ and the corresponding diagram in fig. 3.10. The dimer in the intermediate states possessing no stable nucleus is now considered to be metastable, and we introduce the parameter

$$\beta \equiv \exp(-\Delta E_j^{\mathrm{dis}}/k_{\mathrm{B}}T) \tag{3.44}$$

as "dissociation probability" (analogous to the step edge crossing probability $\alpha = \exp(-\Delta E_{\mathrm{S}}/k_{\mathrm{B}}T)$). For $\beta = 1$ we recover the non-interacting particle model. From the outset it is clear that second layer nucleation will proceed faster for smaller β, since the state probabilities $p_{3,2}(t)$ and $p_{4,2}(t)$ in fig. 3.10 and hence the currents $j_3(t)$ and $j_4(t)$ defined in eq. 3.39 will become strongly enhanced.

Figure 3.16 shows R_c as a function of α for fixed $\Gamma = 10^8$ and various β obtained from Monte Carlo simulations (open symbols). As expected, the critical radius decreases with decreasing β. In fact, for $\beta = 10^{-6}$ one can regard the dimer as effectively being stable on the relevant time scale t_c, so that the changes with β correspond to a continuous transition from $i = 2$ ($\beta = 1$) to $i = 1$ ($\beta = 10^{-6}$). The comparison with the numerical solution of eqs. 3.36 (solid lines) yields very good agreement. To achieve this agreement, we used the *same* set of prefactors $\kappa_{\mathrm{a,j}}^{(n)}$, $\kappa_{\mathrm{d},2}$ as given on page 43 and used for fig. 3.12. This highlights the power of the rate equation approach to treat second layer nucleation in general situations.

3.6.2 Ring barriers

In this section we study the case where the approach of two atoms by diffusion is impeded by additional barriers (published in [HM02]). As a generic model we consider a barrier E_{ring} in form of a ring with radius ξ around each adatom. The occurrence of such barriers was explored by Fichthorn and Scheffler based on extensive density functional calculations [FS00]. Similar interaction effects can be caused by Shockley surface states [HP00]. Experimentally, an extra repulsive barrier of up to 30meV between Cu atoms on Cu(111) was found at the 9th to 11th neighbor distances[KBE+02, FMS03]. The rate equation theory allows us to account for these interaction effects in the form of additional processes and states.

As before, we label the states according to the total number n of atoms on top of the island and their configuration ν. Now the configuration label ν specifies the

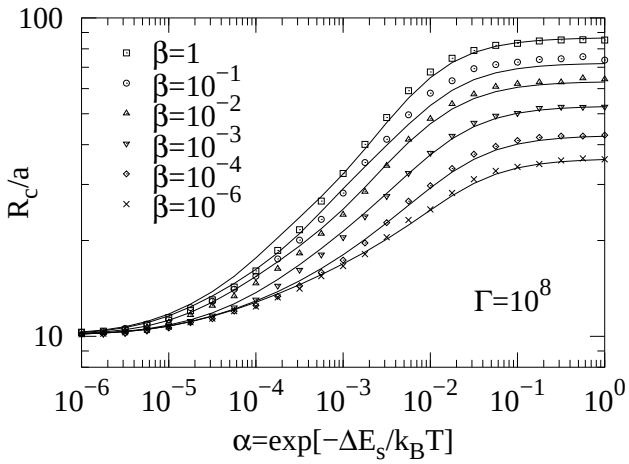

Figure 3.16: Comparison of critical island sizes R_c obtained from the rate-equation approach with results from kinetic Monte Carlo simulations of the one-island model for $i=2$. Dimers are metastable and dissociate with a rate $\beta D/a^2$ (see eq. (3.44)).

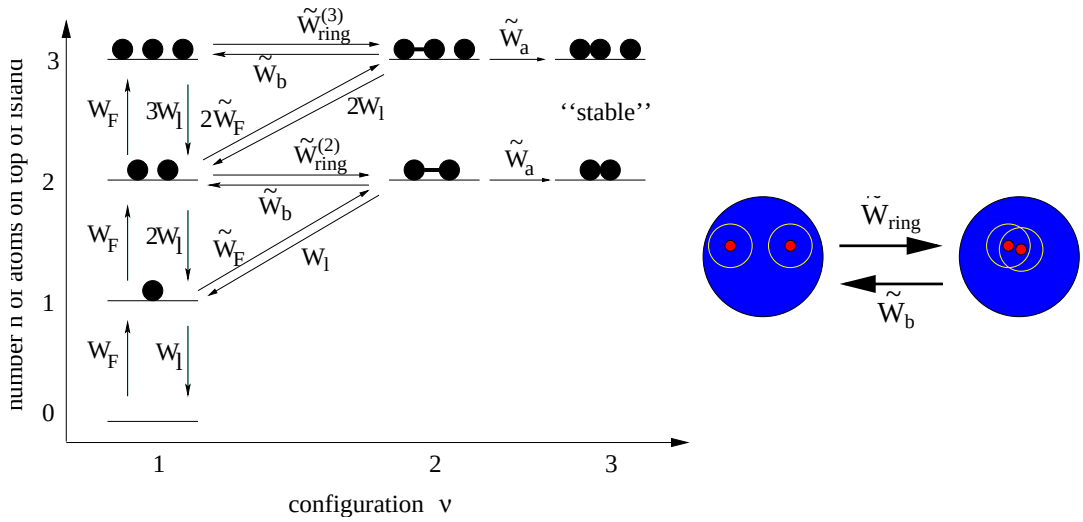

Figure 3.17: States and the corresponding transition rates involved in the second layer nucleation with ring barrier interaction and a critical nucleus of size $i = 1$. The adatoms in configuration 2 are inside each others‘ ring barrier, which is marked by the connecting line. The two states with configuration label $\nu = 3$ contain a stable dimer.

way the n atoms are decomposed into clusters and which pairs of atoms have a distance smaller than ξ and are thus “weakly bound” by their ring barriers. In fig. 3.17 the most important states are shown together with the rates $W(n, \nu \to n', \nu')$ connecting them. Inclusion of further states in the analysis does not change our results by more than a few percent except for very large ratios $\Delta E_{\rm s}/k_{\rm B}T$ and $D/Fa^4 \lesssim 10^5$.

In addition to the rates W_F and W_l for deposition and loss of atoms on the island, the additional rates $\tilde{W}^{(n)}_{\text{ring}}$, $\tilde{W}_F$, $\tilde{W}_b$ and $\tilde{W}_a$ (cf. fig. 3.17) involve the ring barrier in form of the associated Boltzmann factor $\alpha_{\text{ring}} = \exp[-\Delta E_{\text{ring}}/k_{\text{B}}T]$, $\Delta E_{\text{ring}} = E_{\text{ring}} - E_{\text{D}}$, and the ring radius ξ. $\tilde{W}_F = \pi F \xi^2$ is the deposition ("flux") rate into a ring. $\tilde{W}_a = \tilde{\kappa}_a 2D/(\pi\xi^2)$ is the attachment rate for two atoms in a circle which are confined to a separation distance smaller than ξ. It results from the time $\propto \xi^2/2D$ for the two atoms to encounter by diffusion on top of an island with radius ξ. For the relevant case $a < \xi \ll R$ we can further derive the rates for formation and breakup of pairs weakly bound by their ring barriers. The breakup rate is given by

$$\tilde{W}_b = \tilde{\kappa}_b \frac{D\alpha_{\text{ring}}}{a\xi}. \tag{3.45}$$

It results from the probability $\propto 2\pi\xi/\pi\xi^2$ for two atoms to have distance ξ times the rate $\propto \alpha_{\text{ring}} D/a^2$ to overcome the ring barrier. The rate for formation of an adatom pair weakly bound by their ring barriers is

$$\tilde{W}^{(n)}_{\text{ring}} = \frac{n(n-1)D}{R^2}\left(\tilde{\kappa}_1 \frac{a}{\xi\alpha_{\text{ring}}} + \tilde{\kappa}_2\right)^{-1}, \tag{3.46}$$

if in total n adatoms are on top of the island. The associated time $(\tilde{W}^{(2)}_{\text{ring}})^{-1}$ for two atoms results from two contributions: The time $\propto R^2/D$ for first reaching the interaction distance $\xi \ll R$ and the time for overcoming the barrier. The latter is given by $[(2\pi\xi a/\pi R^2) \times (\alpha_{\text{ring}} D/a^2)]^{-1}$, where the term $2\pi\xi a/\pi R^2$ is due to the probability for a pair to have a distance in the interval $(\xi, \xi + a)$ and the term $\alpha_{\text{ring}} D/a^2$ is the rate to overcome the ring barrier. The rate $\tilde{W}^{(2)}_{\text{ring}}$ for a single pair has to be multiplied by the number $n(n-1)/2$ of distinct pairs to obtain the total rate for n adatoms.

Atoms bound via the ring barrier will have a reduced mobility compared to the individual atoms. We therefore approximate the total loss rate for such pairs with the one of a single atom W_l.

The validity of all formulae for the elementary rates is tested as before against kinetic Monte-Carlo (KMC) simulations performed on a hexagonal lattice for the (111) surface. The additional rates not yet tested are shown as scaling plots in fig. 3.18, demonstrating the good agreement of the KMC data with the predictions for $\tilde{W}_b$ and $\tilde{W}^{(n)}_{\text{ring}}$. All constants $\tilde{\kappa}$ in eqs. (3.45),(3.46) are of the order of one. The results for breakup and formation of ring barriers from the KMC simulations were renormalized so that in the limit of weak barriers the nucleation rate without ring barriers is approximately reproduced. The values are: $\tilde{\kappa}_1 = .34$, $\tilde{\kappa}_2 = 1$, $\tilde{\kappa}_{\text{b}} = 0.5$ and $\tilde{\kappa}_{\text{a}} = 1$.

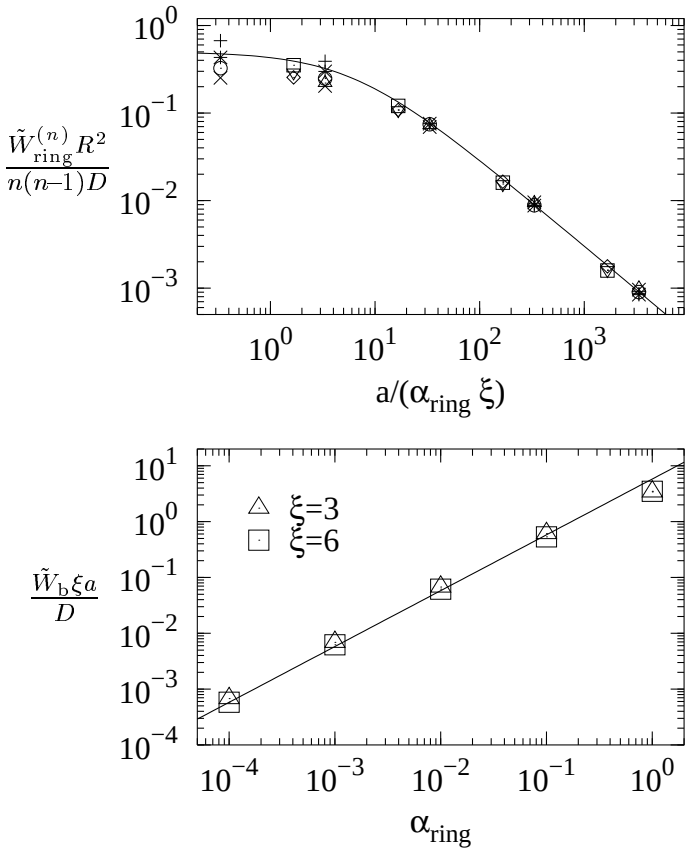

Figure 3.18: Scaling plots of the rates for formation and breakup of atom pairs bound by their ring barriers. The symbols in the upper part of the figure refer *(i)* to $n = 2$, $\xi/a = 3$ for $R/a = 10$ (+), 22 (∗), 46 (∘), 100 (×), *(ii)* to $n = 2$, $\xi/a = 6$ for $R/a = 46$ (□), 100 (◊), and *(iii)* to $n = 3$, $R/a = 6$ for $\xi/a = 3$ (△) and 6 (▽). The solid line in the upper part is a fit to $f_{\rm m}(x) = (\tilde{\kappa}_1 x + \tilde{\kappa}_2)^{-1}$ [cf. eq. (3.46)] and the solid line in the lower part has slope one [cf. eq. (3.45)].

3.6.3 Implications for Experiments

As an application we quantify possible errors when determining the step edge barrier $E_{\rm s}$ [EH66, Sch69] in second layer nucleation experiments under the assumption of non-interacting adatoms. In these experiments one measures the probability $f[R(t)]$ that a stable cluster has nucleated on top of the island until time t (i.e. the fraction of "covered islands"). In systems with a substrate mediated ring barrier, second layer nucleation will be aggravated and nucleation sets in later. A repulsive ring barrier therefore has an effect similar to a reduced step edge barrier, and thus yields an apparent measurement value $\Delta E_{\rm s}^{(0)}$ smaller than the "true" $\Delta E_{\rm s}$. On the other hand, metastable dimers facilitate the formation of a stable nucleus, leading to values $\Delta E_{\rm s}^{(0)}$ larger than $\Delta E_{\rm s}$. For the Ag/Pt(111) system we compare the results for determining the step edge barrier at different

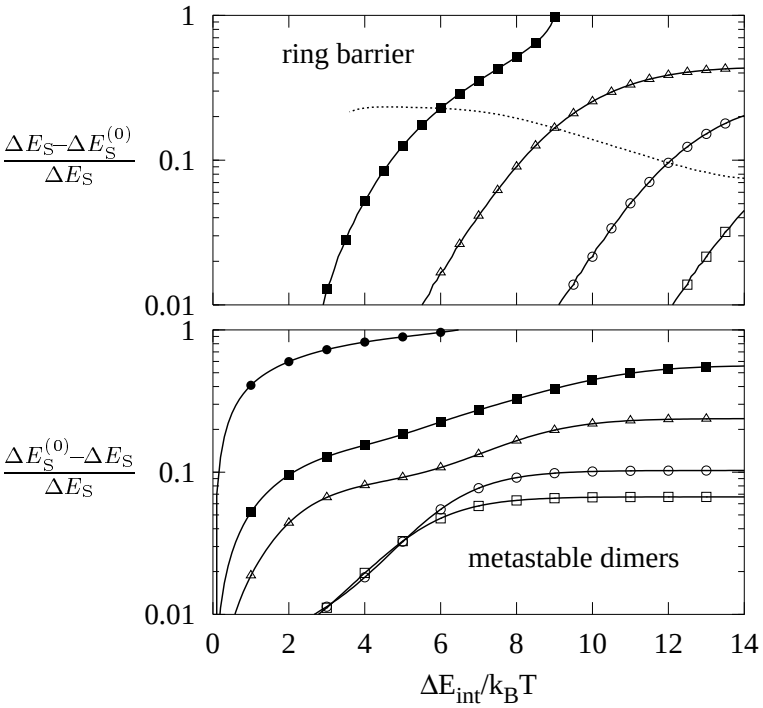

Figure 3.19: Relative error of the apparent additional step edge barrier $\Delta E_S^{(0)}$ when neglecting interactions ($\Delta E_{int} = 0$) with respect to the "true" barrier ΔE_S calculated for $\Delta E_{int} > 0$; upper part: $\Delta E_{int} = \Delta E_{ring}$, lower part: $\Delta E_{int} = \Delta E_{dis}$. The symbols refer to different values $\Delta E_S/k_BT = 3$ (•), 6 (■), 9 (△), 12 (○), and 15 (□). The dotted line in the upper figure is drawn for $\Delta E_S = \Delta E_{ring}$. All plots are calculated with $D/Fa^4 = 10^9$ and the generic growth law $R(t) \propto \sqrt{t}$.

levels of sophistication of the underlying theory.

To estimate the significance of the interactions, we first present results for the relative error $[\Delta E_S - \Delta E_S^{(0)}]/\Delta E_S$ as a function of the interaction parameters. By solving Eq. (3.36) we obtain the curves $f[R(t); \Delta E_S]$ that refer to processes including interactions. On the other hand, we can solve the rate equations neglecting the interaction ($\Delta E_{ring} = 0$), thus obtaining $f_0[R(t); \Delta E_S^{(0)}]$. By fitting the curves f_0 to the "true " curves f we obtain the apparent $\Delta E_S^{(0)}$. For the growth law we use the generic form $R(t) \propto \sqrt{t}$ (with the prefactor $(D/Fa^4)^{i/2(i+2)}\sqrt{Fa^2}$ from standard nucleation theory as in sec. 2.3). In heteroepitaxy the D in this growth law has to be distinguished from the one on top of an island. In the upper half of fig. 3.19 we show results for the relative error as a function of ΔE_{ring}. In the lower half of the figure we include the results of an analogous analysis for $i = 2$ with metastable dimers. We see that for small ΔE_S, even weak interactions ΔE_{int} lead to a large relative error. Closer inspection shows, that for fixed ratio $\Delta E_{int}/\Delta E_S$, the relative error decreases with increasing interaction energy (cf. the dashed line in fig. 3.19). In the case of metastable dimers, the error reaches a plateau when

the dissociation energy becomes so large that a dimer is stable on the time scale of the formation of a stable trimer. This signifies the transition to the $i=1$ case.

3.6.4 Case study: Ag/Pt(111)

For Ag/Pt(111) detailed second layer nucleation measurements of the type discussed above were performed by Bromann *et al.* [BBRK95]. The system Ag/Pt(111) is particularly suited as a reference, since it has the advantage that many of the relevant parameters were determined both by experiment [BBR+95, BBRK95, BHM+96, BBJ+99] and by first-principle calculations [Fei94, RSS97, RS98, FS00]. Experimentally, the diffusion barrier E_{D} for Ag adatom diffusion on a strained Ag monolayer grown on Pt(111) is $E_{\mathrm{D}} \cong 60$ meV [BBR+95]. It has been shown by density functional calculations [FS00] that Ag adatoms diffusing on one monolayer Ag on Pt(111) [1ML Ag/Pt(111)] exhibit a strong additional ring barrier $\Delta E_{\mathrm{ring}} = E_{\mathrm{ring}} - E_{\mathrm{D}} \cong 50$ meV at a distance $\xi/a \cong 2.1$ as introduced in sec. 3.6.2. We expect the same barrier for diffusion on top of already existing Ag islands with sufficient size on the platinum surface.

The original analysis by Bromann *et al.* was based on the "TDT approach" for second layer nucleation (see sec. 3.3). For the experimental parameters, regime II of the fluctuation dominated case applies and the TDT approach should not be applied. In contrast to the generic growth law $R(t) \propto \sqrt{t}$ used for fig. 3.19, in the experiment of Bromann *et al.*, clusters grow predominantly by deposition on top rather than attachment from the sides. This leads to an exponential growth law $R(t)$, different from the generic growth law eq. (2.7) for the mean island radius used so far. The modification of the theories presented to this exponential or more general growth laws is straightforward. Neither the general expressions (3.23),(3.25) for the second layer nucleation rates in simple situations nor the master equation (3.36) depend on the specific form of the growth law (the expressions for $\bar{n}$, p_n, etc. in the quasi-stationary case, however, get modified, see the discussion in sec. 3.4.1).

Metastable states are not considered here, because $i = 1$ in the temperature range of the experiment. In fig. 3.20 we have fitted the measured fraction of covered islands $f(R)$ yielding $\Delta E_{\mathrm{S}}^{(0)} = 65$ meV, which is about twice the value obtained previously based on the TDT approach (see Table I). For the much less reliable prefactor ratio [RT00] we find $\nu_{\mathrm{S}}/\nu_{\mathrm{t}} = 41$. The rate equation theory without interactions yields essentially the same value $\Delta E_{\mathrm{S}}^{(0)} = 68$ meV thereby supporting the scaling approach [RM99, HRM00].

The next step in theoretical sophistication is the inclusion of the ring barrier. When using the value $\Delta E_{\mathrm{ring}} = 50$ meV [FS00], we find a significantly decreased value of $\Delta E_{\mathrm{S}} = 52$ meV. This decrease seems to be in contradiction to the reasoning above that $\Delta E_{\mathrm{S}}^{(0)} < \Delta E_{\mathrm{S}}$. However, the values were obtained by fitting both

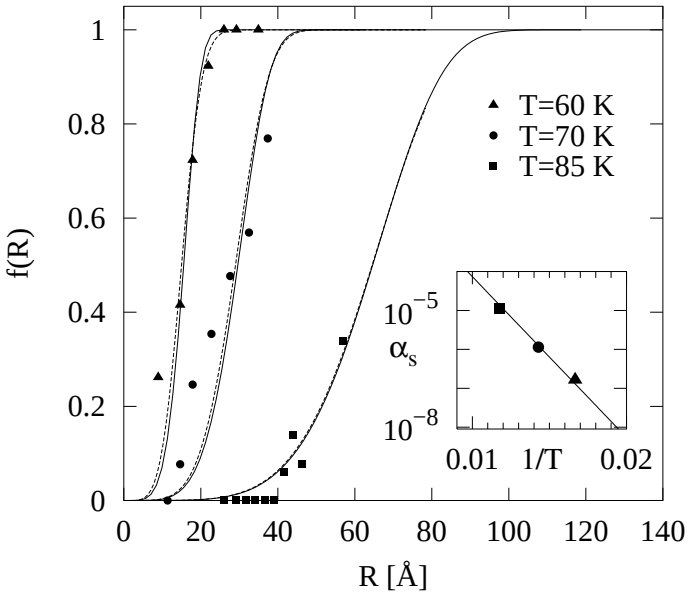

Figure 3.20: Fraction of covered Ag islands of size R as measured by Bromann *et al.* [BBRK95]. The solid lines refer to fits with the scaling approach when neglecting interactions and the dashed lines refer to fits with the rate equation theory when including the ring barriers. The inset shows the Arrhenius fit for values α_s obtained by the rate equation theory for $\nu_s = \nu_t = 10^{12}$ Hz.

the prefactor ν_s/ν_t and ΔE_s to the data and cannot be directly compared because the prefactors turn out to be very different (see table I). When fitting under the constraint $\nu_s/\nu_t = 1$ [KPM00], the value for ΔE_s increases from 42 meV to 48 meV in accordance with the general argument. Interestingly, the behavior of the standard error (see table I) indicates that the system is better described when including the interactions. However, this interpretation should not be driven too far, since the standard error is only an indication of the quality of the fit, but should not be interpreted as the measurement error.

It was recently argued that the often reported small prefactors for hopping on weakly corrugated surfaces are due to neglecting the interaction effects in the analysis of first layer nucleation experiments [OBWL01]. We therefore also analyze the data using the theoretical prediction $\nu_t = 10^{12}$ Hz [RS98] in the rate equation approach. The three α_s values obtained for each temperature shown in fig. 3.20 lie very closely on a line in an Arrhenius plot (see the inset in fig. 3.20). Both when using ν_s/ν_t as fitting parameter and when setting $\nu_s/\nu_t = 1$, we find comparatively large values $\Delta E_s = 74$ meV and $\Delta E_s = 82$ meV, respectively.

In conclusion, when measuring ΔE_s by nucleation experiments, interactions have to be properly taken into account.

ν_t [Hz]	ΔE_{ring} [meV]	Theory	ΔE_S [meV]	ν_S/ν_t	ΔE_S [meV] ($\nu_S/\nu_t = 1$)
10^9	0	TDT	30 ± 5	1	30
10^9	0	Scaling	65 ± 5	41	43 ± 2.2
10^9	0	Rate Eq.	68 ± 1	83	42 ± 2.6
10^9	50	Rate Eq.	52 ± 1	2	48 ± 0.4
10^{12}	50	Rate Eq.	74 ± 2	0.3	82 ± 0.8

Table 3.3: Comparison of results for the additional step edge barrier for Ag/1ML Ag/Pt(111) obtained with theories of different levels of sophistication (see text). The standard errors from the fitting procedure are shown for the values of ΔE_S.

3.7 Applications

The theoretical understanding of second layer nucleation is not only of basic importance but has numerous applications. One of these is the determination of the effective step edge barrier ΔE_S for systems, where the more direct and simpler method via the measurement of adatom lifetimes by field ion microscopy[KE98, Kel94] cannot be applied. Most methods for determination of the step edge barrier essentially determine the quantity $(\nu'/\nu)\exp(-\Delta E_S/k_B T)$, so that separating ν'/ν from the Boltzmann factor requires analyzing data for different temperatures. The breakdown of the TDT approach in the fluctuation-dominated situation calls for a reexamination of some experimental data for estimating ΔE_S, also in cases which are not further complicated by additional interactions as in sec. 3.6.4.

Such a case is the Ag/Ag(111) system also studied by Bromann*et al.*[BBRK95]. A re-examination of the data has been carried out by Krug *et al.*[KPM00] with a fluctuation based theory equivalent to the one presented here. The original value for the step edge barrier was reported as $\Delta E_S \approx 120$meV[BBRK95]. By using both ν'/ν and ΔE_S as free fitting parameters, one obtains $\Delta E_S \cong 320$meV and $\nu'/\nu \cong 4 \times 10^8$. These values are much larger than the previous ones and are in disagreement with effective medium calculations [LdP94], as well as with results from evaluating other experimental data [MVvdV+95, SH95, RBT97]. However, in all these evaluations a particular fixed value for ν'/ν is *assumed*. This assumption implies that one has to allow for a temperature dependence of ΔE_S. Such a dependence is conceivable when remembering that ΔE_S is an effective barrier, which results from an averaging over microscopic rates. Setting $\nu'/\nu = 1$, Krug *et al.* obtained $\Delta E_S(T = 120\text{K}) \cong 110$meV and $\Delta E_S(T = 130\text{K}) \cong 100$meV [KPM00]. These values compare more favorably with the alternative ways of determination referred to above.

TODO eigene Daten einfuegen

Tringides *et al.* claimed to have measured ν'/ν with great accuracy[RT00] by

using RHEED measurements. However, we argued[HM01], that based on the existing data for Ag/Ag(111) a definite value for ΔE_{S} (and thus ν'/ν) cannot be given. One may only conclude that $\nu'/\nu \gg 1$ for $\Delta E_{\mathrm{S}} \geq 120$meV. In order to obtain better results for ΔE_{S} and ν'/ν, one could perform RHEED measurements at different temperatures.

Krug *et al.* moreover studied the influence of step decoration by CO molecules [KCM98] on R_c (and hence ΔE_{S}) for Pt/Pt(111). They found a strong increase of ΔE_{S} with CO partial pressures, when analyzing the data corresponding to regime II (for $i=1$) of the fluctuation-dominated situation. Hence contamination by CO is expected to favor multilayer growth.

On the other hand, surfactants may promote smooth layer-by-layer growth. For example, the presence of only small amounts of Sb for growth of Ag on Ag(111) were shown to convert rough multilayer to layer-by-layer growth[vdVvPL+92, VVM+94]. It was suggested[vdVvPL+92] that Sb reduces ΔE_{S}, but, since it was observed that Sb increases the island density in the first layer[vdVvPL+92, TvdGT94], it is also possible that the induced layer-by-layer growth results from a decrease of the mean island distance[ZL94, LZCM93]. Even in the absence of surfactants, a change of the *effective* step edge barrier may go along with a shape transition of the islands with varying temperature (see [KPVC90, BMC92, vSWV93, TvdGT94] and the footnote on page 17), and this can induce changes in the film morphology as well. With respect to the transition from the fluctuation-dominated to the mean-field type situation with varying i predicted in this work, it would also be interesting to conduct proper experiments for metal epitaxy on (100) surfaces, where a change from $i=1$ to $i=3$ is often observed with increasing temperature.

The case of heteroepitaxy can be treated as well by replacing the jump rate D/a^2 of adatoms on top of the islands by a modified jump rate D'/a^2 in all formulae.

A further application pertaining to the design of self-organized nanostructures is the possibility to create pyramidal mounds on a substrate, which are called "wedding cakes"[EFFL94, KSCM99, GMD+01]. As suggested by Michely *et al.*[MKKP99], the size L_{top} of the top terrace of the pyramid should be roughly given by $\Omega(L_{\mathrm{top}}) \approx F$, where Ω is the second layer nucleation rate. Recently, an expression for the distribution of L_{top} has been suggested within a self-consistent analysis of a model for the dynamics of the top terrace[KPM00]. In recent developments of nanostructure formation also larger clusters of atoms are considered as basic building blocks in epitaxial growth. The underlying processes seem to be very similar to the case of deposition of single atoms or simple molecules (for a review, see [Jen99]), so that it could well be that also for cluster deposition an effective step edge barrier has a decisive influence on the film topography.

3.8 Summary and Discussion

In summary, we have presented a detailed theoretical investigation of the nucleation on top of islands in epitaxial growth. The approach first identifies relevant states of the island in terms of the number of atoms on the island and the way these are decomposed into monomers and clusters of subcritical size. Transitions between these states are described by rates for deposition of atoms, loss of atoms over the step edge, aggregation processes and nucleation events. In the case of interactions, additional rates for breakup of metastable states and formation and breakup of pairs weakly bound by a ring barrier have to be included. All rates were derived from scaling arguments and shown to agree with kinetic MC simulations.

When the lifetimes of unstable clusters can be neglected (non-interacting particle model), it was possible to tackle the problem within a simplified stochastic description based on the deposition rate, the time needed for a monomer to leave the island and the encounter rate for the number of atoms needed to form a critical nucleus. In this case, the critical island radius shows a power law relationship with the quantities Γ and α (defined in eqs. (2.3),(3.1)) in various scaling regimes. An important result of the scaling analysis is that the nucleation for critical nuclei of size $i \leq 2$ is dominated by fluctuations, while for larger critical nuclei it can be treated in a mean-field type manner (note, however, that the metastability of clusters tends to increase the fluctuation dominated regime). The second layer nucleation rate for both the fluctuation dominated and mean-field situation was derived in compact form (see eqs. (3.25),(3.23)). Understanding the reason for the failure of the mean-field approach has attracted more attention [CP01, PC03]. One interpretation of the results is that the nucleation rate in confined geometries depends on the number of distinct sites visited, while mean-field models incorrectly count every visit of a site.

When metastable clusters can form with appreciable lifetimes, the simplified description can in principle be extended (see sec. 3.6.1), but becomes of limited value due to the fact that many elementary processes get mutually coupled both sequentially and in parallel. In such situations it is better to employ the more general framework outlined in sec. 3.5 where a master equation is set up that is based on our derivation for the transition rates between island states. In this framework, additional interactions in the form of ring barriers can be easily incorporated. The theoretical description can be viewed as a three-fold hierarchy: *(i)* A description with individual atomic positions and jump processes on the lattice, can be accurately modeled with KMC simulations and serves as a reference. *(ii)* Identification of states (equivalence classes for atomic configurations) according to the number of atoms and decomposition into clusters together with derivation of rates for transitions between such states. The greatly reduced number of states allows for a direct numerical solution of the corresponding master equation. *(iii)* Identification of scaling properties of the rates and subsequently in the

dependence of the critical island radius on Γ and α by self-consistency arguments. This approach allows the most physical insight by explicity stating the dominant pathway in each scaling regime and delineates the validity of mean-field theories.

The theories predict significantly different nucleation rates than the previous mean-field TDT approach in cases which are of relevance to experiments. Therefore, experiments which measure the step edge barrier by observing nucleation in the second layer need to be reevaluated. In the presence of interactions, additional errors are introduced if they are neglected in the evaluation of experimental data. We quantified the influence of two types of interaction effects on measurements of the step edge barrier for a range of possible parameters and reanalyzed an experiment where interactions effects by ring barriers are important.

4 Growth of binary alloys

4.1 Motivation

Understanding the epitaxial growth of binary alloys is of fundamental interest and the methods presented in this section are applicable to a wide range of materials. In our specific computations we focus on the $CoPt_3$ system, because of its potential in applications, availability of a large set of experimental data, but lack of theoretical understanding in important aspects. Magnetic properties in $CoPt_3$ are strongly influenced by the arrangement of the Co atoms. In general, the magnetic anisotropy energy (MAE) of a homogeneous material depends primarily on the orientation of the magnetization to the crystallographic axes via the crystal field anisotropy and on the orientation with respect to the sample geometry due to dipolar interactions of the magnetic moments[Chi97, DMW00].

For thin magnetic films used in storage devices, the MAE and its direction are decisive parameters that need to be controlled for developing high density magnetic storage materials. The magnitude of the anisotropy determines the stability of the magnetization direction against thermal excitation. It therefore also determines the minimum particle size needed for long term storage. A direction of the MAE with an easy axis perpendicular to the film plane is called perpendicular magnetic anisotropy (PMA). Such an anisotropy has several technical advantages for further increasing information densities by minimizing negative influence of stray fields and effectively doubling the available write fields with an additional soft magnetic layer[MTM+02]. However, for thin films, the form anisotropy that results from dipolar interactions tends to drive the magnetization into the film plane[Chi97]. Much recent activity in the field of magnetic thin films has therefore been devoted to develop materials with PMA [MTM+02].

4.2 Experiments

In order to overcome the form anisotropy of the thin film, additional contributions to MAE originating from interfaces or from the internal structure can be harnessed. In the case of $CoPt_3$, PMA could be induced in several ways: (i) Multilayers formed by epitaxial deposition of alternating Co and Pt layers[GJ93, ZGGF89] or by choosing an appropriate crystallographic direction in $L1_1$ ordered CoPt with

self-organized layering[UUH+02], (ii) Films without long range order but local structural anisotropies with preferential Co-Pt bonds perpendicular to the film plane by codeposition of Co and Pt with $CoPt_3$ stoichiometry[WBG+92, RSTH95, SRT+99]. (iii) Nanoclusters obtained by codeposition in $CoPt_3$ stoichiometry on a van der Waals surface that promotes 3D growth.

Bulk crystals of $CoPt_3$ have fcc lattice structure. Below the temperature $T_{\mathrm{o/d}} =$ 958 K they become ordered with the $L1_2$ structure, where the Pt atoms are at the face centers and the Co atoms at the corners of the fcc unit cell. Films of type (ii) were grown on Pt(111) and Ru(0001) surfaces at growth temperatures T_{g} up to a thickness of 30-300 nm. They only show PMA in a temperature window $500\ K < T_{\mathrm{g}} < 820\ K$. The lower temperature reflects kinetic limitations for development of the local anisotropies while the upper bound is due to the occurrence of isotropic long-range $L1_2$ ordering. Only within that temperature window a uniaxial structural order develops with magnetic properties that can overcome the shape anisotropy.

For nanoclusters (iii), the temperature window where PMA occurs is shifted to room temperature with significant advantages for technological applications. The origin of PMA in films (ii) could be attributed to preferential Co-Pt bonds out of plane by XAFS[TCFJ96], EXAFS[CNH+01] and MCXD[NKS+98] experiments. The strong surface segregation of Pt is believed to play a dominant role in structure formation for both types of films. The situation for nanoclusters is more complicated, because surface effects can play a dominant role.

The reason for three-dimensional island formation of $CoPt_3$ by deposition on WSe_2(0001) surfaces is the combination of the weak van der Waals interaction with the large lattice mismatch of 17% between $CoPt_3$(111) and WSe_2(0001) (nearest neighbor distance 0.272nm in the (111) planes compared to Se-Se nearest distance 0.328nm in the (0001) planes). The islands have the usual $CoPt_3$ lattice constant as confirmed by RHEED measurements[AMT+01], so that magnetostriction effects can be ruled out as the source for the observed magnetic behavior. At a nominal coverage of 0.8 monolayer the islands have an average diameter 2.9nm and height 0.9nm at a growth temperature $T_{\mathrm{g}} = 293$K (20°C), and an average diameter 4.4nm and height 1.2nm at a growth temperature $T_{\mathrm{g}} = 573$K (300°C)[AMT+01]. This corresponds to 300 and 1200 atoms per nanocluster at 20°C and 300°C, respectively. Each nanocluster is hexagonal in shape with a top (111) facet and wall facets consisting of {100} and {111} planes. The $L1_2$ order forms above growth temperatures $T_{\mathrm{g}} > 423$K (150°C) and vanishes above 973K (700°C). The remarkable lowering of the onset temperature for $L1_2$ ordering compared to the smooth films is attributed to the increase of possible chemical arrangements associated with the free surfaces of the nanoclusters.

Similar growth-induced PMA as in CoPt alloys is also observed for Ni_xPt_{1-x} films[VSMH01]. However, for a related class of materials (garnets), the magnetic anisotropy can depend on the crystallographic orientation of the growth

facet[HH74].

In the case of $CoPt_3$ the anisotropy arises from hybridization of d-electron states and spin-orbit coupling. Experiments with multilayers show that the hybridization is highly localized at the interface[NKS+98]. The importance of the interfaces for the origin of the MAE is further corroborated by the fact that electronic structure calculations for Co/Pt superlattices yield the largest values for anisotropy energies for alternating layers of Pt and Co with 1 ML thickness[LV95], and the observed reduction in MAE from the perfect superlattice case for discontinuous monolayers, e.g. due to interdiffusion. Therefore, consideration of only nearest neighbors is sufficient to describe the anisotropy arising from CoPt bonds.

In this work we show how the combined effects of kinetically limited surface segregation and shape formation lead to a structural anisotropy that induces PMA in binary nanoclusters. The effect of cluster shape discussed here primarily relies on surface contributions and favors PMA, in contrast to the dipolar form anisotropy. To demonstrate these mechanisms, we analyzed a model for binary alloys based on nearest neighbor interactions.

4.3 Simulation Model

To our knowledge, prior kinetic MC simulations modeling the growth of binary alloys were either not fully 3-dimensional and employed e.g. simplified solid on solid models[SLP98] and other simplifying assumptions regarding the rates of processes. The work that comes closest to what is presented here is a simulation with only one component and unphysical large distance diffusion hops to speed up the simulation[HGdlR98].

4.3.1 Chemical interactions

Our model starts from an fcc lattice where a site can be occupied with an atom of type A (Co) or B (Pt), or by a vacancy V. In contrast to vacancy driven diffusion models with a small concentration of vacancies and fixed shape of the sample, here most of the simulation box consists of vacancies representing the free space in the vicinity of the cluster and allows for an unconstrained evolution of the sample morphology. The interactions between A and B atoms are assumed to be of nearest neighbor type with a bond counting scheme in order to reduce the number of parameters. This type of lattice model is widely used for simulation of binary alloys and already captures their essential statistical properties, as e.g. in [Vak04, FVCP97, KDM03]. The algorithm automatically entails step edge barriers, desorption from the surface and the possibility of vacancy diffusion in the bulk.

The bond energies between the different atomic species are denoted by E_{AA}, E_{AB} and E_{BB}. This implies a binding energy for an atom at site i

$$E_b = \sum_{\delta=1}^{12} [E_{AA} n_i^A n_{i,\delta}^A + E_{AB}(n_i^A n_{i,\delta}^B + n_i^B n_{i,\delta}^A) + E_{BB} n_i^B n_{i,\delta}^B], \tag{4.1}$$

where $n_i^\alpha \in (0,1)$ are occupation numbers and $n_{i,\delta}^\alpha$ are the occupation numbers of the site neighboring site i in direction δ. For the case of a bulk system without vacancies, this model can be mapped onto an Ising model with interaction J and external field h:

$$J = \frac{1}{4}(E_{AA} + E_{BB} - 2E_{AB}); \qquad h = E_{AA} - E_{BB}. \tag{4.2}$$

The third parameter that determines the energies in addition to Eq. 4.2 is an average bond energy, which we chose to be the one of the $L1_2$ ordered state $E_0 = \frac{1}{2}(E_{AB} + E_{BB})$. The three parameters J, h and E_0 uniquely determine the three bond energies E_{AA}, E_{AB} and E_{BB}.

The choice of parameters should reproduce equilibrium properties of the $CoPt_3$ system: (i) A phase transition leading to chemical order ($L1_2$) at $T_{\mathrm{o/d}} = 961$ K which is related to J via $k_{\mathrm{B}} T_{\mathrm{o/d}} = 1.83J$[FVCP97] and is used to set the energy scale to units of k_{B} (961/1.83)K = 45 meV, so that $J = 1$, and $T = 1$ corresponds to 525 K. (ii) Surface segregation with nearly 100% Pt at the surface[GBSB+92] caused by the larger size of Pt compared to Co. The observed segregation is compatible with values $h/J \lesssim -4$; we chose $h/J = -4$. At the temperatures of interest, the mobility of atoms is effectively restricted to the surface so that the typical number of relevant bonds is between 3 (for an adatom diffusing on a terrace) and up to 7 (for an atom attached to an edge). Parameters for a variety of corresponding processes were calculated for Pt with electronic density functional theory (DFT)[Fei99] and yield $E_0 \approx -5$. The differences between atomic species are accounted for by the parameters J and h. A determination of the average bond energy from the bulk cohesive energy would strongly overestimate the average strength of the bonds with $E_0 \approx -20$. The reason is that the total binding energy is in reality not given by a sum of independent bond interactions and the first few bonds give a much larger contribution than those completing full coordination in the bulk [YDA+97]. The bond energies are to be understood as effective energies since the measured interactions extend to several neighbor shells[KPPB+00]. For $E_0 = -5$, $J = 1$ and $h = -4$, the bond energies are $E_{\mathrm{AA}} = E_{\mathrm{AB}} - 7$ and $E_{\mathrm{BB}} = -3$.

The experiments for nanoclusters were performed on the $WSe_2(0001)$ surface which is known to be of van der Waals type. The interaction at the surface is modeled by a weak attractive potential, represented by an additional energy of $E_{vdW} = -5$ for atoms in the first layer. Compared to a Pt(111) surface with three bonds of typical strength E_0, this amounts to about 1/3 of the energy of

a single Pt–Pt bond. The hcp sites on the (111) surface are not considered, since it is known that single Pt atoms on Pt(111) prefer fcc sites by an energy of 180 meV[FF96], Co atoms on Pt(111) by 100 meV[WLF91], and the resulting structures at experimental temperatures are of fcc type.

4.3.2 Kinetic parameters

The additional parameters needed to describe the kinetics of the system are the additional energy of the transition state E_t and the attempt frequency ν. These values are known from diffusion experiments[BHM+96] of Pt on Pt(111) surfaces as $\nu = 5 \times 10^{12} s^{-1}$ and $\Delta E_t \simeq 5$.[1] ΔE_t is identical to the diffusion barrier E_D in the previous chapter on second layer nucleation. We use a new symbol in this chapter to highlight its more general interpretation as transition energy for a variety of processes. The resulting diffusion constant is $D/a^2 = \nu e^{-\Delta E_t/k_\mathrm{B}T}$ for moves without change in energy.

The bond counting scheme implies a typical activation energy for dimer dissociation of $E_\mathrm{t} + E_0 = 450\mathrm{meV}$, which seems very small and is in fact too small by a factor of almost two when comparing to scanning tunneling microscopy (STM) experiments and DFT calculations[FM01]. However, field ion microscopy (FIM) measurements also yield a small value of 460meV, which can be explained with an additional mechanism for dissociation which involves a concerted motion of atoms at the edge of the FIM tip and is consistent with DFT calculations of a corresponding process[FM01]. Since facets on nanoclusters have about the same dimension as an FIM tip and dimer diffusion is in reality even quicker than the alternating jumps of the two adatoms as needed in the simulation, the binding energy used, effectively captures dimer dissociation better than a strict scheme based on the dissociation process alone.

In addition, the deposition rate F is an important parameter. When a deposition event is chosen, an atom is deposited at a random position in the top layer of the simulation box and moved downwards in one of the three downward directions (randomly chosen at each step) until is has at least one neighbor or reaches the surface. The nucleation theory for the first layer where the ratio D/F enters as key quantity is reviewed in Sec. 2.3. We use $F = 21$ ML/s in most simulations, but also test for sensitivity of the results with $F = 2.1$ ML/s. The latter value is about two orders of magnitude higher than experimental deposition rates. At $T = 1$ and with $F = 21$ ML/s, $D/a^2 = 3.4 \cdot 10^{10} s^{-1}$ and $D/Fa^4 = 1.6 \cdot 10^9$.

[1] When simulating the growth of multiple clusters, one should use a lower barrier for diffusion on the weakly binding substrate. The barrier for pure Co-diffusion is known [AMT+01] as about 1/2 of the value used here, but from measurements of island densities of $CoPt_3$, a value of $\Delta E_t \simeq 5$ results again when assuming a critical cluster size $i = 1$ for an analysis with eq. (2.4)[AMT+01]. When only a single cluster grows in the simulation box, these differences are not important, since almost all atoms are bound in the cluster.

The resulting rate for a process with a final energy E_f and initial energy E_i is

$$\nu\, e^{-\Delta E_t/k_\mathrm{B}T}\ \min(1, e^{-(E_f-E_i)/k_\mathrm{B}T}) \tag{4.3}$$

This rate obeys the condition of detailed balance (see also appendix B) and the minimum operation ensures that the rate of processes is bounded for moves with a lowering of bond energy.

4.3.3 Exchange Processes

$CoPt_3$ shows almost complete Pt segregation in equilibrium[GBSB+92]. While segregation can be observed in the simulations, the process by which Pt accumulates at the surface usually requires several moves. Some of them may require intermediate steps with a significant number of broken bonds. In reality, concerted moves of atoms often open new kinetic pathways, as already discussed in sec. 3.2 for exchange processes where atoms effectively overcome a step edge barrier. Exchange processes by concerted motion of several atoms are found experimentally for Co deposition on Pt(111) over a range of temperatures: 250K[GBB+00], 400K [LSK+99] and 520K[DSBSDSL02]. The exchange processes were especially frequent at the lower edges of terraces. In another experiment Ni atoms exchanged with Pt at temperatures as low as 150K[GK01]. Computer simulations for Co on Au(001) yield a rather small exchange barrier of only 250meV. The exchange barrier for Co on Cu(001) by DFT calculations is 1.02 eV[PFS+03], which is twice the diffusion barrier for that system.

Exchange processes can also be the dominant channel for Pt diffusion on {100} and {110} Pt facets as verified by FIM experiments and DFT calculations[Kel94]. In these processes an adatom is buried in the surface layer substituting a surface atom that moves to a neighboring site of the original atom. Such exchange processes are favored over direct jumps on the surface because of higher coordination numbers in the transition state.

We therefore included exchange processes in addition to single atom moves in the simulation with an additional barrier of ΔE_x and initial and final energies taken into account as before. We imposed an additional condition for a pair of atoms to exchange: One atom is required to have a coordination in the range of $3\ldots5$ and the other one in the range of $8\ldots10$. The activation energy of exchange diffusion on Pt(100) is just 470meV[Kel94], which is almost the same as the total barrier $\Delta E_\mathrm{t} + \Delta E_\mathrm{x}$ when $\Delta E_\mathrm{x} = 5$ as used in most simulations.

4.3.4 Implementation

The simulations are performed in a box with periodic boundary conditions in lateral dimensions. The dimensions of the box (l_x, l_y, l_z) are chosen so that only

one nucleus forms in the box, with the exception of the very lowest temperatures, where the island distance becomes smaller than the box size. For the deposition rate $F = 21$ ML/s used in most simulations and temperatures $T > 0.6$ the island distance which would be observed by self-organization exceeds the box size. This could be effectively accounted for by increasing the deposition rate at the boundary of the box to match the extra flux of atoms deposited within the typical capture zone of an island. However, in order to reduce the number of parameters, we deliberately kept the deposition rate constant for all temperatures.

The simulation is performed with a rejection-less continuous-time MC algorithm that generates realizations of a master equation. Each set of occupation numbers of the lattice can be regarded as a possible state of a master equation where the rates for atomic motion connect the states. Each simulation step consists of: (i) executing a process with probability proportional to its rate. (ii) incrementing the time by an interval Δt drawn from a Poissonian distribution with $\langle \Delta t \rangle = W_{\text{total}}(s)^{-1}$ (iii) update of possible process rates in vicinity of the moving atom (see Appendix B for details).

An example of a typical cluster with $N = 2000$ atoms obtained in the KMC simulations is shown in Fig. 4.1. The simulation box consists of $l_z = 15$ layers with 40^2 lattice sites each. The top facet has (111) orientation, as expected for the (111) substrate and side facets are of {111} and {100} type. The surface shows strong Pt segregation. Similar to the experiments, the aspect ratio of lateral to height dimension of the cluster is 3:1. At the temperature $T = 1.2$, the ratio $D/Fa^4 = 8 \cdot 10^{10}$ and the simulation run used $3.3 \cdot 10^{10}$ steps. A simple MC algorithm which generates equivalent dynamics, but is not rejection free, can be estimated to require close to $N^2 \cdot D/(a^4 l_x l_y F)$ steps, i.e. about 7000 times more than the algorithm used here. This ratio increases further at lower temperatures, since processes where bonds are broken will have a lower rate and correspondingly contribute to larger time increments Δt.

4.4 Connection between structural order and magnetic properties

A connection between a local structural anisotropy and the resulting magnetic anisotropy was proposed already by Néel[Née54] based on dipolar interactions depending on the type of atoms involved in a bond. The approach counts the number of bonds between neighboring atoms taking their direction and species into account. We propose to extend this scheme to the case where the local anisotropy is due to spin-orbit interactions. The anisotropies originating from the different species can be described by local bonds, as shown by the experiments discussed in sec. 4.2. The isotropic part of the magnetic interactions does not

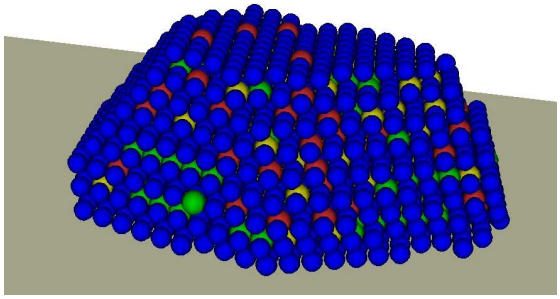

Figure 4.1: A typical cluster configuration with 2000 atoms for $h = -4$, $T = 1.2$ and $\Delta E_{\mathrm{x}} = 0$. Pt atoms are marked in blue and Co atoms are marked in different colors depending on the number of nearest neighbor Pt atoms: if more (less) Pt atoms are found OOP than IP the atom is marked in green (yellow); otherwise it is marked in red. Facets with sixfold {111} and fourfold {100} symmetry can be clearly distinguished.

need to be further specified, but may be described by a Heisenberg hamiltonian, or other models that better take into account the itinerant nature of d-electrons. The anisotropic part of the energy can then be written as

$$H_A = -\sum_{<i,\delta>} \sum_{\alpha} \Delta A^{\mathrm{Co}\,\alpha}\, n_i^{\mathrm{Co}}\, n_{i,\delta}^{\alpha} \cos^2 \sphericalangle(\boldsymbol{\mu}_i^{\mathrm{Co}}, \mathbf{a}_\delta). \tag{4.4}$$

Here $\mathbf{a}_\delta$, $\delta = 1, \ldots, 12$, denote the nearest neighbor bond vectors in the fcc lattice, $n_i^\alpha, n_{i,\delta}^\alpha \in \{0, 1\}$ are occupation numbers for species $\alpha \in (\mathrm{Co}, \mathrm{Pt}, \mathrm{V(vacancy)})$ on lattice sites $\mathbf{R}_i$, $\mathbf{R}_i + \mathbf{a}_\delta$. $\boldsymbol{\mu}_i^{\mathrm{Co}}$ are the Co moments and $\Delta A^{\mathrm{Co}\,\alpha}$ is the anisotropy energy of a single Co-α bond, equal to the energy difference between the local moment oriented perpendicular and parallel to the bond direction. The sum $\sum_{<i,\delta>}$ runs over all nearest neighbor bonds.

The anisotropy energy per atom in a nanocluster is then obtained by evaluation of H_A with saturated magnetization for a given structure $\{n_i^\alpha\}$ on a fcc lattice in different directions. The in plane (IP) direction lies in the (111) plane and the out-of-plane (OOP) direction is perpendicular to the plane (parallel to the [111] direction). The evaluation yields the bond anisotropy energy $E_{\mathrm{s}} = [H_{\mathrm{A}}(\{\boldsymbol{\mu}_i \ \ \mathrm{IP}\}) - H_{\mathrm{A}}(\{\boldsymbol{\mu}_i \ \ \mathrm{OOP}\})]$. For the evaluation, it is helpful to note that all in plane directions are equivalent because $\sum_{k=0}^{2} \cos^2(\phi + \frac{2\pi k}{3}) = \frac{3}{2}$ for an arbitrary angle ϕ. Summation over the 12 nearest neighbor vectors and using the condition $\sum_\alpha n_i^\alpha = 1$ then yields

$$\begin{aligned} E_{\mathrm{s}} = \frac{1}{2} \big[& (\Delta A^{\mathrm{CoPt}} - \Delta A^{\mathrm{CoV}})(n_\perp^{\mathrm{CoPt}} - n_\parallel^{\mathrm{CoPt}}) \\ & + (\Delta A^{\mathrm{CoCo}} - \Delta a^{\mathrm{CoV}})(n_\perp^{\mathrm{CoCo}} - n_\parallel^{\mathrm{CoCo}}) \big] \end{aligned} \tag{4.5}$$

with $n_{\perp}^{\mathrm{Co}\,\alpha}$ denoting the number of Co-α bonds with non-vanishing component in the [111] direction and $n_{\parallel}^{\mathrm{Co}\,\alpha}$ the number of bonds in plane. The latter can be written as $n_{\parallel}^{\mathrm{Co}\,\alpha} = \sum_{i,\delta_{\parallel}} n_i^{\mathrm{Co}}\, n_{i,\delta}^{\alpha}$, and $n_{\perp}^{\mathrm{Co}\,\alpha}$ is defined accordingly.

We define structural anisotropy parameters

$$P_{\perp-\parallel}^{\mathrm{Co}\,\alpha} = \frac{1}{N}\left(n_{\perp}^{\mathrm{Co}\,\alpha} - n_{\parallel}^{\mathrm{Co}\,\alpha}\right) \tag{4.6}$$

Similar to multilayers where Co-Pt bonds are oriented perpendicular to the surface, PMA can be expected for $P_{\perp-\parallel}^{\mathrm{CoPt}} > 0$.

4.4.1 Parameters for the bond anisotropy constants

The main contribution to the anisotropy comes from the Co-Pt bond anisotropy constant ΔA^{CoPt} and can be inferred from Co-Pt interface anisotropies, which were measured by magnetic torque measurements to be $K^{\mathrm{CoPt}} = 1.2$ mJ/m^2 [WWS+94], and with the magneto-optical Kerr effect on a Co wedge embedded in Pt $K^{\mathrm{CoPt}} = 1.15$ mJ/m^2 [GJ93] and multilayers $K^{\mathrm{CoPt}} = 0.96$ mJ/m^2 [WWS+94] and $K^{\mathrm{CoPt}} = 0.42$ mJ/m^2 [ZGGF89]. Differences arise through different preparations of the films resulting in differing interface roughness. Higher order terms in angles θ to the surface normal, proportional to $\sin^4\theta$ are not always accounted for separately. They can amount to about 1/4 of the $\sin^2\theta$ terms[WWS+94]. In the following, a value of $K^{\mathrm{CoPt}} = 1$ mJ/m^2 is assumed which corresponds to $\Delta A^{\mathrm{CoPt}} = 130\mu$ eV.

The anisotropy of the free Co interface was measured by comparison of magnetic anisotropy of covered and uncovered films by torsion oscillation magnetometry as $K^{\mathrm{CoV}} = -0.28$ mJ/m^2 [KG95], with MOKE measurements as $K^{\mathrm{CoV}} = -0.17$ mJ/m^2 [BBC+94] and with Brillouin light scattering measurements of spin wave excitations as $K^{\mathrm{CoV}} = -1.06$ mJ/m^2 [KLS+92]. A theoretical investigation of a free standing Co monolayer yields $K^{\mathrm{CoV}} = -0.32$ mJ/m^2 [WLF91]. Assuming a value of $K^{\mathrm{CoV}} = -0.25$ mJ/m^2, the bond anisotropy is $\Delta A^{\mathrm{CoV}} = -33\mu$ eV.

The remaining parameter in eq. (4.5) is Δa^{CoCo} for the Co-Co bond. The Co-Co bonds only have a very small anisotropy because of the small orbital Co moment and the fact that the anisotropy considered here is driven by the orbital moments. The dipolar interaction of the atomic magnetic moments is always present and is considered here for nearest neighbors. The dipolar energy of a pair of moments in parallel orientation depends on their angle to the connecting line and is $E_{\mathrm{dip}}(\alpha) = \frac{3\mu_0}{4\pi}\frac{\mu_1\mu_2}{r^3}\cos^2\alpha$. In the case of a pair of Co atoms in $CoPt_3$ with a moment of about $1.5\mu_B$[MP66, IOJ96], this amounts to a maximal energy difference at nearest neighbor distance of 18μeV. This value is smaller than the anisotropy value of Co-Pt bonds inferred from measurements of multilayers by about one order of magnitude.

Combining the contributions, we obtain $\Delta A^{\mathrm{CoPt}} - \Delta A^{\mathrm{CoV}} = 0.17\mathrm{meV}$ and $\Delta A^{\mathrm{CoCo}} - \Delta A^{\mathrm{CoV}} = 0.051\mathrm{meV}$. The second term in eq. (4.5) is much smaller than the first one because $\Delta A^{\mathrm{CoCo}} < \Delta a^{\mathrm{CoPt}}$ and $|P_{\perp-\|}^{\mathrm{CoCo}}| < |P_{\perp-\|}^{\mathrm{Co-Pt}}|$ due to the smaller number of Co-Co bonds resulting from stoichiometry and partial ordering.

The main result of this section is that knowing the magnetic anisotropy energy per bond, the structural anisotropy parameter $P_{\perp-\|}^{\mathrm{CoPt}}$ directly predicts the main bond contribution to the magnetic anisotropy constant per atom as

$$K_{\mathrm{s}} = \frac{1}{2}\Delta A^{\mathrm{CoPt}} P_{\perp-\|}^{\mathrm{CoPt}}. \tag{4.7}$$

The full uniaxial anisotropy $K_{\mathrm{u}} = K_{\mathrm{s}} + K_{\mathrm{dip}}$ also contains the form anisotropy from dipolar interactions, which is evaluated in Sec. 4.5.4.

4.5 Simulation results for nanoclusters

4.5.1 Anisotropy parameters

The two anisotropy parameters $P_{\perp-\|}^{\mathrm{Co-Pt}}$ and $P_{\perp-\|}^{\mathrm{Co-Co}}$ are shown in fig. 4.2 in dependence of temperature for clusters grown to 1000 atoms. The dashed lines connect data points with $F = 2.1$ ML/s and are shifted to lower temperatures compared to the solid lines with $F = 21$ ML/s. The slower deposition rates allow for more jumps between deposition events, so that a small decrease in temperature which slows down the kinetics can be compensated. However, F and T remain independent parameters of the system and no exact relation exists that would relate results obtained at different temperatures by simply changing F.

In the case without exchange processes, both anisotropy parameters are smaller than zero for all temperatures and PMA cannot be expected. Including exchange processes, gives rise to values $P_{\perp-\|}^{\mathrm{Co-Pt}} > 0$. In this case, a conspicuous feature of the curves is the non-monotonic dependence on temperature. Such a temperature window where PMA can be observed was also found in experiments[AMT+01, SRT+99].

At this point in the analysis, the origin of the local structural anisotropy is not clear. It could be a bulk effect similar to the ordering observed in comparatively thick films as discussed in sec. 4.2. However, the temperatures are lower and the surface to bulk ratio is very different for small clusters.

Fig. 4.3 shows $P_{\perp-\|}^{\mathrm{Co-Pt}}$ during the growth of clusters for several temperatures in the presence of exchange processes. For the two highest temperatures, the anisotropy decreases with the cluster size $\propto N^{-1/3}$. Since $P_{\perp-\|}^{\mathrm{Co-Pt}}$ is normalized

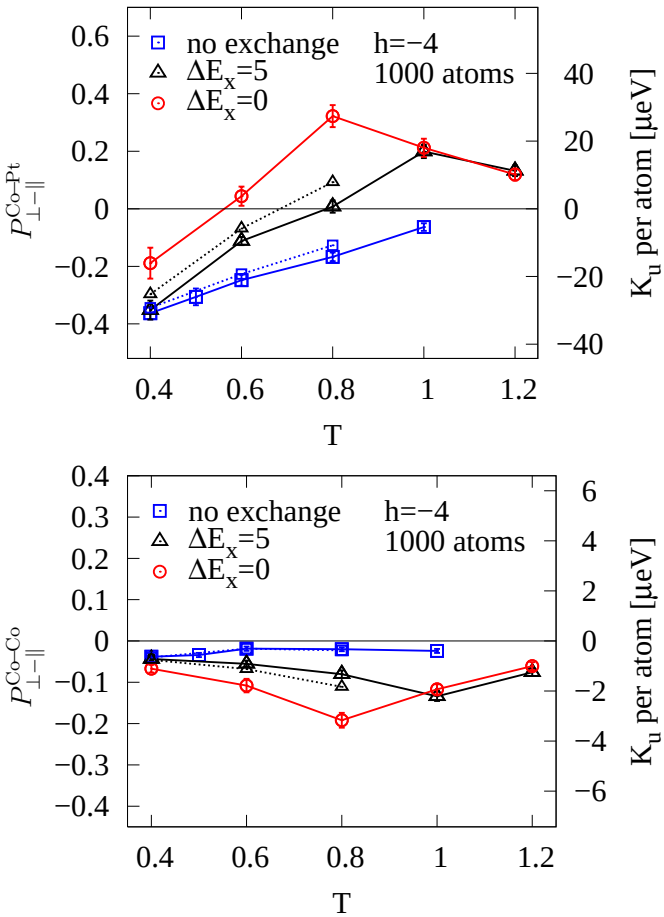

Figure 4.2: Structural anisotropy parameters $P^{\text{Co–Pt}}_{\perp-\parallel}$ (upper panel) and $P^{\text{Co–Co}}_{\perp-\parallel}$ (lower panel). The dashed lines correspond to data obtained with a deposition rate of $F = 2.1$, which is 10 times smaller than the rate used for the full lines.

per atom, the total anisotropy scales $\propto N^{2/3}$. When partitioning the sample into a bulk part and an outer shell comprised of atoms with coordination $n \leq 11$ and their neighbors, one finds that the bulk part does not contribute significantly to the total anisotropy. This indicates a surface effect as origin of the anisotropy. The surface effect is different from the thick films grown at much higher temperatures (discussed in sec. 4.2), where the bulk part shows anisotropic ordering. The next two sections investigate how cluster shape and surface segregation influence the anisotropy of nanoclusters, and explain the reason for a decrease of the anisotropy with higher temperatures.

4.5.2 Cluster shape

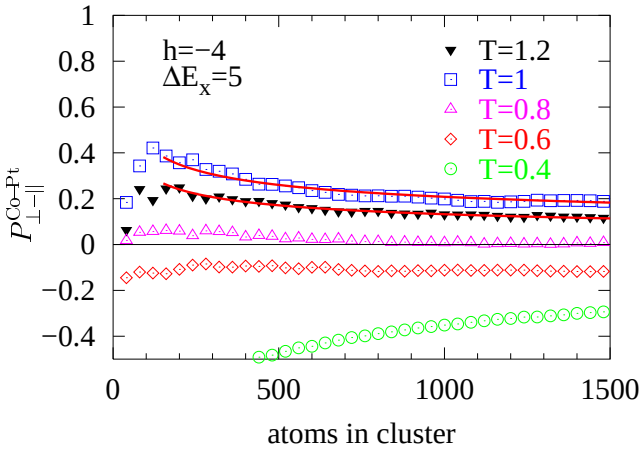

Figure 4.3: Anisotropy parameter for Co-Pt bonds averaged over 20 clusters of growing size at different temperatures. For the two highest temperatures, the scaling with cluster size N as $\propto N^{-1/3}$ is well established. The exponents of the fits for the range from 150 to 2000 atoms are -0.34 and -0.30 for $T = 1$ and $T = 1.2$, respectively.

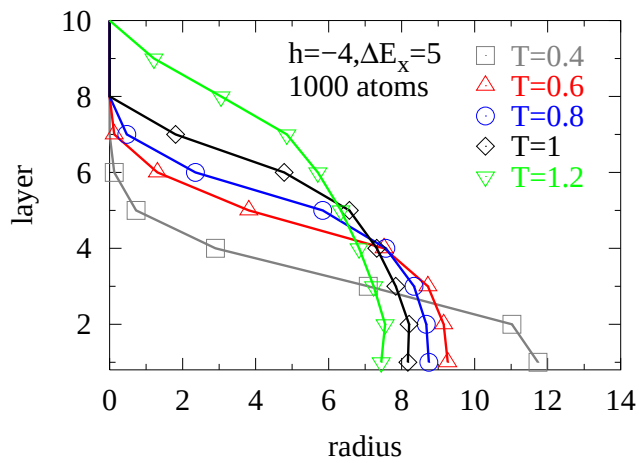

Figure 4.4: Number of atoms per layer n represented with a radius $R = \sqrt{n/\pi}$ and averaged over 20 realizations of the growth process. Layer one is the bottom layer on the (111) substrate.

In order to give a visual impression of the shape of the clusters, fig.4.4 shows an effective radius for n atoms found on average in each layer, that is defined as $R = \sqrt{n/\pi}$. In the case of the lowest temperature $T = 0.4$, several clusters grow simultaneously so that the radius cannot be interpreted as the radius of a single cluster in this case.

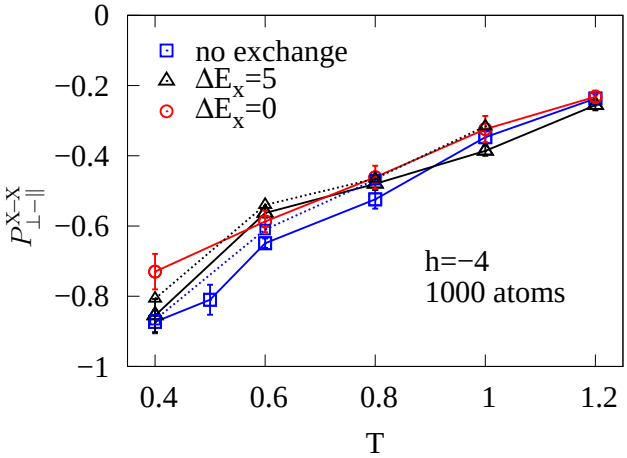

Figure 4.5: Cluster shape parameter $P^{\text{X–X}}_{\perp-\parallel}$ comparing the number of bonds OOP to the number IP. Decreasing magnitude signifies the change from oblate to ball shaped clusters.

The shape parameter $P^{\text{X–X}}_{\perp-\parallel}$ counts the number of OOP bonds minus the number of bonds IP (irrespective of the type), so that for clusters with oblate shape $P^{\text{X–X}}_{\perp-\parallel} < 0$. For homogeneous clusters (e.g. fully ordered or random occupation), the anisotropy parameters $P^{\text{Co}\,\alpha}_{\perp-\parallel}$ are proportional to $P^{\text{X–X}}_{\perp-\parallel}$. For an atom inside of the cluster with full coordination, the number of bonds IP and OOP are the same, so that only atoms at the surface of the cluster contribute to $P^{\text{X–X}}_{\perp-\parallel}$. The shape parameter therefore scales with the surface of the cluster. The dependence of $P^{\text{X–X}}_{\perp-\parallel}$ on temperature is shown in fig. 4.5.

Alternatively, the shape may be evaluated as the ratio of the radii of gyration in lateral and perpendicular directions $S_{\perp/\parallel} = \sqrt{\sum_{i,j} \mathbf{R}^2_{ij,\parallel} / \sum_{i,j} \mathbf{R}^2_{ij,\perp}}$, where $\mathbf{R}_{ij}$ is the distance vector between lattice sites i and j and indices $\perp$ and $\parallel$ specify components OOP and IP, respectively. The two shape measures correlate remarkably well to each other, provided a scaling correction is applied that connects the surface sensitive measure $P^{\text{X–X}}_{\perp-\parallel}$ with the volume dependant gyration measure as $P^{\text{X–X}}_{\perp-\parallel} \sim \left(S_{\perp/\parallel}\right)^{2/3}$.

The cluster shape plays a critical role for the formation of a bond anisotropy leading to PMA. For the oblate shapes found in simulation and experiment, a random or fully ordered configuration will have more bonds IP than OOP (irrespective of the type), so that the structural anisotropy parameter $P^{\text{CoPt}}_{\perp-\parallel} < 0$. Since this is not observed for the case with exchange, such clusters cannot be homogeneous in chemical order. The next section shows that surface segregation can effectively invert the effect of cluster shape.

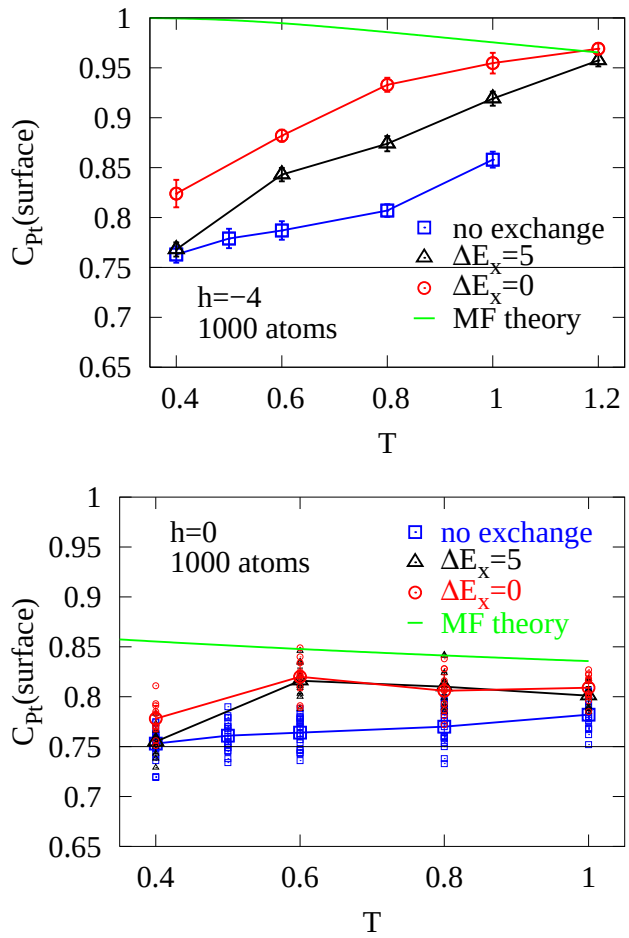

Figure 4.6: Concentration of Pt atoms in the outer shell of clusters for $h = E_{\mathrm{CoCo}} - E_{\mathrm{PtPt}} = -4$ in the upper panel and $h = 0$ in the lower panel.

4.5.3 Surface segregation

The model is set up so that Pt-segregation in equilibrium matches experimental values (see sec. 4.3.1). Segregation at a growing surface with kinetics limited by the time until the surface is covered with newly deposited atoms, will be smaller than the equilibrium values.

Strong segregation effectively turns the two topmost layers of the cluster into a structure resembling multilayers. For oblate clusters with more surface area oriented in the [111] direction than in perpendicular directions, a sufficiently strong segregation of Pt to the surface will therefore reverse the sign of $P_{\perp-\parallel}^{\mathrm{CoPt}}$, so that PMA becomes possible, even for disordered structure within the cluster. Furthermore, the weakly binding van der Waals substrate also allows for segregation

towards the substrate during growth, effectively doubling the available surface with favorable orientation.

Fig. 4.6 shows an increasing concentration of Pt atoms in the outer shell of clusters with temperature. The outer shell is defined to comprise all atoms with coordination $n \leq 11$. Since the van der Waals surface is only weakly binding, strong segregation towards the surface can be observed and "bonds" to the substrate are accordingly not counted so that all atoms in the first layer $z = 1$ are also counted as surface atoms. The inclusion of exchange processes as observed in experiments (see sec. 4.3.3) is needed to reach levels of segregation which are close to the experimentally observed values[GBSB+92].

It is remarkable that Pt-segregation can be observed even when the parameter controlling segregation $h = E_{\mathrm{PtPt}} - E_{\mathrm{CoCo}} = 0$. This can be understood from a mean field argument that counts bonds for a slab with a free surface: For a disordered structure, the exchange of a Co atom with a Pt atom of the bulk allows the system to lower its energy by $3J$. However, for a fully ordered structure, the situation is reversed and the stoichiometric composition at the surface yields the lowest energy with an energy cost for exchange of $10J$.

For nanoclusters, the almost non-existent bulk diffusion has to be taken into account and results in an increasing concentration of Co in the second layer which will impede further exchange. We calculated a mean field equilibrium model consisting of three completely filled (111) layers with the first one fixed in composition and allowing exchanges between the upper two. The third layer is the free surface. The internal energy term for a given Co concentration in the third layer $C_{Co,3}$ can be expressed in the case of 1:3 stoichiometry as

$$U = 12E_0 + \frac{3}{8}h(1 - 4C_{Co,3}) + 3J(1 - C_{Co,3} + 4C_{Co,3}^2). \tag{4.8}$$

The energy minimum at $T = 0$ is attained for $C_{Co,3} = \frac{1}{8}(1 + h/2J)$ clearly demonstrating segregation for $h = 0$.

The entropy is

$$S = \sum_{\alpha=Co,Pt} \sum_{z=2}^{3} C_{\alpha,z} \ln C_{\alpha,z} \tag{4.9}$$

Minimizing the free energy $F = U - TS$ then yields the equilibrium concentration of Co in the third layer. Including the entropy term, leads to a decrease in Pt concentration in the outer shell with increasing temperature and restores the stoichiometric concentrations in the limit of high temperatures. Such a negative slope with temperature is reproduced in the simulations for $h = 0$ when exchange processes are included, but not in the simulations for $h = -4$ and $h = 0$ without exchange processes. The positive slope of segregation values with temperature indicates that segregation differs from thermal equilibrium due to kinetic limitations.

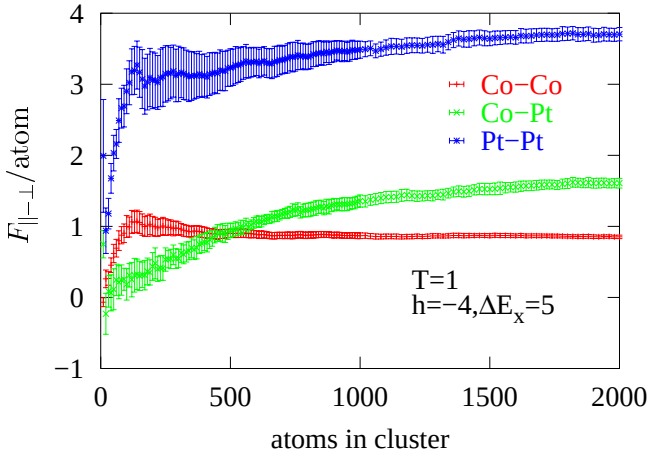

Figure 4.7: Geometry dependent part of the dipolar magnetic anisotropy during the growth process to 2000 atoms and averaged over 20 realizations. The geometry dependent terms were evaluated in length units of the nearest neighbor distance.

For the case with $h = -4$, the segregation increases with T, which leads to larger anisotropy constants $P^{\mathrm{CoPt}}_{\perp-\|}$ (see fig. 4.2), up to a maximum temperature $T_{\max}$ above which $P^{\mathrm{CoPt}}_{\perp-\|}$ falls, although the segregation continues to become stronger. The reason is that the condition of a flat cluster shape, which enables segregation to drive structural anisotropy, is not pronounced enough at higher temperatures, as shown before in fig. 4.5. The structural anisotropy is thus the result of two competing effects: the surface segregation and the transition from flat to rounded shapes.

4.5.4 Dipolar Interaction energy and total anisotropy

In order to fully evaluate the total anisotropy energy of a nanocluster, the additional contribution of the dipolar energy has to be taken into account also for atoms not on neighboring lattice sites. This term is the conventional form anisotropy and will drive the magnetization in plane, reducing the anisotropy K_{s} originating from the local structure. The dipolar form anisotropy in the limit of a thin film with saturation magnetization M_s is $\frac{1}{2}\mu_0 M_s^2$.

The dipolar energy for saturated magnetization in direction $\hat{\mathbf{M}}$ ($|\hat{\mathbf{M}}| = 1$) is

$$E_{\mathrm{dip}} = \frac{\mu_0}{4\pi} \sum_{i>j} \mu_i \mu_j \left[\frac{\hat{\mathbf{M}}^2}{|\mathbf{R}_{ij}|^3} - 3\frac{(\hat{\mathbf{M}} \cdot \mathbf{R}_{ij})^2}{|\mathbf{R}_{ij}|^5} \right], \tag{4.10}$$

where $\mathbf{R}_{ij}$ is the difference between the lattice position vectors $\mathbf{R}_i$ and $\mathbf{R}_j$. For the contribution to PMA, only the difference of this term for two directions of

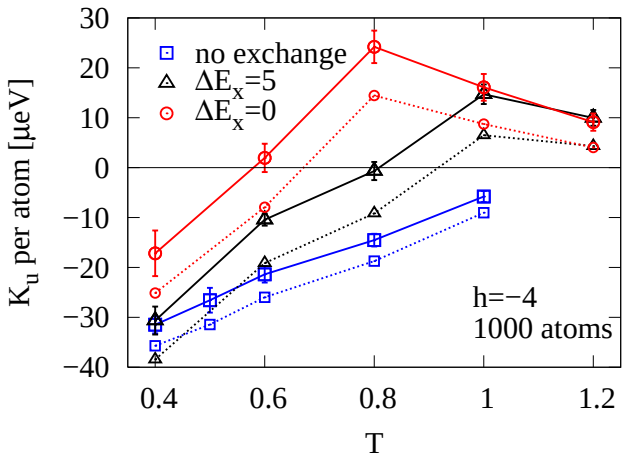

Figure 4.8: Magnetic anisotropy constant for different temperatures and different values of the additional barrier ΔE_{x} for exchange processes (no exchange processes for $\Delta E_{\mathrm{x}} = \infty$). The data of the dashed lines also includes the form anisotropy from dipolar interactions.

magnetization $\hat{\mathbf{M}} \perp (111)$ and $\hat{\mathbf{M}} \| (111)$ is needed, so that the first term cancels. The resulting energy difference $E_{\mathrm{dip}} = E_{\mathrm{dip},\perp} - E_{\mathrm{dip},\|}$ can be split into contributions for the three different types of pairs and each term can be decomposed into a geometry dependent prefactor and a second factor where the magnetic moments of the different types of atoms come into play. The total dipolar anisotropy energy can then be expressed as

$$E_{\mathrm{dip}} = \frac{3\mu_0}{4\pi} \left(F_{\perp-\|}^{\mathrm{CoCo}} |\mu_{\mathrm{Co}}|^2 + F_{\perp-\|}^{\mathrm{CoPt}} |\mu_{\mathrm{Co}}||\mu_{\mathrm{Pt}}| + F_{\perp-\|}^{\mathrm{PtPt}} |\mu_{\mathrm{Pt}}|^2 \right) . \tag{4.11}$$

The geometry dependent factors have a structure as $F_{\perp-\|} = \sum_{i>j}^{`} \frac{R_{ij,x}^2 - R_{ij,z}^2}{|\mathbf{R}_{ij}|^5}$, where $R_{ij,x}$ and $R_{ij,z}$ are a representative in-plane and the perpendicular component of $\mathbf{R}_{ij}$, respectively and the sum is restricted to one of the three types of pairs. Note that $R_{ij,x}$ is not the full in-plane component of $\mathbf{R}_{ij}$, but rather the projection onto a specific in-plane direction. The choice of in-plane direction only changes the outcome very slightly, because of the approximate threefold symmetry of the clusters. An evaluation of the geometry terms $F_{\perp-\|}$ for a typical cluster configuration, is shown in Fig. 4.7. The Pt-Pt contributions are largest, because of the larger number of Pt atoms. The factors are normalized per atom and become approximately constant above $N \approx 1000$ atoms, showing that the contribution is a volume effect. Taking the magnetic moments $\mu^{Co} = 1.5\mu_{\mathrm{B}}$ and $\mu^{Pt} = 0.3\mu_{\mathrm{B}}$ into account, it becomes clear that the Co-Co contribution is largest.

The sum $E_{\mathrm{u}} = E_{\mathrm{s}} + E_{\mathrm{dip}}$ of the bond anisotropy E_{s} from Eq. 4.5 and the dipolar terms according to Eq. 4.11 is shown in Fig. 4.8. With increasing ΔE_{x}, PMA

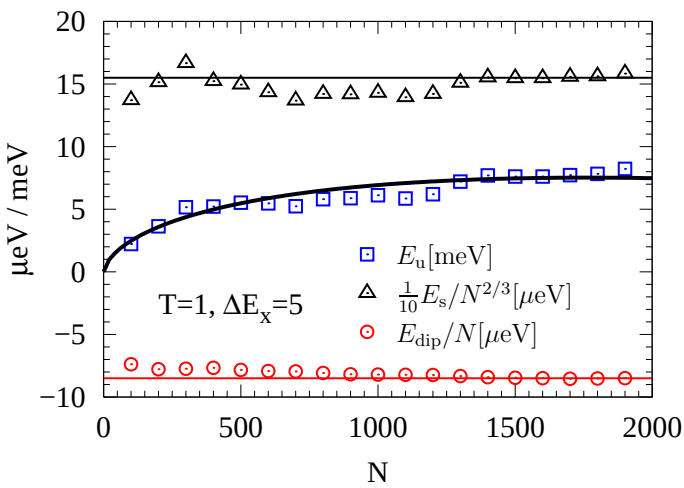

Figure 4.9: Dependence of surface E_s and bulk E_{dip} contributions to magnetic anisotropy on cluster size N and total $E_u = E_s + E_{dip}$ with best fit (solid line).

becomes weaker and the PMA window shifts to higher T. For each value of ΔE_x, there is an optimal temperature T_{opt} where PMA is strongest. The total dipolar contribution to the MAE is significant, but does not overcome the MAE induced by the Co-Pt bonds for the cluster size shown.

For a single bond between nearest neighbor atoms, the dipolar contribution has the same functional form for the directional dependence as a contribution to the anisotropy energy eq. 4.4. The measurements of the anisotropy constants $\Delta A^{Co\,\alpha}$ therefore already entail the dipolar contribution and the nearest neighbor contributions in 4.11 are removed for $Co-\alpha$ pairs.

For applications, the relevant quantity is the total anisotropy energy $E_u = E_s + E_{dip}$ of a cluster, because it determines the stability against thermal excitations reversing the magnetization. Since E_s is a surface term and E_{dip} a term proportional to the volume, the MAE can be written as

$$E_u = K_s N^{2/3} - K_{dip} N \tag{4.12}$$

with $K_{dip} > 0$. As a consequence, there should exist an optimal cluster size $N_{opt} = (2K_s/3K_{dip})^3$ (for $2K_s > 3K_{dip}$) where the MAE is largest and a critical cluster size $N_c = (3/2)^3 N_{opt}$, above which E_u becomes negative. Fig. 4.9 shows E_u as a function of N, together with the rescaled surface and bulk contributions $E_s/N^{2/3}$ and E_{dip}/N for $\Delta E_x = 5$ and $T = 1 \simeq T_{opt}$. From the plateau values for large N, we read off $K_s \simeq 155\mu$eV and $K_{dip} \simeq 8.5\mu$eV, which we use to fit E_u (solid line). The corresponding optimal cluster size $N_{opt} \simeq 1800$ is just reached in the simulations and the PMA is expected to disappear for $N > N_c \simeq 6100$.

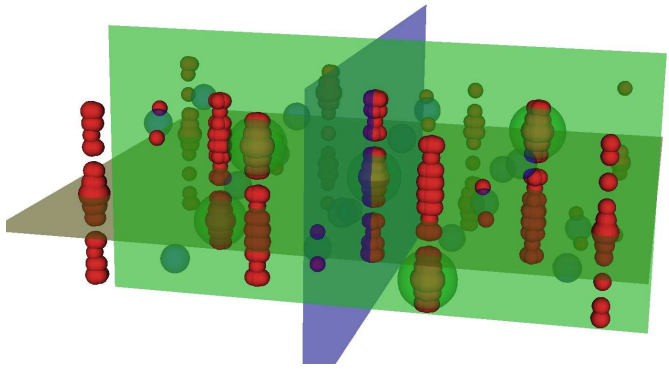

Figure 4.10: Intensity of Fourier transform of the cluster configuration in fig. 4.1. The fcc lattice in real space is transformed to a bcc lattice. The view is not restricted to the first Brillouin zone, so that the periodic structure can be seen. The large spheres mark the integration volume for evaluation of the superstructure peaks.

Slight deviations from the proportionality with N can be seen for E_{dip} even for larger clusters. This is a consequence of the growth process, which results in a cluster shape that changes with N. The reason is that kinetic parameters D/F set an inherent length scale in addition to the cluster size, and the ratio of atoms deposited on top of the cluster and arriving by diffusion from the surrounding substrate changes with growing size.

The MAE for a cluster of 1200 atoms at $T = 1$ and $\Delta E_{\mathrm{x}} = 5$ is $K_{\mathrm{u}} = 6\mu\mathrm{eV}$ per atom (see fig. 4.9). This is even larger than the experimental value of $K_{\mathrm{u}} = 3\mu\mathrm{eV}$ per atom[AMT+01] for clusters of the same size. The deposition temperature in the experiment was $300\,\mathrm{deg}\,C$, corresponding to $T = 1.1$ in the units used for the simulations. The primary difference is the much slower deposition rate in the experiments of $F = 0.02ML/s$, compared to $F = 21ML/s$ as used in the simulations. The degree of correspondence is still very satisfactory in view of the simplifying assumptions in the model that does not aim at an exact quantitative reproduction of experimental results.

4.5.5 $L1_2$ order parameter

The $L1_2$ order parameter is determined similar to the experimental situation by evaluating the magnitudes of scattered intensities around the superstructure peaks. The atoms of the cluster and the surrounding vacancies are represented by spins $s_l \in \{1, 0, -1\}$ at the lattice positions $\mathbf{R}_l$ with $s_l = 0$ for vacancies. The structure factor is then calculated via the Fast Fourier Transform and the am-

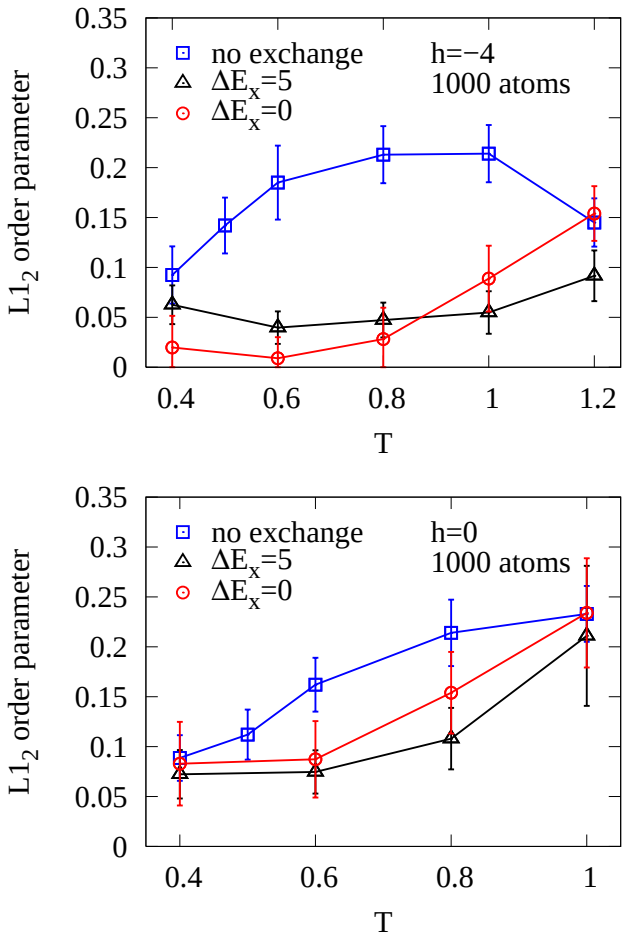

Figure 4.11: Dependence of the order parameter for $L1_2$ structure on temperature for segregation controlling parameter $h = -4$ (upper panel) and $h = 0$ (lower panel). Values are averaged over 20 realizations for $h = -4$ and 10 realizations for $h = 0$.

plitudes $F_{\mathbf{k}} = \sum_l s_l e^{-i\mathbf{k}\mathbf{R}_l}$ are squared, yielding intensities as shown in Fig. 4.10. The anisotropic box size is due to the implementation of the fcc lattice by a sparse simple cubic lattice with anisotropic lattice spacings, so that the maximal spatial frequencies depend on the direction. The shape of the cluster can be represented by a function that takes on values of one for occupied sites and zero for vacancies, so that a cluster with prescribed shape is retrieved when multiplying with a fully occupied lattice. The Fourier transform is therefore the convolution of the Fourier transforms of the shape function (cluster form factor) and the one of the underlying atomic configurations. The finite dimensions of the cluster therefore lead to a significant broadening of peaks in Fourier space. This is particularly evident in the vertical direction, where the small height of the clusters results in more spread than in lateral directions. In order to account for the smearing of peaks, an integration in k-space was performed around each peak in form of a

sphere with radius $1/10a$.

Only three non-equivalent superstructure peaks exist, corresponding to the three non-conserved order parameters in the description of $L1_2$ ordering[Sch98], which represent the ordering in directions (100), (010) and (001). The total intensity at the positions of the superstructure peaks $\mathbf{K}_1, \mathbf{K}_2\ \mathbf{K}_3$ is calculated as

$$I = \sum_{i=1}^{3} \sum_{\|\mathbf{k}-\mathbf{K}_i\|<1/10a} F_{\mathbf{k}}^2. \tag{4.13}$$

While integration of the intensity over the volume of a peak is the usual experimental procedure, the possibility to fully control the structure allows for the following evaluation of the order parameter: The intensities are calculated for surrogate structures where the shape is maintained, but the type of atoms is changed so that only one sublattice is occupied with Co atoms. Using eq. (4.13) for this structure results in the quantity $I_{\mathrm{L1_2}}$. Similarly, the case where the sites are randomly occupied with the stoichiometric concentrations yields I_{random}. The order parameter is then defined as

$$\Psi = \frac{I - I_{\mathrm{random}}}{I_{\mathrm{L1_2}} - I_{\mathrm{random}}} \tag{4.14}$$

and is automatically normalized to fall in the range zero to one.

Fig. 4.11 shows results of the order parameter Ψ in the case of a strong tendency towards segregation on the upper panel and in the case where $h = 0$ on the lower panel. Comparing the order parameters with different additional barriers ΔE_x for exchange processes, one observes that including exchange processes generally suppresses ordering. This can be understood from the large energy difference a Co adatom gains when it is incorporated by an exchange process into deeper layers of the cluster irrespective of its contribution to ordering. However, for most parameters shown, ordering for $\Delta E_x = 0$ is stronger than for $\Delta E_x = 5$, suggesting a temperature dependent value for ΔE_x that maximally suppresses ordering. The competition between ordering and segregation is presumably also the reason for the decrease of Ψ at $T = 1.2$ for $h = -4$ and $\Delta E_x = \infty$.

In the case of thick films, where PMA originates from the bulk part (see sec. 4.2), the onset of $L1_2$ ordering causes a decrease of PMA, because of the isotropic ordering (see also sec. 4.2). For nanoclusters, the onset temperature of $L1_2$ ordering in the presence of exchange processes is $T \approx 1$ and coincides with the temperatures where PMA decreases in fig. 4.11. In this case, however, PMA is a surface induced effect and its decrease is caused by the change in shape rather than concomitant bulk ordering.

4.5.6 Layer resolved analysis

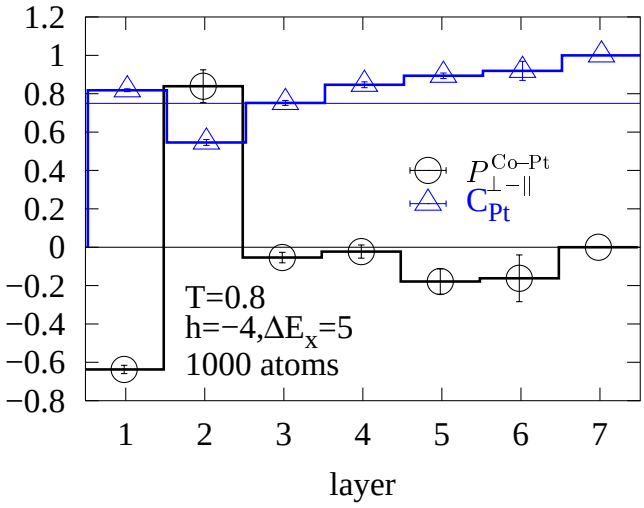

Figure 4.12: Typical layer resolved values for Co-Pt bond anisotropy and Pt concentration for the parameters as shown in the plot averaged over 20 realizations of the growth process. The enhanced Co concentration in the second layer induces a strong peak in the structural anisotropy.

When analyzing the structural anisotropy $P_{\perp-\parallel}^{CoPt}$ layer by layer, a strong enhancement in the second layer can be observed, which is caused by an increased Co concentration due to segregation effects, see Fig. 4.12. This effect is made possible by the weak binding energy of the van der Waals substrate. The strong decrease in the first layer of $P_{\perp-\parallel}^{CoPt}$ is not only due to a reduced Co concentration, but also caused by the fact that only 3 possible bonds are directed to a neighboring layer while six bonds are found in plane. The values shown for the topmost layers do not carry much weight in the total cluster average, because of the small number of atoms in these layers (cf. fig. 4.4).

The almost vanishing anisotropy in the upper layers originates from the fact that the ensemble of clusters with 1000 atoms has a distribution of cluster heights. For a sub-ensemble with a given height, the two topmost layers have opposite sign in $P_{\perp-\parallel}^{CoPt}$ in analogy to the two bottom layers. Hence their contributions cancel approximately when averaging over a specific layer using the full ensemble with varying heights.

4.5.7 Ensemble fluctuations of parameters

With clusters consisting of only a few thousand atoms, fluctuations in the properties in an ensemble of clusters with fixed N can be expected. The probability densities for the total structural anisotropy parameter of one cluster and

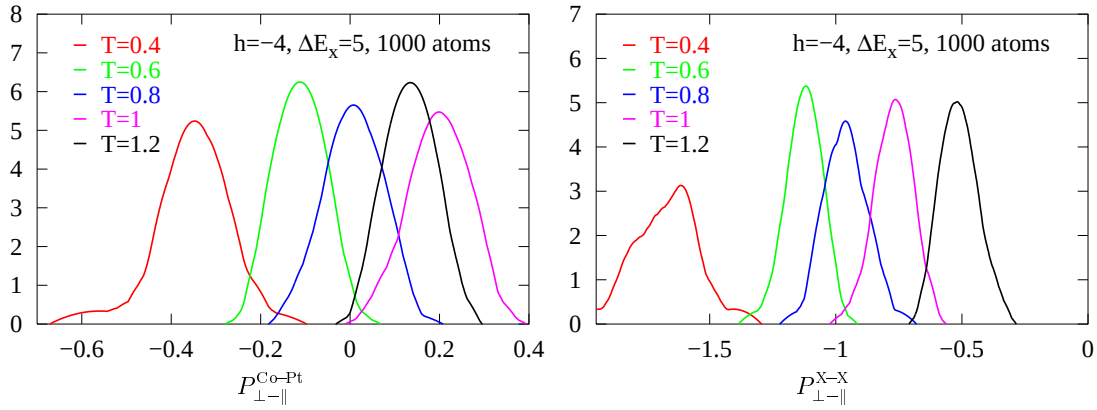

Figure 4.13: Probability density of structural anisotropy parameter $P^{\text{Co–Pt}}_{\perp-\parallel}$ (left panel) and shape parameter $P^{\text{X–X}}_{\perp-\parallel}$ (right panel) for different temperatures in the presence of exchange processes. $P^{\text{X–X}}_{\perp-\parallel} < 0$ corresponds to a larger number of IP bonds than OOP bonds.

the shape parameter are shown in Fig. 4.13. The densities are estimated with an Epanechnikov kernel (parabolic shape) using 20 samples for each temperature. At the lowest temperature of $T = 0.4$, multiple islands form in the simulation box by self-organization, so that this temperature is not directly comparable to higher temperatures where a single cluster is formed. The widths and shape of the distributions are very similar, with the exception of $T = 0.4$. The mean values of these distributions were already shown in figs. 4.2 and 4.5. With increasing temperature the shape changes from flat to rounded and the shape parameter $P^{\text{X–X}}_{\perp-\parallel}$ increases.

All error-bars shown in this chapter were calculated for a 95 % confidence interval using the Student t-distribution. The shape of the densities is roughly Gaussian, so that the calculation of confidence intervals using the t-distribution is vindicated.

4.5.8 Details of the growth process

Nucleation events

The nanoclusters are subject to second layer nucleation processes on the top terrace. The weakly binding substrate facilitates diffusion from the substrate to higher layers. An atom on the substrate surface that touches two atoms belonging to a side facet can jump onto the facet without cost in energy, because it gains one extra bond on the facet while it loses contact energy with the van der

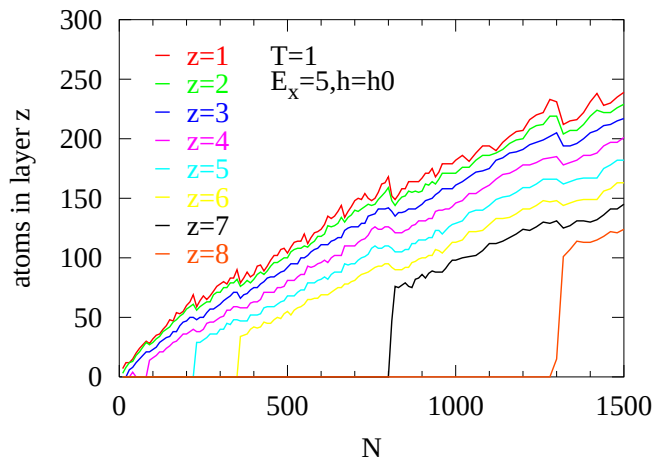

Figure 4.14: Atoms per layer versus total number of atoms during the growth of one cluster. The curve on top shows the number of atoms in the first layer above the substrate and curves below represent successive layers on top. For the 4th to 8th layer nucleation events are visible as a strong initial increase in the number of atoms.

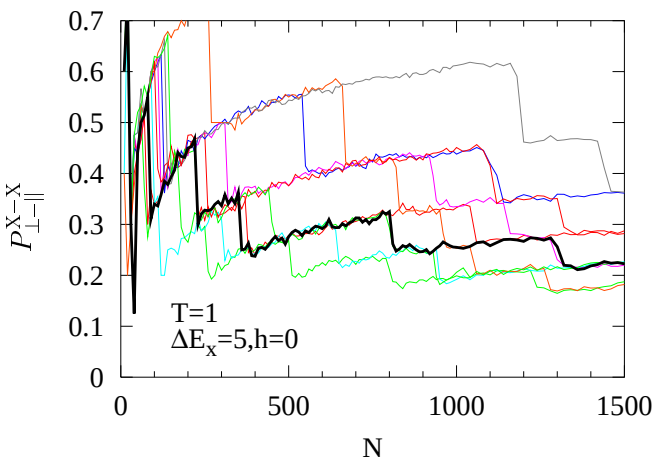

Figure 4.15: Shape anisotropy parameter $P^{\mathrm{X-X}}_{\perp-\parallel}$ representing the excess number of OOP bonds per atom for 10 different realizations of the growth process. The characteristic curves where the results from different configurations coincide, correspond to specific heights of the cluster. The thick curve corresponds to the realization shown in fig. 4.14.

Waals surface, equivalent to just one bond with the energy parameters used (see sec. 4.3.1). The 3D islands develop side facets at higher temperatures which also facilitate mass transport to higher layers compared to the situation where step edge barriers have to be surmounted as in the case of "wedding cakes" (see also sec. 3.7).

The easy mass transport across layers on facets leads to lateral growth in all layers simultaneously and nucleation events in the top layer, where atoms are visiting from the facets, may play a role depending on temperature. Nucleation events are followed by a rapid completion of the top layer as shown in Fig. 4.14. Note that the slope of the atom numbers in the top layer is initially greater than one, reflecting the effective additional mass transport from the substrate area not covered by the cluster and from the other layers. The mass transport from lower layers is also visible as a temporary decrease in the layer occupation numbers during the time when the top layer is filled.

The quickness of the nucleation events together with the small variability in shape for a given number of atoms and layers leads to noticeable patterns in the shape parameter when following an ensemble of clusters, as shown in Fig. 4.15. The growth of a cluster can be described as jumping between growth curves that are universal for a given parameter set. Each jump corresponds to a nucleation event. As the cluster sizes where nucleation occurs become smeared out with lower temperatures, the sets of growth curves become non-distinct themselves and are not visible any more at $T = 0.6$ (not shown). Knowledge of such growth curves may be of technological importance because the spread in anisotropy values of an ensemble of clusters is not monotonic during the growth process and stopping the process at the right time, could yield more homogeneous cluster properties.

Dependence of transition rates on coordination

Fig. 4.16 shows the relative frequency of hopping and exchange processes in dependence on the coordination numbers of initial and final sites. The largest number of moves are diffusion moves on terraces ($3 \rightarrow 3$) and at edges ($5 \rightarrow 5$). This highlights the importance of processes at edges and is consistent with the choice of bond parameters according to the slope of the binding energy curve as discussed in Sec. 4.3. The diagram at low temperatures is not symmetric with respect to the diagonal: the majority of processes increases rather than decreases the coordination number of the moving atom. At high temperatures, an equilibrium with respect to breaking and forming bonds is reached. Due to the comparatively weak Pt-Pt bonds, moves of Pt atoms contribute much more than one quarter to the total number of moves so that this type of equilibrium is not in contradiction with the fact that the local structure involving Co atoms and cluster shape are still far from equilibrium. While the relative number of exchange processes is much lower at the higher temperature, these processes are nevertheless sufficient to significantly enhance surface segregation, as discussed in sec. 4.5.3.

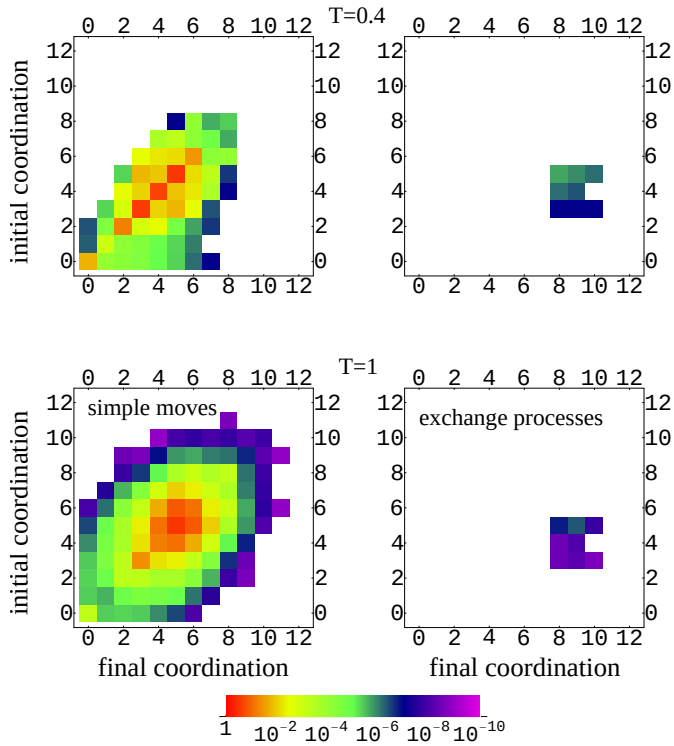

Figure 4.16: Relative frequency of hopping and exchange processes for different initial and final coordination numbers at two temperatures $T = 0.4$ (upper panel) and $T = 1$ (lower panel) with $h = -4$ and $\Delta E_{\mathrm{x}} = 5$ during the growth process to 2000 atoms.

4.6 Summary and Discussion

Motivated by experiments of $CoPt_3$ nanoclusters, we developed a kinetic model for the growth of binary alloy clusters on a weakly binding substrate by epitaxial processes. The interactions consist of nearest neighbor bonds with parameters chosen to match equilibrium properties. In the case of complex environments as encountered at step edges, additional input for effective parameters is taken from DFT calculations (see sec. 4.3). Kinetic parameters are obtained from diffusion experiments of Pt on Pt(111) surfaces and experiments observing exchange processes of the Co/Pt system.

The experiments[AMT+01] show PMA in nanoclusters for a temperature window that is bounded by frozen-in kinetics to low temperatures. The reason for the disappearance of PMA at higher temperatures was thought to be linked to the appearance of long range chemical order of $L1_2$ type[SRT+99]. In the case of nanoclusters we showed that the interplay of segregation and shape can lead to the same observations, although chemical order in the bulk is not involved. A oblate cluster with larger facets on top and towards the bottom than on the sides

will have a greater number of bonds in plane (IP) than out of plane (OOP) when counting all types of bonds. As known from multilayers, Co–Pt bonds have an easy magnetic axis along the bond direction. Hence, for the occurrence of PMA, one conversely needs more Co–Pt bonds OOP than IP. This can be achieved for oblate clusters with the help of surface segregation. In order to induce a sufficient degree of segregation, it is necessary to make the model more realistic by explicitly including exchange processes which represent concerted moves of atoms. The segregation of Pt is kinetically limited and therefore becomes stronger with increasing temperature, so that one could expect an increase of bond anisotropy with temperature. However, this is only the case for lower temperatures. At higher temperatures, the cluster shape becomes more spherical and the bond anisotropy decreases despite further increasing segregation. The consequence of these competing effects is the existence of a temperature where the bond anisotropy is strongest. The simulations therefore reproduce a temperature window for PMA, as found in the experiments of nanoclusters.

For the evaluation of PMA, the dipolar interactions of the magnetic moments have to be taken into account in addition to the local bond anisotropy. For the oblate shapes – as required for the bond anisotropy – the dipolar interactions tend to turn the easy axis of magnetization into the plane. Again, the two competing effects, bond anisotropy (surface term) and dipolar interactions (volume term), lead to an optimum cluster size where the anisotropy energy of a cluster is largest, and a second characteristic size where PMA disappears.

A second set of nanocluster experiments was performed for higher coverages. There a rotation of the easy magnetization axis into the film plane was observed with a correlated change in the aspect ratio of the clusters from oblate to tall[AMM+02]. This finding corroborates the importance of the cluster shape for the resulting magnetic anisotropy and supports the model presented in this work.

We have shown how PMA in binary alloy magnetic nanoclusters results from the combined effect of surface segregation mediated by exchange processes and oblate cluster shapes. The temperature window for PMA observed in experiments can be explained by a shape that becomes unfavorable for surface-induced PMA at higher temperatures. Stronger segregation (e.g. due to lower exchange barriers) as well as smaller adsorbate-substrate and adsorbate-vacuum surface tensions (leading to more oblate shapes) should broaden the temperature window and may guide the search for optimized materials. It should be interesting to test experimentally the predictions regarding scaling of PMA with cluster size as $\propto N^{2/3}$ for clusters with size $N < N_{\mathrm{opt}}$.

Part II

TDFT

5 Time Dependent Density Functional Theory

5.1 Introduction

Density functional theory (DFT) was first developed for the description of interacting multi-electron systems. The first key step is to prove that the particle density for the ground state implicitly entails the full information of the wave function[HK64]. The density is therefore a key variable on which the calculation of all other observables can be based. Furthermore, the theorem states that the density also uniquely determines the single particle potential. For applications, a second step [KS65] is performed that reduces the complicated many particle problem to a single particle equation where each electron moves in an effective potential which captures correlation and exchange effects induced the many body effects. In particular, the method allows the calculation of the energies of atomic configurations and intermediate transition states for processes of atoms on surfaces. The first part of the thesis referred to this type of DFT for ab-initio calculations of microscopic properties. This part deals with classical systems for which a corresponding theorem was established soon after the electronic version[Mer65]. DFT for classical systems is a powerful method to derive phase diagrams and phase transitions in condensed matter systems[L9̈4, Eva79]. The extension to lattice systems [NDM93] is particularly useful for discrete structures as encountered, e.g. in metallic alloys.

The derivation of kinetic equations based on microscopic interactions is a long-standing problem in nonequilibrium statistical mechanics. For quantum mechanical systems, the Runge-Gross theory [RG84, GDP96] is a well established tool. A similar approach for classical hamiltonian dynamics suited for hydrodynamical interactions was published only recently [CF05]. A scheme based on the Langevin equation is set up in [MT99]. Time-dependent DFT (TDFT) for lattice systems was first formulated in [RD96] and is reviewed in a broader context in [GPDM03]. In contrast to the quantum mechanical theory, the lattice models assume stochastic, overdamped dynamics. The basic assumption in TDFT is the local equilibrium approximation, which postulates that correlations at each instant in time can be described with the well developed theories for the equilibrium state. This theory therefore reproduces the thermodynamics to the accuracy of the equilibrium DFT, in contrast to mean field kinetic theories [GPDM03]. TDFT

can be applied in the kinetics of metallic alloys, adsorbate layers, and complex pattern formation on atomic scales, in particular in the presence of confinement effects (see e.g. [FRD+98]).

In the case where many ordered phases can coexist one is lead to include internal degrees of freedom into the DFT approach. As a prominent model we will consider in this work the q-state Potts model, which has a q-fold degenerate ground state [Pot52, Wu82]. The non-equilibrium dynamics of that model reflects the coarsening of domains following a quench from the disordered homogeneous phase to a system with long–range order seen in binary alloys, liquid crystals, magnetic bubbles, Langmuir films and soap bubbles [SM95]. The Potts model (in the limit $q \to 1$) is isomorphic to a site-bond percolation problem [KF69, Lub79, CK80] and for $q = 2$ it corresponds to the Ising model [LC00]. There are interesting experimental realizations for $q = 3$ (e.g. Kr on Graphite [BH86]), $q = 4$ and $q = \infty$ (e.g. froths and metallic grains [GAG89]).

In this chapter, based on the exact density functional for the one–dimensional q-state Potts model [BMD00], we investigate the quality of various approximations often employed in DFT and TDFT. After presenting a general scheme for treating systems with internal degrees of freedom, we first consider the mean spherical approximation (MSA) for the equilibrium properties, and show how it compares with a mean-field approach and the exact solution. We then derive the TDFT for the one–dimensional Potts model, which entails the treatment of the one-dimensional Ising model in [KDF+02]. As an application, we study the smoothening of an initial sharp-kink density profile. By comparison with Monte–Carlo simulations we show that the TDFT provides a significant improvement over kinetic mean field theory. Moreover, since in our case the TDFT is based on an exact density functional, the differences between the exact simulated and DFT results allow us to perform a specific test of the local equilibrium approximation used in the TDFT. Finally, we discuss principal limitations of the TDFT, caused by the use of the single-particle density profile to specify non-equilibrium states of the system. This amounts to an incorrect account of correlations.

5.2 DFT for Lattice Gases with Internal Degrees of Freedom

We consider a lattice gas where each site i is either vacant ($x_i^\alpha = 0$ for all α) or singly occupied by a particle in one of q internal states (note that this corresponds to a generalized Potts model with $q+1$ states). If state $\alpha \in \{1, \ldots, q\}$ is realized, $x_i^\alpha = 1$ and $x_i^\beta = 0$ for $\beta \neq \alpha$. Occupation numbers therefore satisfy $x_i^\alpha x_i^\beta = x_i^\alpha \delta_{\alpha\beta}$. The Hamiltonian including two particle interactions $\Phi_{i,j}^{\alpha\beta}$ and site energies

ϵ_i^α due to an external potential is given by

$$H = \frac{1}{2}\sum_{i\neq j}\sum_{\alpha,\beta}\Phi_{i,j}^{\alpha\beta}x_i^\alpha x_j^\beta + \sum_{i,\alpha}\epsilon_i^\alpha x_i^\alpha \tag{5.1}$$

The formal steps of DFT for fluids or lattice gases without internal degrees of freedom can be carried over to the case considered here. Appendix C details the steps to arrive at a variational principle based on the functional for the grand canonical potential

$$\Omega[\mathbf{p}] = F_{\mathrm{id}}[\mathbf{p}] + F_{\mathrm{ex}}[\mathbf{p}] + \sum_{i,\alpha}(\epsilon_i^\alpha - \mu_\alpha)p_i^\alpha. \tag{5.2}$$

μ_α is the chemical potential fixing the mean total occupation $\bar{p}_\alpha$ of state α and $\mathbf{p} = \{p_i^\alpha\}$ and $p_i^\alpha = \langle x_i^\alpha\rangle$ are the average occupation numbers. The minimum value of $\Omega[\mathbf{p}]$ is the grand-canonical potential at equilibrium. The free energy is decomposed into an 'ideal' part describing a non-interacting lattice gas,

$$F_{\mathrm{id}}[\mathbf{p}] = \left[\sum_{i,\alpha}p_i^\alpha \ln p_i^\alpha + \sum_i\left(1-\sum_\alpha p_i^\alpha\right)\ln\left(1-\sum_\alpha p_i^\alpha\right)\right] \tag{5.3}$$

and an excess part $F_{\mathrm{ex}}[\mathbf{p}]$ due to interactions (for convenience we set $k_BT = 1$). Derivatives of $F_{\mathrm{ex}}[\mathbf{p}]$ with respect to the p_i^α taken at the equilibrium profile yield a hierarchy of direct correlation functions [Eva79].

$$c_{i\alpha}^{(1)} = -\frac{\partial F_{\mathrm{ex}}[\mathbf{p}]}{\partial p_i^\alpha}, \quad c_{i\alpha,j\beta}^{(2)} = -\frac{\partial^2 F_{\mathrm{ex}}[\mathbf{p}]}{\partial p_i^\alpha \partial p_j^\beta}, \quad \text{etc.} \tag{5.4}$$

The equilibrium occupation is then obtained by minimizing $\Omega[\mathbf{p}]$ with respect to the p_i^α. The corresponding equations $\partial\Omega[\mathbf{p}]/\partial p_i^\alpha = 0$ determining the equilibrium profile are called structure equations. For a lattice system with internal degrees of freedom, they can be expressed as[Maa99].

$$\sum_\beta\left(1+\delta_{\alpha\beta}\exp\left[\epsilon_i^\alpha - \mu_\alpha - c_{i\alpha}^{(1)}\right]\right)p_i^\beta = 1. \tag{5.5}$$

This equation is reminiscent of the Fermi occupation statistics for p_i^β. This is a consequence of the premise that no more than one particle can occupy a site.

Since the exact form of the free energy is usually not known, an approximation for the direct correlation functions is needed. The pair correlation function is accessible through scattering experiments and is related to $c_{i\alpha,j\beta}^{(2)}$ by the Ornstein–Zernike equation. It can be derived [NDM93, Maa99] by differentiating $c_{i\alpha}^{(1)}$ from

the structure equation, and using the fact that $\Omega[\mathbf{p}]$ is the generating function for cumulants of x_i^α by differentiation with ϵ_i^α:

$$\tilde{c}_{ij}^{\alpha\beta} + \sum_{k,\gamma} \tilde{c}_{ik}^{\alpha\gamma}\, p_k^\gamma\, h_{kj}^{\gamma\beta} = h_{ij}^{\alpha\beta}, \quad \tilde{c}_{ij}^{\alpha\beta} = c_{i\alpha,j\beta}^{(2)} - \frac{\delta_{ij}}{1-\sum_\mu p_i^\mu}. \tag{5.6}$$

It relates the direct correlation function $c_{i\alpha,j\beta}^{(2)}$ entering $\tilde{c}_{ij}^{\alpha\beta}$ to the pair correlation function $g_{ij}^{\alpha\beta} = (1-\delta_{ij})\langle x_i^\alpha x_j^\beta\rangle / \langle x_i^\alpha\rangle\langle x_j^\beta\rangle$ in $h_{ij}^{\alpha\beta} = g_{ij}^{\alpha\beta} - 1$. In the limit $q = 1$ the known result for systems without internal degrees of freedom is recovered. The difference between $\tilde{c}_{ij}^{\alpha\beta}$ and $c_{i\alpha,j\beta}^{(2)}$ is a consequence of the discrete lattice and the single occupancy condition.

5.3 Application to the 1D Potts model

In the following, standard approximation schemes used in DFT are tested based on the one-dimensional Hamiltonian ($1 \le i \le M$)

$$H = \sum_{i,\alpha,\beta} v_i^{\alpha\beta} x_i^\alpha x_{i+1}^\beta + \sum_{i,\alpha} (\epsilon_i^\alpha - \mu_\alpha) x_i^\alpha\,, \tag{5.7}$$

which for $v_i^{\alpha\beta} = V\delta_{\alpha\beta}$ reduces to the standard Potts model [Pot52].

5.3.1 Exact density functional

For one-dimensional lattice gases with short range interactions, a general scheme for deriving exact density functionals based on Markov chains has recently been developed in [BMD00]. This approach in particular provides an exact functional for the Potts model, which has been derived earlier by Percus [Per82] for the continuous DFT. The functional can be written as

$$\begin{aligned}
\Omega[\mathbf{p}] \;=\; & \sum_{i=1}^{M}\Bigg\{\sum_{\alpha=1}^{q}(\epsilon_i^\alpha - \mu_\alpha)p_i^\alpha + \sum_{\alpha,\beta=1}^{q} v_i^{\alpha\beta}\Gamma_i^{\alpha\beta} + \\
& + \sum_\beta \left[\sum_\alpha \Gamma_i^{\alpha\beta}\log\frac{\Gamma_i^{\alpha\beta}}{p_{i-1}^\beta} + \Big(p_{i-1}^\beta - \sum_\alpha \Gamma_i^{\alpha\beta}\Big)\log\Big(1 - \frac{\sum_\alpha \Gamma_i^{\alpha\beta}}{p_{i-1}^\beta}\Big)\right] \\
& + \sum_\alpha \Big(p_i^\alpha - \sum_\beta \Gamma_i^{\alpha\beta}\Big)\log\Big(\frac{p_i^\alpha - \sum_\beta \Gamma_i^{\alpha\beta}}{1-\sum_\beta p_{i-1}^\beta}\Big) \\
& + \Big(1 - \sum_\beta (p_{i-1}^\beta + p_i^\beta) + \sum_{\alpha,\beta}\Gamma_i^{\alpha\beta}\Big)\log\Big(1 - \frac{\sum_\beta p_i^\beta - \sum_{\alpha,\beta}\Gamma_i^{\alpha\beta}}{1-\sum_\beta p_{i-1}^\beta}\Big)\Bigg\},
\end{aligned} \tag{5.8}$$

where the correlators

$$\Gamma_i^{\alpha\beta} = \langle x_{i-1}^\alpha x_i^\beta \rangle \tag{5.9}$$

have to be expressed by the mean occupation numbers $\{p_k^\gamma\}$. This is achieved by solving the correlator equations [BMD00]

$$\Gamma_i^{\alpha\beta} = e^{-v_i^{\alpha\beta}} \frac{(p_i^\alpha - \sum_\gamma \Gamma_i^{\alpha\gamma})(p_{i-1}^\beta - \sum_\delta \Gamma_i^{\delta\beta})}{1 - \sum_\gamma (p_{i-1}^\gamma + p_i^\gamma) + \sum_{\gamma,\delta} \Gamma_i^{\delta\gamma}} \,. \tag{5.10}$$

A simpler expression for the functional is obtained if the vacancies are considered as an additional Potts state with index $\alpha = 0$ (and $v_i^{\beta 0} = v_i^{0\beta} = 0$), whereby the lengthy entropic part reduces to $\sum_{i=1}^M \sum_{\alpha,\beta=0}^q \Gamma_i^{\alpha\beta} \log(\Gamma_i^{\alpha\beta}/p_i^\alpha)$. In the fully occupied case ($\sum_\alpha x_i^\alpha = 1$) the solution of eqs. (5.10) requires a careful limiting procedure by letting the vacancy concentration go to zero.

The structure equations read

$$e^{-(\epsilon_i^\alpha - \mu_\alpha)} = \frac{(1 - \sum_\beta p_i^\beta)\left(p_i^\alpha - \sum_\gamma \Gamma_i^{\alpha\gamma}\right)\left(p_i^\alpha - \sum_\delta \Gamma_{i+1}^{\delta\alpha}\right)\frac{1}{p_i^\alpha}}{\left(1 - \sum_\beta (p_{i-1}^\beta + p_i^\beta) + \sum_{\gamma,\delta} \Gamma_i^{\delta\gamma}\right)\left(1 - \sum_\beta (p_i^\beta + p_{i+1}^\beta) + \sum_{\gamma,\delta} \Gamma_{i+1}^{\delta\gamma}\right)} \,. \tag{5.11}$$

By solving this equation numerically we obtain the exact density profiles.

5.3.2 Mean spherical approximation (MSA)

In general, an exact density functional as presented in the previous section is not available and the excess density functional will have to be approximated. In this section $\Delta F_{\rm ex}[\mathbf{p}]$ will be expanded around a homogeneous reference state[1], $p_i^\alpha = \bar{p}$. For simplicity, we here consider the standard Potts case $v_i^{\alpha\beta} = V\delta_{\alpha\beta}$.

Defining $\Delta p_i^\alpha = p_i^\alpha - \bar{p}$, $\Delta\Omega[\mathbf{p}] = \Omega[\mathbf{p}] - \Omega[\{\bar{p}\}]$, etc., we can write

$$\Delta\Omega[\mathbf{p}] = \Delta F_{\rm id}[\mathbf{p}] + \Delta F_{\rm ex}[\mathbf{p}] + \sum_{i,\alpha} \tilde{\epsilon}_i^\alpha \Delta p_i^\alpha \,. \tag{5.12}$$

When retaining only terms up to second order in the excess free energy functional, we find

$$\Delta F_{\rm ex}[\mathbf{p}] = -\sum_{i,\alpha} c^{(1)}(\bar{p}) \Delta p_i^\alpha - \frac{1}{2} \sum_{i,\alpha,j,\beta} c_{\alpha\beta}^{(2)}(|i-j|, \bar{p}) \Delta p_i^\alpha \Delta p_j^\beta \,, \tag{5.13}$$

[1] An alternative possibility would be to choose a reference state being homogeneous in space but inhomogeneous in the space of Potts states, i.e. $p_i^\alpha = \bar{p}_\alpha$. In certain applications this might be advantageous. For simplicity, however, we will not consider this case here.

where $c^{(1)}(\bar{p})$ can be subsumed into the chemical potential. For our choice of interactions with translational symmetry, $g_{ij}^{\alpha\beta} = g_{\alpha\beta}(|i-j|)$, and the direct correlation function $\tilde{c}_{ij}^{\alpha\beta} = c_{\alpha\beta}^{(2)}(|i-j|,\bar{p}) - \delta_{ij}/[1-q\bar{p}]$ can be split into two parts,

$$\tilde{c}_{ij}^{\alpha\beta} = \delta_{\alpha\beta} c_1(|i-j|) + (1-\delta_{\alpha\beta}) c_2(|i-j|)\,. \tag{5.14}$$

The direct correlation functions are to be determined from the OZ equation with a closure condition using the given two-body interactions. Due to the single occupancy condition, the interaction potential has a hard sphere character at least on the length scale of a lattice site. For such potentials, the mean spherical approximation (MSA) is a natural choice for the closure condition. In the MSA, the pair correlation function is exactly reproduced at the hard core scale by $g_{\alpha\beta}(0) = 0$, reflecting the single occupancy condition. For larger distances, starting at neighboring sites, the direct correlation functions in MSA are

$$c_1(|l|) = \begin{cases} -V, & |l| = 1 \\ 0, & |l| \geq 2 \end{cases} \qquad \text{and} \qquad c_2(|l|) = 0 \quad \text{for} \quad |l| \geq 1. \tag{5.15}$$

The two unknowns $c_1(0)$ and $c_2(0)$ are found using the Ornstein–Zernike equation (5.6) in Fourier space, which yields[Maa99]

$$\begin{aligned} c_1(0) =& \frac{1+\bar{p}-q\bar{p}}{\bar{p}(1-q\bar{p})} - \frac{1}{q}\left[A + (q-1)B\right] \\ c_2(0) =& \frac{1}{1-q\bar{p}} - \frac{1}{q}\left[A - B\right] \\ \text{with} \qquad A =& \frac{\sqrt{1+[2V\bar{p}(1-q\bar{p})]^2}}{\bar{p}(1-q\bar{p})},\ B = \frac{\sqrt{1+(2V\bar{p})^2}}{\bar{p}}\,. \end{aligned} \tag{5.16}$$

As an example, we now consider the special case of zero external energies for the Potts states $\alpha = 2, \ldots, q$ and alternating external energies for the Potts state $\alpha = 1$,

$$\epsilon_i^\alpha = \begin{cases} \epsilon, & i \text{ even and} \quad \alpha = 1 \\ 0, & \text{otherwise} \end{cases} \tag{5.17}$$

and assume $\mu_\alpha = \mu$ independent of α. Due to the symmetry of this external potential, each occupation number p_i^α is equal to one of the four representatives $p_0^1, p_0^2, p_1^1, p_1^2$, and the mean particle density per site is

$$\bar{n} = \frac{1}{2}\left[p_0^1 + p_1^1 + (q-1)(p_0^2 + p_1^2)\right]. \tag{5.18}$$

We consider the functional

$$
\begin{aligned}
\Psi[\mathbf{p}] \equiv & \frac{1}{M}\left(\Delta\Omega[\mathbf{p}] + F_{\mathrm{id}}[\bar{p}]\right) \\
= & \frac{1}{2}\big[p_0^1 \ln p_0^1 + p_1^1 \ln p_1^1 + (q-1)\left(p_0^2 \ln p_0^2 + p_1^2 \ln p_1^2\right) \\
& + \left(1 - p_0^1 - (q-1)p_0^2\right) \ln\left(1 - p_0^1 - (q-1)p_0^2\right) \\
& + \left(1 - p_1^1 - (q-1)p_1^2\right) \ln\left(1 - p_1^1 - (q-1)p_1^2\right)\big] \\
& - \frac{1}{4}\Bigg[\left(c_1(0) + \frac{1}{1-q\bar{p}}\right)\left((\Delta p_0^1)^2 + (\Delta p_1^1)^2 + (q-1)\left((\Delta p_0^2)^2 + (\Delta p_1^2)^2\right)\right) \\
& \quad + \left(c_2(0) + \frac{1}{1-q\bar{p}}\right)(q-1)\left\{2\left(\Delta p_0^1 \Delta p_0^2 + \Delta p_1^1 \Delta p_1^2\right)\right. \\
& \qquad\qquad \left. + (q-2)\left((\Delta p_0^2)^2 + (\Delta p_1^2)^2\right)\right\} \\
& \quad - 4V\left(\Delta p_0^1 \Delta p_1^1 + (q-1)\Delta p_0^2 \Delta p_1^2\right)\Bigg] \\
& + \frac{1}{4}\epsilon\left[p_0^1 - p_1^1 - (q-1)(p_0^2 + p_1^2) + 2(q-1)\bar{p}\right] \\
& - \mu_{\mathrm{eff}}\left[\frac{1}{2}\left(p_0^1 + p_1^1 + (q-1)(p_0^2 + p_1^2)\right) - \bar{n}\right].
\end{aligned}
\tag{5.19}
$$

with $\mu_{\mathrm{eff}} = \mu - \epsilon/2 + c^{(1)}(\bar{p})$. The structure equations are obtained by setting the derivatives of $\Psi[\mathbf{p}]$ with respect to $p_0^1, p_0^2, p_1^1, p_1^2$ equal to zero. These equations are solved numerically subject to a fixed $\bar{n}$ in eq. (5.18) (which is equivalent to $\partial\Psi/\partial\mu_{\mathrm{eff}} = 0$).

To establish a connection to mean-field theory, we write

$$
x_i^\alpha x_{i+1}^\beta = x_i^\alpha \langle x_{i+1}^\beta \rangle + \langle x_i^\alpha \rangle x_{i+1}^\beta - \langle x_i^\alpha \rangle \langle x_{i+1}^\beta \rangle + (x_i^\alpha - \langle x_i^\alpha \rangle)(x_{i+1}^\beta - \langle x_{i+1}^\beta \rangle). \tag{5.20}
$$

It can then be shown that neglecting the last term when inserting into eq. (5.7) amounts to an expression equal to (5.13) in the MSA approximation with $c_1(0) = c_2(0) = 0$. Ordinary mean field theory can therefore be recovered from the functional by setting $c_1(0) = c_2(0) = 0$.

In Fig. 5.3.2 the occupation numbers for the MSA approximation and the mean field theory are compared with the exact results based on eq. (5.11). Without interactions ($V = 0$) the external potential yields mean occupation numbers $p_0^1 < p_1^1 = p_1^2 < p_0^2$, $p_0^1 = e^{-\epsilon} p_0^2$. When a repulsive interaction $V > 0$ is switched on, the fact that $p_1^1 > p_1^2$ induces an increasing occupation difference. For larger q this effect becomes less pronounced due to the increasing contribution of the entropy to the free energy per site.

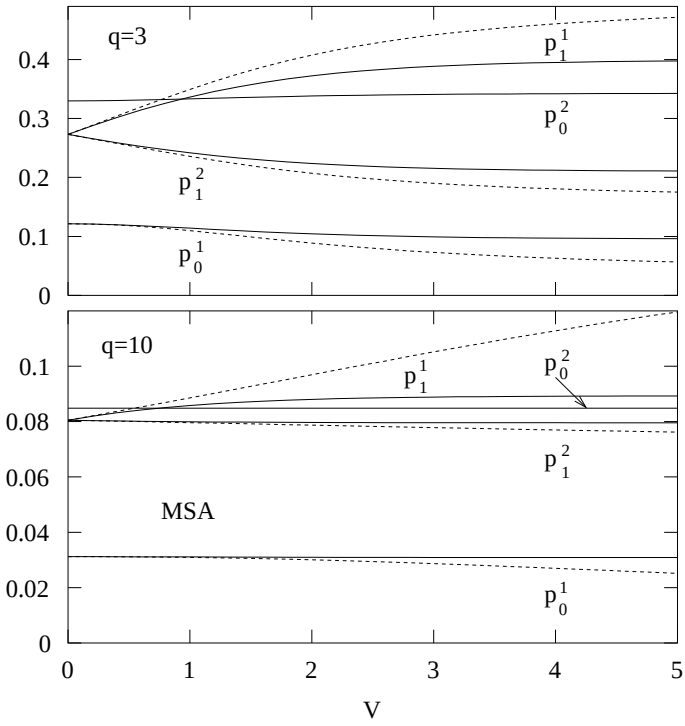

Figure 5.1: Comparison of the occupation numbers p_0^1, p_1^1 and p_1^2 in dependence of interaction strength V for two q values in the MSA approximation (dashed lines) with the exact solution (solid lines) for $\bar{n} = 0.8$ and $\epsilon = 1$. The corresponding MSA results for p_0^2 (not shown) are always close to the exact solution.

As expected, the MSA is an improvement over the simple mean field approximation especially for higher values of the interaction parameter and high overall densities $\bar{n}$. Moreover, the quality of the MF-results can be shown to improve when ϵ is decreased. A notable result is the improvement of the two approximations for larger q, reflecting the fact that mean-field descriptions should become exact in the limit $q \to \infty$.

5.3.3 Kinetics of density profiles

So far we have considered density profiles at equilibrium. In order to account for the time evolution of non-equilibrium profiles we will make use of the local equilibrium approximation for the probability distribution $P(\mathbf{x}, t)$ to find a configuration $\mathbf{x} = \{x_i^\alpha\}$ at time t. In this time-dependent density functional theory (TDFT) [RD96, GPDM03], the deviations of $P(\mathbf{x}, t)$ from the Boltzmann equilibrium distribution are described by a one-particle time-dependent effective

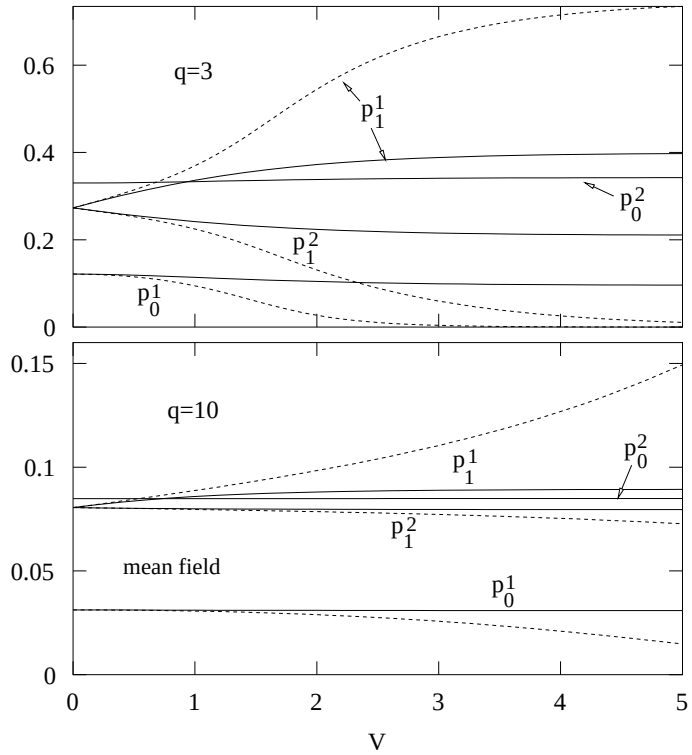

Figure 5.2: Comparison of the occupation numbers p_0^1, p_1^1 and p_1^2 in dependence of interaction strength V for two q values in the mean field approximation (dashed lines) with the exact solution (solid lines) for $\bar{n} = 0.8$ and $\epsilon = 1$. The corresponding mean field results for p_0^2 (not shown) are always close to the exact solution.

potential $h_i^\alpha(t)$,

$$P(\mathbf{x}, t) = \frac{1}{Z(t)} \exp\left[-H(\mathbf{x}) - \sum_{i,\alpha} h_i^\alpha(t) x_i^\alpha\right] . \tag{5.21}$$

The effective potential is the unique potential, which yields the instantaneous density profile $p_i^\alpha(t)$ according to the equilibrium DFT. Accordingly, the unknown field $\mathbf{h}$ in eq. (5.21) can be determined by the "structure equation" $h_i^\alpha(t) = -\partial\Omega[\mathbf{p}]/\partial p_i^\alpha$ with $\Omega[\mathbf{p}]$ from eq. (5.2). It is then clear that in this approach all equilibrium relations between occupational correlators $\langle x_i^\alpha x_j^\beta \ldots\rangle$ and the density $\mathbf{p}$ also apply at each time instant to the non-equilibrium situation [in particular eq. (5.10)]. This should work well in cases where the correlators reach their equilibrium values quickly enough on the time scale of changes in the densities. Since deviations of the correlators from the ones for the instantaneous density in equilibrium cannot be captured with the one-particle potential $h_i^\alpha(t)$, the approach is attributed mean-field character in time. The system will evolve towards the equilibrium distribution, so that consistency of kinetics and thermodynamics is ensured. Because the equilibrium properties are captured exactly by the exact

density functional, we can specifically test the quality of the approximation in time.

To test the quality of the TDFT, we consider a lattice with all sites being occupied ($\bar{n} = 1$) and a non-conserved dynamics, where a given Potts state α on lattice site i can change to any other state $\beta \neq \alpha$ with a rate $w_i^{\alpha\beta}(\mathbf{x})$ that depends on the current state $\mathbf{x}$ due to interactions. In the following we will start with the master equation and derive a closed set of equations for the occupation probabilities without the need to calculate $h_i^\alpha(t)$ explicitly from the density functional. This is possible because the Markov property allows to break down multi-point correlators to two-point correlators, which depend on the density by the known expressions from the exact DFT presented in sec. 5.3.1. From the master-equation describing this stochastic process, we derive the equation of motion for the occupation profile,

$$\frac{dp_i^\alpha}{dt} = \sum_\beta \langle (x_i^\beta - x_i^\alpha) w_i^{\alpha\beta} \rangle_t \tag{5.22}$$

where $\langle \ldots \rangle_t$ denotes an average with respect to the non-equilibrium distribution $P(\mathbf{x}, t)$. For the rates we choose a generalized Glauber form,

$$\begin{aligned} w_i^{\alpha\beta}(\mathbf{x}) = &\left(1 - \tanh\left[(x_{i-1}^\beta x_i^\beta - x_{i-1}^\alpha x_i^\alpha)V/2\right]\right) \\ &\times \left(1 - \tanh\left[(x_{i+1}^\beta x_i^\beta - x_{i+1}^\alpha x_i^\alpha)V/2\right]\right) , \end{aligned} \tag{5.23}$$

which satisfies the condition of detailed balance [2]. Detailed balance alone is not a sufficient condition to make the dynamics unambiguous. In fact, it was shown that for the Potts model a range of dynamical critical exponents can be attained by appropriate choice of the transitions rates[WKA86]. In the kinetic MC simulations, presented at the end of this section, the same generalized Glauber form was implemented in order to allow for comparison.

When substituting eq. (5.23) in (5.22) further evaluation is made possible by noting that the factor in front of $V/2$ in the argument of tanh is always $-1, 0$ or 1, so that it can be taken out from the tanh function. With the help of the Markov property, three-point correlators can exactly be reduced to two-point correlators, e.g. $\langle x_{i-1}^\alpha x_i^\beta x_{i+1}^\gamma \rangle = \Gamma_i^{\alpha\beta} \Gamma_{i+1}^{\beta\gamma} / p_i^\beta$. **Beweis in Anhang ?** After some algebra we

[2] For a Hamiltonian H that is decomposable into independent parts, $H = \sum_i H_i$, the generalized Glauber rate w_{ab} for a transition from an initial state a to a final state b in the form $w_{ab} = \prod_i \{1 - \tanh[(H_i^{(b)} - H_i^{(a)})/2]\}$ always satisfies the condition of detailed balance.

then find

$$\begin{aligned}\frac{dp_i^\alpha}{dt} &= 1 - qp_i^\alpha + \tanh(V/2)\Big[2p_i^\alpha - p_{i-1}^\alpha - p_{i+1}^\alpha \\ &\qquad + \sum_\beta \Big(\Gamma_i^{\beta\beta} - \Gamma_i^{\alpha\alpha} + \Gamma_{i+1}^{\beta\beta} - \Gamma_{i+1}^{\alpha\alpha}\Big)\Big] \\ &\quad + \tanh^2(V/2) \sum_\beta \Big[\frac{1}{p_i^\beta}(\Gamma_i^{\alpha\beta} - \Gamma_i^{\beta\beta})(\Gamma_{i+1}^{\beta\alpha} - \Gamma_{i+1}^{\beta\beta}) \\ &\qquad - \frac{1}{p_i^\alpha}(\Gamma_i^{\beta\alpha} - \Gamma_i^{\alpha\alpha})(\Gamma_{i+1}^{\alpha\beta} - \Gamma_{i+1}^{\alpha\alpha})\Big]. \qquad (5.24)\end{aligned}$$

Equations (5.24) together with the correlator equations (5.10) form a complete set of equations for the time evolution of density profiles and can be solved numerically for a given initial condition.

As an example, we consider an initially sharp kink profile at time $t = 0$, where the left part of the system is in Potts state $\alpha = 1$ and the right part in Potts state $\alpha = q$ with fixed boundary sites $i = 1$ and M in Potts states $\alpha = 1$ and q, i.e. $x_1^\alpha = \delta_{\alpha,1}$ and $x_M^\alpha = \delta_{\alpha,q}$. In Figure 5.3a we compare the time evolution of the profile with the results from continuous-time Monte–Carlo simulations (for details of the algorithm, see appendix B.1). Because of divergences in the correlator equations, the computations were performed with an occupation slightly below 1. At the boundaries, the correlators could be evaluated simply as $\langle x_1^\alpha x_2^\beta \rangle = \langle \delta_{\alpha,1} x_2^\beta \rangle = \delta_{\alpha,1} p_2^\beta$. The agreement of the TDFT solution with the simulations is excellent at all times and both approaches yield the correct equilibrium profile for large times. In order to obtain this agreement, it was necessary to adjust the time scale according to $t_{\mathrm{TDFT}} = 0.85\, t_{\mathrm{KMC}}$. The significant improvement over a simple mean-field treatment corresponding to factorization of all correlators in eq.(5.24), i.e. $\Gamma_i^{\alpha\beta} = p_{i-1}^\alpha p_i^\beta$, etc., can be seen by comparing Fig. 5.3a with Fig. 5.3b. The mean-field approximation is insufficient from the beginning and does not provide the correct equilibrium profile for long times.

5.4 Basic Limitations of TDFT

Since in the kinetic equation of the TDFT only the densities (mean occupation numbers) enter, the TDFT can not distinguish between states with the same density profile but different correlations. As a consequence, the time evolution of a non-equilibrium state with the equilibrium density profile cannot be captured. This issue may become important when considering memory effects in systems with slow relaxations, as for example glassy systems. The observables used to characterize the thermodynamic states of such systems (as e.g. density) may have equal values initially, but very different time evolutions depending on the systems' history.

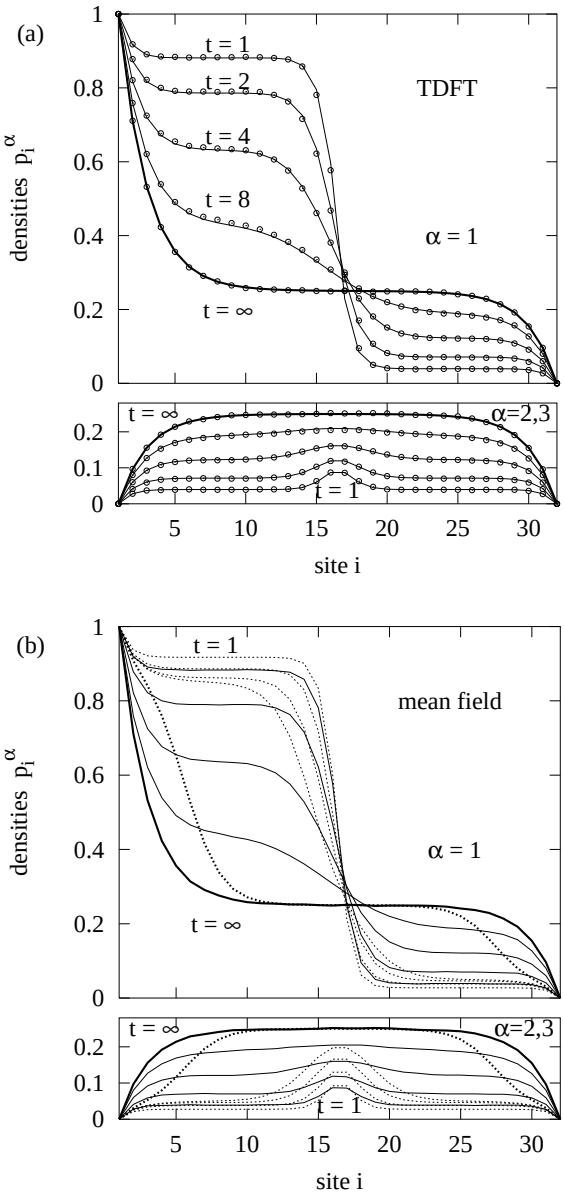

Figure 5.3: (a) Comparison of the evolution of an initial kink profile calculated using TDFT (lines) with Monte–Carlo simulations (points) for a system with 32 particles, $q = 4$ and $V = -2$. Boundary conditions are $p_1^\alpha = \delta_{\alpha,1}$ and $p_M^\alpha = \delta_{\alpha,4}$. Results are shown for $t = 1, 2, 4, 8$ and the equilibrium density (thick lines). Results for $\alpha = 4$ (not shown) are mirror images of those for $\alpha = 1$ with respect to the center site $i = 16$. (b) Comparison of mean field theory (dotted lines) with the simulations (solid lines) for the same system as shown in (a). Equilibrium solutions are indicated with thick lines.

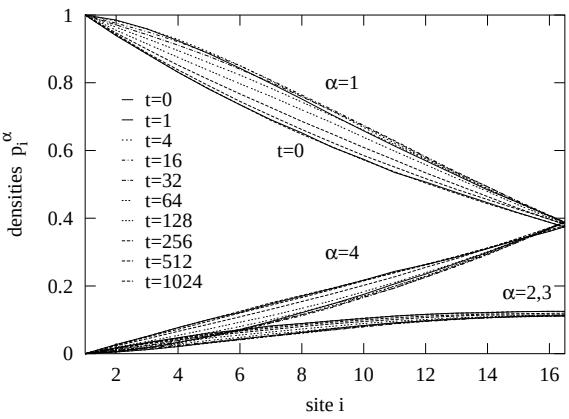

Figure 5.4: Evolution of a density profile starting from the equilibrium density, but with non-equilibrium correlators (see text) for $V = -4$ and $q = 4$. The system quickly reaches the state with maximum deviation from the equilibrium density at $t \approx 1$ and then relaxes to the original equilibrium density profile. Only the left half of the system is shown.

To illustrate this principal failure of the TDFT, we generate states of the Potts model with the same mean occupation numbers but different correlations for the same system as in the previous chapter. To achieve this, we first determine the equilibrium profile p_i^α for a system with interactions from the structure equations (5.11). This profile is also the equilibrium profile for a system without interactions ($V = 0$) and external potential $\epsilon_i^\alpha = -\log p_i^\alpha$. Hence by taking the equilibrium state of the non-interacting system as initial non-equilibrium state for the interacting system, we can study by Monte–Carlo simulations the time development of a density profile that according to TDFT cannot change.

Figure 5.4 shows the effect for $V = -4$ and $q = 4$. Although the mean occupation numbers at time $t = 0$ are the same as in the equilibrium state reached for $t \simeq 1024$, there is a pronounced change in the occupation profile at intermediate times. These changes are due to the fact that in the initial state the correlations between occupation numbers are not the equilibrium ones. The configurations with large statistical weights in the initial state exhibit stronger short-wavelength fluctuations and in order for the correlations to build up, the system has to pass through intermediate states with a non-equilibrium profile.

5.5 Summary and Discussion

We extended lattice gas DFT to systems with internal degrees of freedom. In particular, we presented the Ornstein–Zernike equation for this case, which is often used as a starting point to derive functionals for the excess free energy.

As an example, we chose the Potts model in one dimension, because an exact functional is available in this case. We demonstrated the usual steps in derivation of an approximate functional for DFT by application of the MSA. The resulting densities are a significant improvement over mean-field theory.

The kinetics of density profiles were investigated with TDFT. The use of the exact equilibrium functional in the local equilibrium approximation yields densities in excellent agreement to KMC simulations. Finally, we demonstrated that TDFT based on single particle potentials cannot capture the evolution of states where correlations deviate significantly from the ones for an equilibrium state with the same density. The limitation of using single particle potentials to describe deviations from equilibrium may be overcome by extending density functional theory to the case where two-point densities uniquely determine two-point potentials which may then also be used to describe deviations from equilibrium[GPDM03]. The approach by Nastar *et al.* [NC04] also includes multi-point correlations and can describe the transport of different species with currents related to non-diagonal Onsager coefficients. How this approach compares to a TDFT based on two-point functionals will be of interest in further research.

6 Summary and Outlook

Appendix

A Rates of Processes in second layer nucleation

A.1 Encounter rates $\omega_n(R)$

We want to calculate the characteristic rate $\omega_n(R)$ for an encounter of i+1 atoms, if initially $n \geq i+1$ atoms are randomly placed on top of an island with radius R and infinite step edge barrier ($\alpha = 0$). For this purpose let us consider the encounter as a sequential process as depicted in Fig. A.1 (for $i = 3$ and $n = 5$): First a dimer forms, then one of the remaining atoms attaches to the dimer and a trimer is created, and so on until a stable cluster composed of i+1 atoms has been formed. Denoting the rate for the formation of the dimer by w_1, and the rate for the attachment of an atom to an already existing cluster composed of k atoms ("k-cluster") by w_k, we may write

$$w_1 = \frac{n(n-1)}{2} \frac{2D}{a^2} \frac{b_1 a^2}{\pi R^2}\,, \tag{A.1}$$

$$w_k = (n-k) \frac{D}{a^2} \frac{b_k a^2}{\pi R^2}\,, \qquad 2 \leq k \leq i\,. \tag{A.2}$$

The factors b_k can be viewed as the effective number of perimeter sites of a k-cluster. Similarly, we may write for the rate of dissociation v_k of a single atom from a k-cluster (in the case of negligible binding energies of unstable clusters)

$$v_k = d_k \frac{D}{a^2}\,, \qquad k \geq 2\,, \tag{A.3}$$

where again d_k has the meaning of an effective number of perimeter sites. (In principle one may also take into account the possibility that a subcluster composed of more than one atom can dissociate from an unstable cluster and other states with various intermediate unstable clusters of size $2 \leq k \leq i$.)

The idea now is to renormalize the process depicted in Fig.A.1 by replacing it by an effective transition rate w_{eff} between the initial state composed of n isolated atoms and the final state containing the stable cluster. Clearly, such a replacement is only approximately valid. After the replacement, the encounter rate $\omega_n(R)$ in eq. (3.17) can be identified with w_{eff}. In order to derive w_{eff}, we consider a stationary situation, where the probability p_1 of the initial state is kept

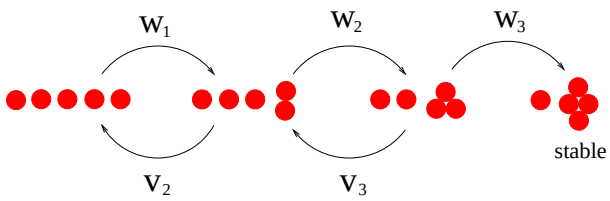

Figure A.1: Illustration of the encounter of 4 atoms out of $n=5$ adatoms. The 4 connected atoms are supposed to form a stable cluster ($i=3$). First a dimer forms with a rate w_1 then a trimer with a rate w_2, and finally the stable quadrumer with a rate w_3. The sequential process only leads to the formation of a stable cluster, if neither the dimer dissociates with the rate v_2 nor the trimer dissociates with the rate v_3.

fixed and a constant current J flows between neighboring states containing a k- and $k+1$-cluster. We thus write

$$J = w_k p_k - v_{k+1} p_{k+1}\,, \qquad 1 \le k \le i-1\,, \tag{A.4}$$

where p_k denotes the probability of the state containing a k-cluster. The set of equations (A.4) can be readily solved for p_i yielding

$$J = w_i p_i = w_1 p_1 \prod_{k=2}^{i} \frac{w_k}{v_k} - J \sum_{k=2}^{i} \prod_{j=k}^{i} \frac{w_j}{v_j}\,. \tag{A.5}$$

On the other hand we have

$$J = w_{\text{eff}} p_1\,. \tag{A.6}$$

Eliminating J from eqs. (A.5),(A.6), we obtain

$$w_{\text{eff}} = \frac{w_1 \prod_{k=2}^{i} w_k/v_k}{1 + \sum_{k=2}^{i} \prod_{j=k}^{i} w_j/v_j}\,. \tag{A.7}$$

For large radii $R \gg a$, it holds $w_j/v_j \ll 1$ so that we can neglect the sum over k in the denominator on the right hand side of (A.7). Hence we find

$$\omega_n(R) \simeq w_{\text{eff}} \simeq \kappa_{\text{e}} \left[\prod_{k=0}^{i}(n-k)\right] \frac{D}{a^2} \left(\frac{a^2}{\pi R^2}\right)^i\,, \tag{A.8}$$

where $\kappa_{\text{e}} = b_1 \prod_{k=2}^{i} b_k/d_k$.

A.2 Lifetime $\tau_n(R)$

In this Appendix we first derive the lifetime $\tau_n(R)$ of a state with n atoms on top of an island with radius R in the continuum limit based on the diffusion equation

supplemented by the boundary conditions (3.7). This is then used to show that the probability $p_n(R(t))$ to find exactly n atoms on the island at time t equals a Poisson distribution (when disregarding any possible nucleation events). The mean number $\bar{n}(R(t))$ of atoms on the island characterizing the Poisson distribution is given explicitly for the generic growth law $R(t)$ specified in eq. (2.7) and the resulting expression is taken to renormalize "bare coefficients" in the formula found for $\tau_n(R)$. Finally, we discuss the lattice corrections to the renormalized coefficients to obtain the values for κ_1 and κ_2 given in the text (see the discussion right after eq. (3.18)).

The solution of the diffusion problem[1]

$$\frac{\partial \rho}{\partial t} = D\,\Delta\rho\,, \tag{A.9}$$

$$\frac{\partial \rho}{\partial r}\Big|_{r=0} = 0\,, \quad \left[\frac{\partial \rho}{\partial r} + \frac{\alpha}{a}\rho\right]_{r=R} = 0 \tag{A.10}$$

with the initial condition $\rho(\mathbf{r}, t{=}0) = 1/(\pi R^2)$ has been derived by Harris [Har95]:

$$\rho(\mathbf{r}, t) = \sum_{k=1}^{\infty} \frac{c_k \lambda_k^2}{2\pi R^2 \frac{\alpha R}{a}} \frac{J_0(\frac{\lambda_k r}{R})}{J_0(\lambda_k)} \exp\Big(-\lambda_k^2 \frac{D}{R^2} t\Big)\,. \tag{A.11}$$

Here $J_\nu(.)$ is the Bessel function of νth order, $c_k \equiv 4(\alpha R/a)^2/(\lambda_k^2[\lambda_k^2 + (\alpha R/a)^2])$ and λ_k is the kth root ($\lambda_1 < \lambda_2 < \ldots$) of

$$\Big(\frac{\alpha R}{a}\Big) J_0(\lambda) = \lambda J_1(\lambda)\,. \tag{A.12}$$

The solution (A.11),(A.12) describes the probability density for a single diffusing atom that at time $t = 0$ is randomly deposited on top of a circular island with a partially reflecting boundary. The probability that the atom has not escaped from the island up to time τ is $\Psi(\tau) = 2\pi \int_0^R dr\, r\, \rho(\mathbf{r}, t)$, which yields[Har95]

$$\Psi(\tau) = \sum_{k=1}^{\infty} c_k \exp\Big(-\lambda_k^2 \frac{D}{R^2}\tau\Big) \tag{A.13}$$

Note that, since $\Psi(0) = 1$, it must hold $\sum_{k=1}^{\infty} c_k = 1$.

[1] To simplify notation, we do not distinguish between the diffusion coefficient D_{cont} in the continuum limit and the coefficient D defining the jump rate D/a^2 of the adatoms on the substrate lattice. In two dimensions $D_{\text{cont}} = D/4$. In the case of heteroepitaxy, moreover, one has to replace D/a^2 by the jump rate on top of an island. Also, we do not introduce the edge crossing probability $\alpha_{\text{cont}} = \kappa_\alpha \alpha$ in the continuum limit, where the correction factor κ_α depends on both the lattice type and the shape of the island boundary. For a discussion of the lattice corrections, see Appendix A.2.

The probability that none of n independent atoms has escaped from the island up to time τ is $\Psi(\tau)^n$. Accordingly, the probability $\phi(\tau)d\tau$ that the *first* atom leaves the island in the time interval $[\tau, \tau+d\tau]$ is

$$\begin{aligned}\phi(\tau) &= -\frac{d\Psi(\tau)^n}{d\tau} = -n\Psi(\tau)^{n-1}\frac{d\Psi(\tau)}{d\tau} \\ &= n\frac{D}{R^2}\sum_{j_1,\ldots,j_n=1}^{\infty} c_{j_1\ldots c_{j_n}} \times \\ &\qquad \times \lambda_{j_1}^2 \exp\Big[-(\lambda_{j_1}^2+\ldots+\lambda_{j_n}^2)\frac{D}{R^2}\tau\Big],\end{aligned} \tag{A.14}$$

from which we find for the average time $\tau_n(R) \equiv \int_0^\infty d\tau\phi(\tau)\tau$,

$$\tau_n(R) = n\frac{R^2}{D}\sum_{j_1,\ldots,j_n=1}^{\infty} c_{j_1\ldots c_{j_n}} \frac{\lambda_{j_1}^2}{(\lambda_{j_1}^2+\ldots+\lambda_{j_n}^2)^2}\,. \tag{A.15}$$

It is easy to show that $j_{1,k} < \lambda_k < j_{0,k}$, where $j_{\nu,k}$ is the kth zero of $J_\nu(.)$. Since $j_{\nu,k} \sim (k+\nu/2-1/4)\pi$ for $k \gg \nu$, the terms in the series of (A.15) rapidly decrease with increasing j_k, $k = 1,\ldots,n$ (note that c_j depends on λ_j). The leading term can be obtained by setting $c_j = \delta_{j,1}$ in eq. (A.13), which amounts to a Poisson approximation of the escape process, $\Psi(\tau) \simeq \exp(-\lambda_1 D\tau/R^2)$. Within this approximation we obtain

$$\tau_n(R) = \frac{1}{n}\frac{R^2}{D}\frac{1}{\lambda_1^2}\,, \tag{A.16}$$

where λ_1 follows from eq. (A.12). In the limit of small $\alpha R/a \ll 1$ one finds $\lambda_1^2 \simeq 2\alpha R/a$, while in the limit of large $\alpha R/a \gg 1$, $\lambda_1^2 \simeq j_{0,1}^2$. Combining these two limits yields the interpolation formula

$$\tau_n(R) \simeq \frac{1}{n}\frac{R^2}{D}\left(\kappa_1\frac{a}{\alpha R}+\kappa_2\right) \tag{A.17}$$

with $\kappa_1 = 1/2$ and $\kappa_2 = 1/j_{0,1}^2 \cong 0.173$.

Knowing $\tau_n(R)$ we can set up the master equation for the probabilities $p_n(t)$ to find exactly n atoms on top of the island at time t in the presence of an incoming flux F, see eq. (3.19). Introducing the generating function $Q(z,t) \equiv \sum_{n=0}^{\infty} p_n(t)z^n$ we obtain from eq. (3.19)

$$\frac{\partial Q}{\partial t} = (z-1)\left[\pi F R^2 Q - \frac{1}{\tau_1(R)}\frac{\partial Q}{\partial z}\right], \tag{A.18}$$

For the moment $R = R(t)$ is a general growth law, that is assumed to be a monotonously increasing function of t ($\dot{R} \equiv dR/dt > 0$). Transforming variables

from t to R and defining $\tilde{Q}(z,R)\equiv Q(z,t(R))$ and $\zeta(R)\equiv\dot{R}(t(R))$, where $t(R)$ is the inverse function of $R(t)$, eq. (A.18) gives

$$\frac{\partial\tilde{Q}}{\partial R}+\frac{z-1}{\tau_1(R)\zeta(R)}\frac{\partial\tilde{Q}}{\partial z}=\frac{\pi F R^2(z-1)}{\zeta(R)}\tilde{Q}\,. \tag{A.19}$$

This is a semi-linear partial differential equation of first order that can be solved by the method of characteristics. For the initial condition $\tilde{Q}(z,R=0)=1$ we obtain

$$\tilde{Q}(z,R)=\exp\left[-(1-z)\bar{n}(R)\right]\,, \tag{A.20}$$

which for $p_n(R)=p_n(R(t))=[\partial_z^n\tilde{Q}(z,R)/n!]_{z=0}$ yields the Poisson distribution (3.20) with

$$\bar{n}(R)=\pi F\exp\left[-\int_0^R\frac{du}{\tau_1(u)\zeta(u)}\right]\int_0^R\frac{du\,u^2}{\zeta(u)}\exp\left[-\int_0^u\frac{du'}{\tau_1(u')\zeta(u')}\right] \tag{A.21}$$

For the generic growth law eq. (2.7) in particular, we obtain

$$\begin{aligned}\bar{n}(R) &= \frac{2\pi}{A^2\Gamma^{\frac{i}{i+2}}}(1+\tilde{\alpha}R)^{-\varphi}\int_0^R dx\,x^3\,(1+\tilde{\alpha}x)^{\varphi}\\ &= \frac{2\pi}{A^2\Gamma^{\frac{i}{i+2}}\tilde{\alpha}^4}(1+\tilde{\alpha}R)^{-\varphi}\end{aligned} \tag{A.22}$$

$$\times\left[\frac{(1+\tilde{\alpha}R)^{\varphi+4}-1}{\varphi+4}-3\frac{(1+\tilde{\alpha}R)^{\varphi+3}-1}{\varphi+3}+3\frac{(1+\tilde{\alpha}R)^{\varphi+2}-1}{\varphi+2}-\frac{(1+\tilde{\alpha}R)^{\varphi+1}-1}{\varphi+1}\right],$$

where $\tilde{\alpha}=\kappa_2\alpha/\kappa_1$ and $\varphi=2A^{-2}\Gamma^{2/(i+2)}/\kappa_2$. In the quasi-stationary case ($\partial_t Q=0$ in eq. (A.18)) one obtains

$$\bar{n}^{\rm st}(R)=\pi F R^2\tau_1(R)=\pi\frac{FR^4}{D}\left(\kappa_1\frac{a}{\alpha R}+\kappa_2\right)\,, \tag{A.23}$$

to which (A.22) simplifies for $\varphi\tilde{\alpha}R\ll 1$ (see the discussion right after eq. (3.21)).

Alternatively, we can determine $\bar{n}^{\rm st}(R)$ by integrating $\rho_1^{\rm st}(r)$ over the island area, which yields

$$\bar{n}^{\rm st}(R)=2\pi\int_0^R dr\,r\,\rho_1^{\rm st}(r)=\pi\frac{FR^4}{D}\left(\frac{1}{2}\frac{a}{\alpha R}+\frac{1}{8}\right)\,. \tag{A.24}$$

Hence we can improve the Poisson approximation by renormalizing the bare coefficient $\kappa_2=1/j_{0,1}^2\simeq 0.173$ to $\kappa_2=1/8$ (note that $\kappa_1=1/2$ does not change).
Finally, in order to obtain the constants κ_1 and κ_2 in eq. (3.18), one has to take into account the "lattice corrections". Let us denote by $\mathbf{l}$ the position of a lattice site and by $\boldsymbol{\delta}_j$ the nearest-neighbor bond vectors, i.e. for a triangular lattice

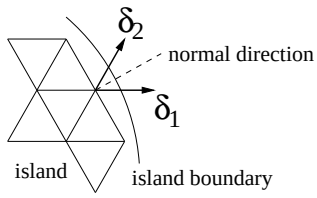

Figure A.2: Sketch of the island geometry in the neighborhood of a boundary site $\mathbf{l}$, from which two jumps in the directions $\boldsymbol{\delta}_1$ and $\boldsymbol{\delta}_2$ lead to an escape from the island over the step edge barrier.

$\boldsymbol{\delta}_j = (\cos[2\pi j/6], \sin[2\pi j/6])a,\ j = 0, \ldots, 5$. The master equation describing the diffusion of a single adatom on the island reads

$$\frac{\partial w(\mathbf{l},t)}{\partial t} = \frac{D}{6a^2} \sum_{j=0}^{5} \left[w(\mathbf{l} + \boldsymbol{\delta}_j, t) - w(\mathbf{l}, t) \right] , \tag{A.25}$$

where $w(\mathbf{l}, t)$ is the probability to find the atom at lattice site $\mathbf{l}$. Equation (A.25) is valid as long as $\mathbf{l}$ is not a boundary site. In the continuum limit we can write $\sum_{j=0}^{5}[w(\mathbf{l} + \boldsymbol{\delta}_j, t) - w(\mathbf{l}, t)] = (1/2) \sum_{j=0}^{5} (\boldsymbol{\delta}_j \cdot \boldsymbol{\nabla})^2 w(\mathbf{l}, t) + \mathcal{O}(a^4)$, which yields eq. (A.9) when D is replaced by $D_{\text{cont}} = D/4$ (see also the footnote on page 111). As a consequence, one has to substitute D by D_{cont} in all continuum equations, in particular in eq. (A.24), which means that in eq. (3.18) (referring to the lattice simulations) one should take $\kappa_1 = 4(1/2) = 2$ and $\kappa_2 = 4(1/8) = 1/2$.

The value of κ_1 is still not correct, since we have not taken into account the lattice correction to the parameter α. To derive this correction we consider a lattice site $\mathbf{l}$ at the boundary. For example, one may encounter the situation sketched in Fig. A.2, where $\boldsymbol{\delta}_0$ and $\boldsymbol{\delta}_1$ lead to sites outside the island (where $w(\mathbf{l} + \boldsymbol{\delta}_j, t) \equiv 0$) and the remaining nearest neighbor sites $\mathbf{l} + \boldsymbol{\delta}_j$, $j = 2, \ldots, 5$ are on the island. The equation corresponding to (A.25) then reads

$$\begin{aligned} \frac{\partial w(\mathbf{l},t)}{\partial t} &= \frac{\alpha D}{6a^2} \sum_{j=0}^{1} \left[w(\mathbf{l} + \boldsymbol{\delta}_j, t) - w(\mathbf{l}, t) \right] + \frac{D}{6a^2} \sum_{j=2}^{5} \left[w(\mathbf{l} + \boldsymbol{\delta}_j, t) - w(\mathbf{l}, t) \right] \\ &= -\frac{2\alpha D}{6a^2} w(\mathbf{l}, t) + \frac{D}{6a^2} \sum_{j=0}^{5} \left[w(\mathbf{l} + \boldsymbol{\delta}_j, t) - w(\mathbf{l}, t) \right] \\ &\quad - \frac{D}{6a^2} \sum_{j=0}^{1} \left[w(\mathbf{l} + \boldsymbol{\delta}_j, t) - w(\mathbf{l}, t) \right] . \end{aligned} \tag{A.26}$$

In a discretization of the second boundary condition in eq. (A.10) on a triangular lattice one has to eliminate the outer boundary points $\mathbf{l} + \boldsymbol{\delta}_0$ and $\mathbf{l} + \boldsymbol{\delta}_1$ via the discretized version of the "bulk equation" (A.10). This amounts to a cancellation of the term on the left hand side and the second term on the right hand side of

(A.26) in the continuum limit, and the replacement $\sum_{j=0}^{1}[w(\mathbf{l}+\boldsymbol{\delta}_j,t)-w(\mathbf{l},t)] = \sum_{j=0}^{1}(\boldsymbol{\delta}_j \cdot \boldsymbol{\nabla})w(\mathbf{l},t) + \mathcal{O}(a^2) \to \sqrt{3}a\partial w/\partial r$. Hence eq. (A.26) corresponds to the second boundary condition in eq. (A.10), when α is replaced by $\alpha_{\text{cont}} = 2\alpha/\sqrt{3}$ in eq. (A.10).

In general, k nearest neighbor sites of a boundary site $\mathbf{l}$ can lie outside the island ($k=1,\ldots,4$). The weights how often such $\mathbf{l}$ occur and the way the normal direction is oriented with respect to the nearest neighbor bond vectors leading to the sites outside the island depend sensitively on the shape of the island edge. Hence, the factor $2/\sqrt{3}$ is only an estimate, which gives an impression on the influence of the lattice correction to the coefficient κ_1. Our comparison with the simulation results in Fig. 3.5 yields $\alpha_{\text{cont}} \cong 2\alpha$, i.e. $\kappa_1 \cong 4(1/2)^2 = 1$. We note that in general lattice corrections have always to be included in a continuum description after the effective Schwoebel barrier (for the lattice) has been calculated from the microscopic barriers (see the footnote on page 17).

B Continuous–Time Monte–Carlo simulations

B.1 General description

The Continuous-time Monte-Carlo method or kinetic Monte-Carlo (KMC) method generates realizations of a stochastic process defined by a master equation. This allows one to study non-equilibrium systems in a natural way, because the time scale is already accurately represented. This is in contrast to standard MC algorithms which usually generate a chain of configurations with the aim to sample an *equilibrium* ensemble. When kinetic properties are to be obtained from standard MC simulations, the matching of a physical timescale to MC steps remains an open problem.

The KMC method is often applied to systems which can be described by a hopping motion of particles where the moves represent a slow subset of all degrees of freedom and the fast degrees of freedom, such as lattice vibrations, act as a heat bath[HTB90]. More microscopic methods, e.g. molecular dynamics and electronic structure calculations by density functional theory, may be used to calculate the jump rates, but are impractical for a study of much longer timescales. In contrast to the usual Monte–Carlo method, where moves may be rejected with a probability depending on the energy change, the KMC method generates a chain of configurations in a rejection-less way (the main idea was first put forward in [BKL75]). It is usually desirable to average over several realizations.

Since this thesis deals with lattice models, we formulate our description for discrete models, although the KMC method can be applied more generally. Such a choice is natural for lattice forming systems such as alloys, where the type of lattice is chosen according to the known crystallographic structure, e.g. fcc for $CoPt_3$. Each lattice site i can be either empty or occupied with state $\alpha \in 1 \dots q$, represented by occupation numbers $n_{i,\alpha}$ with $\sum_{\alpha=0}^{q} n_{i,\alpha} = 1$ and $\alpha = 0$ for a vacancy. In the context of a binary alloy $\alpha \in \{1, 2\}$ represents the two atomic species.

For L lattice sites, the system can be in any of $(q+1)^L$ states $\{n_{i,\alpha}\}$, denoted by $s \in \{1 \dots (q+1)^L\}$. For realistic dynamics in epitaxy, usually only processes with neighboring sites of each atom are allowed. Deposition events of adatoms are represented by transitions between states with an increasing number of atoms

$\sum_{i=1}^{L}\sum_{\alpha=1}^{q} n_{i,\alpha}$. In the case of the Potts model, particles do not move but may change their internal state.

The time dependent probability for the system being in state s is described by a master equation

$$\frac{dP(s)}{dt} = \sum_{s'} [W_{s' \to s} P(s') - W_{s \to s'} P(s)] \tag{B.1}$$

with rates $W_{s \to s'}$ for transitions from state s to state s'. The rates are chosen to obey the condition of detailed balance $W_{s' \to s} P_{\mathrm{eq}}(s') = W_{s \to s'} P_{\mathrm{eq}}(s)$, which precludes the occurrence of limit cycles and ensures that the correct equilibrium distribution P_{eq} can be attained[NB99]. We assume that the hopping process is sufficiently fast, so that particles moving close to each other cannot interfere during a transition.

Then the total transition rate for the system in state s is

$$W_{\mathrm{total}}(s) \;=\; \sum_{s'} W_{s \to s'}. \tag{B.2}$$

With $\Psi_s(\tau)$ we denote the (MARKOVian) probability distribution for a system being in state s at time t to remain in this state at least up to time $t+\tau$.

$\Psi_s(\tau)$ is called "waiting time distribution" or "lifetime distribution". When a process obeys a master equation (B.1), its waiting time distribution is exponential (it is called a POISSON process), since from the definition of Ψ_i one has to remove the gain term of eq. (B.1) and to sum over all accessible states s'. This yields

$$\frac{d}{dt}\Psi_s(t) \;=\; -W_{\mathrm{total}}(s)\,\Psi_s(t)\ , \tag{B.3}$$

and since $\Psi_s(0) = 1$ the lifetime distribution of state s is

$$\Psi_s(\tau) \;=\; e^{-W_{\mathrm{total}}(s)\tau} \tag{B.4}$$

and its density is

$$\psi_s(\tau) \;=\; W_{\mathrm{total}}(s)\, e^{-W_{\mathrm{total}}(s)\tau}\ . \tag{B.5}$$

The process is simulated by starting with a state s at time t. Then we draw a time increment τ according to eq. (B.5) and change to a state s' at time $t+\tau$. The new state is chosen among all states s' with a probability proportional to its rate $W_{s \to s'}$.

The procedure is repeated, until a desired maximal simulation time $t_{\max}$ or a certain number of atoms is reached. For a discussion in a wider context and more details, see e. g. [NB99]

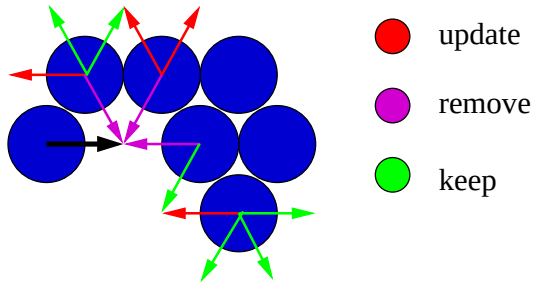

Figure B.1: Processes which need to be updated after the move of the particle on the left. Some processes need not be updated although the atoms involved are in direct vicinity of the moving atom.

B.2 Implementation for 3d growth

A straightforward implementation makes explicit reference to the lattice when querying for neighbors and takes periodicity of boundary conditions into account for each access to a neighbor of a lattice site. For the purpose of an efficient implementation of lattice algorithms, it is beneficial to make the algorithm independent of the lattice together with the specification of which directions are periodic. This can be achieved by making an abstraction to a graph where the lattice points are represented by vertices which are connected by edges to their neighbors. By using such data structures, the algorithm becomes independent of the particular choice of the lattice (fcc in this work) and boundary conditions. Storing the indices of neighbors was already suggested in [NB99]. A further improvement employed in this work is to store pointers to the data structures of the neighboring atoms, obviating the need for address calculations.

The lists for storing processes are organized into classes according to energy differences. For a given set of parameters, tables for the mapping of differences of bond numbers of the three types and extra interactions through the surface are set up, taking advantage of energy degeneracies. Depending on the choice of parameters, typically a few hundred classes result. By using reverse index lookup tables, insertions and deletions into process lists are $\mathcal{O}(1)$ operations, so that the total computational complexity for a given time increment scales with the number of active atoms. In the case of a limited number of classes, as in this case, this method is more efficient than a binary search tree for the whole process list[Sch02]. Such a tree could also be constructed for the classes, but the overhead involved would actually slow down the simulation, since the linear search for selecting a class begins with the one for energy difference 0, which contains a large fraction of the total rate, so that the full search is very rarely needed.

For KMC simulations, the update of possible processes in the vicinity of the moving atom is the most time consuming step. Since the rates depend on both the initial and final energies, possible moves of second nearest neighbor atoms around both sites involved in the process that is executed, are affected. However, for some of those moves the initial and final energies change in the same way, so that the difference and therefore also the class remains constant, see fig. B.1. Because the condition for excluding these possible moves does not depend on the exact occupation of the lattice sites, it is possible to list and store all processes that may be affected by a given process in a table for quick lookup. These tables take up most of the program‘s memory (a few hundred MBytes for clusters), but yield a significant speedup. In the case without exchange processes, the condition for the necessity of updating a process P from initial site P_i to final site P_f, when an atom has just moved from initial site M_i to M_f, can be succinctly formulated as

$$N(M_i, P_i) \oplus N(M_i, P_f) \vee N(M_f, P_i) \oplus N(M_f, P_f). \tag{B.6}$$

Here $N(s_1, s_2)$ is true if and only if sites with number s_1 and s_2 are neighbors in the lattice and $\oplus$ denotes the logical exclusive or operation. When allowing exchange processes for M, additional processes need to be updated.

C Fundamentals of Density Functional Theory

In order to derive the fundamentals of the DFT, we consider the grand canonical ensemble and supplement the Hamiltonian (5.1) with the chemical potential μ_α fixing the mean total occupation $\bar{p}_\alpha$ of state α:

$$H_\mu = H - \sum_{i,\alpha} \mu_\alpha x_i^\alpha. \tag{C.1}$$

The statistical operator in the grand canonical ensemble depends on $\{x_i^\alpha\}$ and is

$$\rho_0 = Z^{-1} e^{-\bar{\beta} H_\mu}, \quad Z = \mathbf{Tr}\, e^{-\bar{\beta} H_\mu} \tag{C.2}$$

Here, the trace $\mathbf{Tr}$ is the sum over all possible occupation states of the lattice $\mathbf{Tr}(\dots) = \sum_{\{x_i^\alpha\}}(\dots)$ and $\bar{\beta} = 1/k_\mathrm{B}T$.

Consider the functional

$$\Omega[\rho] = \mathbf{Tr}\, \rho\, (H_\mu + \bar{\beta}^{-1} \ln \rho) \tag{C.3}$$

for an arbitrary density $\rho[\{x_i^\alpha\}]$ with $\mathbf{Tr}\rho = 1$. Then, for $\rho \neq \rho_0$ we can prove the Gibbs inequality

$$\begin{aligned}
\Omega[\rho] &= \mathbf{Tr}\, \rho\, (H_\mu + \bar{\beta}^{-1} \ln \rho) \\
&= \mathbf{Tr}\, \rho\, (-\bar{\beta}^{-1} \ln \rho_0 - \bar{\beta}^{-1} \ln Z + \bar{\beta}^{-1} \ln \rho) \\
&= -\bar{\beta}^{-1} \ln Z\, \mathbf{Tr}\rho + \bar{\beta}^{-1} \mathbf{Tr}\, (\rho \ln \rho - \rho \ln \rho_0) \\
\Omega[\rho] - \Omega[\rho_0] &= \bar{\beta}^{-1} \mathbf{Tr} \left(\rho \ln \frac{\rho}{\rho_0} \right) = \bar{\beta}^{-1} \mathbf{Tr} \left(\rho_0 \left[\frac{\rho}{\rho_0} \ln \frac{\rho}{\rho_0} - \frac{\rho}{\rho_0} + 1 \right] \right) > 0.
\end{aligned} \tag{C.4}$$

We used that $\Omega[\rho_0]$ is the grand canonical potential and the fact that $x \ln x > x - 1$ for all $x \neq 1$.

The final step is to make the connection to the occupation densities with the theorem of Mermin[Mer65]. It states that for given occupation density $\mathbf{p} = \{p_i^\alpha = \mathbf{Tr}\, \rho\, x_i^\alpha\}$ and interactions, the external potential $\{\epsilon_i^\alpha\}$ is a unique function of $\{p_i^\alpha\}$.

The proof proceeds by assuming the contrary, i.e. two potentials $V = \sum_{i,\alpha} \epsilon_i^\alpha x_i^\alpha$ and V' in the full Hamiltonians H_μ and H'_μ with statistical operators ρ and ρ' which yield the same density $\mathbf{p}$.

We have with (C.4)

$$\begin{aligned} \Omega[\rho] &< \Omega[\rho'] = \mathbf{Tr}\ \rho'\,(H_\mu + \bar{\beta}^{-1}\ln\rho') \\ &= \Omega'[\rho'] + \mathbf{Tr}\ \rho'\,(H_\mu - H'_\mu) \\ &= \Omega'[\rho'] + \mathbf{Tr}\ \rho'\,(V - V') \end{aligned} \tag{C.5}$$

Swapping primed and unprimed quantities, we obtain

$$\Omega'[\rho'] < \Omega[\rho] + \mathbf{Tr}\ \rho\,(V' - V). \tag{C.6}$$

When adding the two inequalities, we find a contradiction

$$\begin{aligned} 0 &< \mathbf{Tr}\ (\rho'\,(V - V') + \rho\,(V' - V)) \\ &= \mathbf{Tr}\ (V - V')(\rho' - \rho) \\ &= \mathbf{Tr}\ \left(\sum_{i,\alpha} \epsilon_i^\alpha x_i^\alpha - \sum_{i,\alpha} \epsilon_i^{\alpha'} x_i^\alpha\right)(\rho' - \rho) \\ &= \sum_{i,\alpha} [\epsilon_i^\alpha \mathbf{Tr}\ x_i^\alpha(\rho' - \rho)] - \sum_{i,\alpha} \left[\epsilon_i^{\alpha'} \mathbf{Tr}\ x_i^\alpha(\rho' - \rho)\right] \\ &= 0. \end{aligned} \tag{C.7}$$

Therefore, the occupation density $\mathbf{p}$ uniquely determines the statistical distribution ρ and thus eq. (C.4) becomes

$$\Omega[\mathbf{p}] > \Omega[\mathbf{p}_0] \tag{C.8}$$

for a density $\mathbf{p} \neq \mathbf{p}_0$ and $\Omega[\mathbf{p}] = \Omega[\mathbf{p}_0]$ for $\mathbf{p} = \mathbf{p}_0$. The equilibrium density $\mathbf{p}_0$ therefore minimizes the functional $\Omega[\mathbf{p}]$ and the variational principle follows as a necessary condition

$$\left.\frac{\partial\Omega[\mathbf{p}]}{\partial p_i^\alpha}\right|_{\mathbf{p}_0} = 0. \tag{C.9}$$

Bibliography

[AF95] J. G. Amar and F. Family, *Critical cluster-size - island morphology and size distribution in submonolayer epitaxial-growth*, Phys. Rev. Lett. **74**(11), 2066 – 2069 (1995).

[AF96] J. G. Amar and F. Family, *Kinetics of submonolayer and multilayer epitaxial growth*, Thin Solid Films **272**(2), 208 – 222 (1996).

[AMM+02] M. Albrecht, M. Maret, A. Maier, F. Treubel, B. Riedlinger, U. Mazur, G. Schatz and S. Anders, *Perpendicular magnetic anisotropy in $CoPt_3$(111) films grown on a low energy surface at room temperature*, J. Appl. Phys. **91**(10), 8153–8155 (2002).

[AMT+01] M. Albrecht, A. Maier, F. Treubel, M. Maret, P. Poinsot and G. Schatz, *Self-assembled magnetic nanostructures of $CoPt_3$ with favoured chemical ordering*, Europhys. Lett. **56**(6), 884–890 (2001).

[BBC+94] P. Beauvillain, A. Bounouh, C. Chappert, R. Megy, S. Ouldmahfoud, J. P. Renard, P. Veillet, D. Weller and J. Corno, *Effect of submonolayer coverage on magnetic-anisotropy of ultrathin cobalt films M/Co/Au(111) with M=Au, Cu, Pd*, J. Appl. Phys. **76**(10), 6078 – 6080 (1994).

[BBJ+99] H. Brune, G. S. Bales, J. Jacobsen, C. Boragno and K. Kern, *Measuring surface diffusion from nucleation island densities*, Phys. Rev. B **60**(8), 5991 – 6006 (1999).

[BBR+95] H. Brune, K. Bromann, H. Roder, K. Kern, J. Jacobsen, P. Stoltze, K. Jacobsen and J. Norskov, *Effect of strain on surface-diffusion and nucleation*, Phys. Rev. B **52**(20), 14380 – 14383 (1995).

[BBRK95] K. Bromann, H. Brune, H. Roder and K. Kern, *Interlayer mass-transport in homoepitaxial and heteroepitaxial metal growth*, Phys. Rev. Lett. **75**(4), 677 – 680 (1995).

[BC94] G. S. Bales and D. C. Chrzan, *Dynamics of irreversible island growth during submonolayer epitaxy*, Phys. Rev. B **50**(9), 6057 – 6067 (1994).

[BE92] M. C. Bartelt and J. W. Evans, *Scaling analysis of diffusion-mediated island growth in surface adsorption processes*, Phys. Rev. B **46**(19), 12675–12687 (1992).

[BE94] M. C. Bartelt and J. W. Evans, *Dendritic islands in metal-on-metal epitaxy: I. Shape transitions and diffusion at island edges*, Surf. Sci. **314**(1), L829 – L834 (1994).

[BE95] M. C. Bartelt and J. W. Evans, *Transition to multilayer kinetic roughening for metal (100) homoepitaxy*, Phys. Rev. Lett. **75**(23), 4250 – 4253 (1995).

[BE99] M. C. Bartelt and J. W. Evans, *Temperature dependence of kinetic roughening during metal(100) homoepitaxy: transition between 'mounding' and smooth growth*, Surf. Sci. **423**(2-3), 189 – 207 (1999).

[BGK+96] M. C. Bartelt, S. Gunther, E. Kopatzki, R. J. Behm and J. W. Evans, *Island-size distributions in submonolayer epitaxial growth: Influence of the mobility of small clusters*, Phys. Rev. B **53**(7), 4099 – 4104 (1996).

[BH86] R. J. Birgeneau and P. M. Horn, Science **232**, 329 (1986).

[BHM+96] M. Bott, M. Hohage, M. Morgenstern, T. Michely and G. Comsa, *New approach for determination of diffusion parameters of adatoms*, Phys. Rev. Lett. **76**(8), 1304 – 1307 (1996).

[BKL75] A. B. Bortz, M. H. Kalos and J. L. Lebowitz, *A New Algorithm for Monte Carlo Simulation of Ising Spin Systems*, J. Computat. Phys. **17**, 10–18 (1975).

[BMC92] M. Bott, T. Michely and G. Comsa, Surf. Sci. **272**, 161 (1992).

[BMD00] J. Buschle, P. Maass and W. Dieterich, *Exact density functionals in one dimension*, Journ. of Phys. A **33**(4), L41 – L46 (2000).

[BRRK94] H. Brune, C. Romainczyk, H. Roder and K. Kern, *Mechanism of the transition from fractal to dendritic growth of surface aggregates*, Nature **369**(6480), 469 – 471 (1994).

[Bru98] H. Brune, *Microscopic view of epitaxial metal growth: nucleation and aggregation*, Surf. Sci. Reports **31**(4-6), 121 – 229 (1998).

[BSJ+99] M. C. Bartelt, C. R. Stoldt, C. J. Jenks, P. A. Thiel and J. W. Evans, *Adatom capture by arrays of two-dimensional Ag islands on Ag(100)*, Phys. Rev. B **59**(4), 3125 – 3134 (1999).

[BvdM86] E. Bauer and J. H. v. d. Merwe, *Structure and growth of crystalline superlattices: From monolayer to superlattice*, Phys. Rev. B **33**(6), 3657–3671 (1986).

[CF05] G. K. L. Chan and R. Finken, *Time-dependent density functional theory of classical fluids*, Phys. Rev. Lett. **94**(18) (2005).

[Chi97] S. Chikazumi, *Physics of Ferromagnetism*, Oxford University Press, 2nd edition, 1997.

[CK80] A. Coniglio and W. Klein, J. Phys. A **13** (1980).

[CNH+01] J. O. Cross, M. Newville, F. Hellman, P. W. Rooney, A. L. Shapiro and V. G. Harris, *Growth induced magnetic and chemical anisotropy in $CoPt_3$ alloy films*, J. Synchrotron Rad. **8**, 880 – 882 (2001).

[CP01] C. Castellano and P. Politi, *Spatiotemporal distribution of nucleation events during crystal growth*, Phys. Rev. Lett. **8705**(5), 056102–1–4 (2001).

[CSL+01] K. J. Caspersen, C. R. Stoldt, A. R. Layson, M. C. Bartelt, P. A. Thiel and J. W. Evans, *Morphology of multilayer Ag/Ag(100) films versus deposition temperature: STM analysis and atomistic lattice-gas modeling*, Phys. Rev. B **63**(8), 085401– (2001).

[DMW00] K. De'Bell, A. B. MacIsaac and J. P. Whitehead, *Dipolar effects in magnetic thin films and quasi-two-dimensional systems*, Rev. Mod. Phys. **72**(1), 225 – 257 (2000).

[DSBSDSL02] M. De Santis, R. Baudoing-Savois, P. Dolle and M. C. Saint-Lager, *Chemical ordering in the first stages of Co-Pt film growth on Pt(111)*, Phys. Rev. B **66**(8), 085412–1–7 (2002).

[EB01] J. W. Evans and M. C. Bartelt, *Nucleation, adatom capture, and island size distributions: Unified scaling analysis for submonolayer deposition*, Phys. Rev. B **63**(23), 235408 (2001).

[EFFL94] H. J. Ernst, F. Fabre, R. Folkerts and J. Lapujoulade, *Observation of a growth instability during low-temperature molecular-beam epitaxy*, Phys. Rev. Lett. **72**(1), 112 – 115 (1994).

[EH66] G. Ehrlich and F. G. Hudda, *Atomic View of Surface Self-Diffusion: Tungsten on Tungsten*, J. Chem. Phys. **44**(3), 1039–1049 (1966).

[EV94] I. Elkinani and J. Villain, *Growth roughness and instabilities due to the schwoebel effect - a one-dimensional model*, Journ. de Physique I **4**(6), 949 – 973 (1994).

[Eva79] R. Evans, Adv. Phys. **28**, 143 (1979).

[Fei94] P. J. Feibelman, *Diffusion barrier for a Ag adatom on Pt(111)*, Surf. Sci. **313**(1-2), L801 – L805 (1994).

[Fei98] P. J. Feibelman, *Interlayer self-diffusion on stepped Pt(111)*, Phys. Rev. Lett. **81**(1), 168 – 171 (1998).

[Fei99] P. J. Feibelman, *Scaling of hopping self-diffusion barriers on fcc(100) surfaces with bulk bond energies*, Surf. Sci. **423**(2-3), 169 – 174 (1999).

[FF96] M. C. Fallis and C. Y. Fong, *Influence of multiatom interactions on the shapes and energetics of two-dimensional homoepitaxial clusters on close-packed metallic surfaces*, Phys. Rev. B **54**(15), 10869–10879 (1996).

[FM01] P. J. Feibelman and T. Michely, *Pt-dimer dissociation on Pt(111)*, Surf. Sci. **492**(1-2), L723 – L728 (2001).

[FMS03] K. A. Fichthorn, M. L. Merrick and M. Scheffler, *Nanostructures at surfaces from substrate-mediated interactions*, Phys. Rev. B **68**(4), 041404–1–4 (2003).

[FRD+98] H. P. Fischer, J. Reinhard, W. Dieterich, J. F. Gouyet, P. Maass, A. Majhofer and D. Reinel, *Time-dependent density functional theory and the kinetics of lattice gas systems in contact with a wall*, Journ. Chem. Phys. **108**(7), 3028 – 3037 (1998).

[FS00] K. A. Fichthorn and M. Scheffler, *Island nucleation in thin-film epitaxy: A first-principles investigation*, Phys. Rev. Lett. **84**(23), 5371 – 5374 (2000).

[FVCP97] C. Frontera, E. Vives, T. Castan and A. Planes, *Monte Carlo study of the growth of L1(2)-ordered domains in fcc A(3)B binary alloys*, Phys. Rev. B **55**(1), 212 – 225 (1997).

[GAG89] J. A. Glazier, M. P. Anderson and G. S. Grest, Philos. Mag. B **59**, 293 (1989), (and references therein).

[GBB+00] P. Gambardella, M. Blanc, L. Burgi, K. Kuhnke and K. Kern, *Co growth on Pt(997): from monatomic chains to monolayer completion*, Surf. Sci. **449**(1-3), 93 – 103 (2000).

[GBSB+92] Y. Gauthier, R. Baudoing-Savois, J. M. Bugnard, U. Bardi and A. Atrei, *Influence of the transition metal and of order on the composition profile of $Pt_{80}M_{20}$(111)(M=Ni,Co,Fe) alloy surfaces: LEED study of $Pt_{80}Co_{20}$(111)*, Surf. Sci. **276**, 1–11 (1992).

[GDP96] E. K. U. Gross, J. F. Dobson and M. Petersilka, *Density Functional Theory II*, volume 181 of *Topics in Current Chemistry, ed. R. F. Nalewajski*, pages 81 – 172, Springer, Berlin, 1996.

[GJ93] N. W. E. M. Gee and M. T. Johnson, *Localized Kerr study of the magnetic properties of an ultrathin epitaxial Co wedge grown on Pt(111)*, J. Appl. Phys. **73**(7), 3418–3425 (1993).

[GK01] P. Gambardella and K. Kern, *Ni growth on vicinal Pt(111): low temperature exchange and formation of ordered surface alloys*, Surf. Sci. **475**(1-3), L229 – L234 (2001).

[GMD+01] R. Gerlach, T. Maroutian, L. Douillard, D. Martinotti and H. J. Ernst, *A novel method to determine the Ehrlich-Schwoebel barrier*, Surf. Sci. **480**(3), 97 – 102 (2001).

[GPDM03] J. F. Gouyet, M. Plapp, W. Dieterich and P. Maass, *Description of far-from-equilibrium processes by mean-field lattice gas models*, Advances in Phys. **52**(6), 523 – 638 (2003).

[HA87] S. Havlin and D. B. Avraham, Adv. Phys. **36**, 695 (1987).

[Har95] S. Harris, *Kinetics of interlayer transport prior to nucleation*, Phys. Rev. B **52**(23), 16793 – 16795 (1995).

[HGdlR98] H. Huang, G. H. Gilmer and T. D. de la Rubia, *An atomistic simulator for thin film deposition in three dimensions*, J. Appl. Phys. **84**(7), 3636–3649 (1998).

[HH74] F. B. Hagedorn and B. S. Hewitt, *Growth-induced magnetic anisotropy in variously oriented epitaxial films of Sm-YIGG*, J. Appl. Phys. **45**(2), 925–928 (1974).

[HK64] P. Hohenberg and W. Kohn, *Inhomogeneous Electron Gas*, Phys. Rev. **136**(3B), B864–B871 (1964).

[HM01] S. Heinrichs and P. Maass, *Comment on "Determination of interlayer diffusion parameters for Ag/Ag(111)"*, Phys. Rev. Lett. **8714**(14), 149605 (2001).

[HM02] S. Heinrichs and P. Maass, *Influence of adatom interactions on second-layer nucleation*, Phys. Rev. B **66**(7), 073402–1–4 (2002).

[HP00] P. Hyldgaard and M. Persson, *Long-ranged adsorbate-adsorbate interactions mediated by a surface-state band*, Journ. of Phys.:Cond. Matter **12**(1), L13 – L19 (2000).

[HRM00] S. Heinrichs, J. Rottler and P. Maass, *Nucleation on top of islands in epitaxial growth*, Phys, Rev. B **62**(12), 8338 – 8359 (2000).

[HTB90] P. Hänggi, P. Talkner and M. Borkovec, *Reaction-rate theory: fifty years after Kramers*, Rev. Mod. Phys. **62**(2), 251–342 (1990).

[IOJ96] K. Iwashita, T. Oguchi and T. Jo, *Orbital and spin magnetic moments of TPt3 (T=V,Cr,Mn,Fe, and Co)*, Phys. Rev. B **54**(2), 1159 – 1162 (1996).

[Jen99] P. Jensen, *Growth of nanostructures by cluster deposition: Experiments and simple models*, Rev. Mod. Phys. **71**(5), 1695 – 1735 (1999).

[JJSN95] J. Jacobsen, K. W. Jacobsen, P. Stoltze and J. K. Norskov, *Island shape-induced transition from 2d to 3d growth for Pt/Pt(111)*, Phys. Rev. Lett. **74**(12), 2295 – 2298 (1995).

[KBE+02] N. Knorr, H. Brune, M. Epple, A. Hirstein, M. A. Schneider and K. Kern, Phys. Rev. B **65**, 115420–1–5 (2002).

[KCM98] M. Kalff, G. Comsa and T. Michely, *How sensitive is epitaxial growth to adsorbates?*, Phys. Rev. Lett. **81**(6), 1255 – 1258 (1998).

[KDF+02] M. Kessler, W. Dieterich, H. L. Frisch, J. F. Gouyet and P. Maass, *Kinetics in one-dimensional lattice gas and Ising models from time-dependent density-functional theory*, Phys. Rev. E **65**(6) (2002).

[KDM01] M. Kessler, W. Dieterich and A. Majhofer, *Monte Carlo simulation of subsurface ordering kinetics in an fcc alloy model*, Phys. Rev. B **64**(12), 125412–125421 (2001).

[KDM03] M. Kessler, W. Dieterich and A. Majhofer, *Ordering kinetics in an fcc A(3)B binary alloy model: Monte Carlo studies*, Phys. Rev. B **67**(13), 134201–134210 (2003).

[KE98] K. Kyuno and G. Ehrlich, *Step-edge barriers on Pt(III): An atomistic view*, Phys. Rev. Lett. **81**(25), 5592 – 5595 (1998).

[Kel94] G. L. Kellog, *Field ion microscope studies of single-atom surface diffusion and cluster nucleation on metal surfaces*, Surf. Sci. Rep. **21**, 1–88 (1994).

[KF69] P. W. Kasteleyn and C. M. Fortuin, J. Phys. Soc. Japan Suppl. **16**, 11 (1969).

[KG95] J. Kohlhepp and U. Gradmann, *Magnetic surface anisotropies of Co(0001)-based interfaces from in-situ magnetometry of Co films on Pd(111), covered with ultrathin films of Pd and Ag*, J. Magnet. Magn. Mater. **139**(3), 347 – 354 (1995).

[KKW98] H. Kallabis, P. L. Krapivsky and D. E. Wolf, *Island distance in one-dimensional epitaxial growth*, Europ. Phys. Journ. B **5**(3), 801 – 804 (1998).

[KLS+92] P. Krams, F. Lauks, R. L. Stamps, B. Hillebrands and G. Güntherodt, *Magnetic anisotropies of ultrathin Co(001) films on Cu(001)*, Phys. Rev. Lett. (1992).

[KPM00] J. Krug, P. Politi and T. Michely, *Island nucleation in the presence of step-edge barriers: Theory and applications*, Phys. Rev. B **61**(20), 14037 – 14046 (2000).

[KPPB+00] E. Kentzinger, V. Parasote, V. Pierron-Bohnes, J. F. Lami, M. C. Cadeville, J. M. Sanchez and R. Caudron, *Experimental determination of pair interaction energies in a CoPt3 single crystal and phase-diagram calculations*, Phys. Rev. B **61**(22), 14975 – 14983 (2000).

[KPVC90] R. Kunkel, B. Poelsema, L. K. Verheij and G. Comsa, Phys. Rev. Lett. **65**, 7333 (1990).

[Kru00] J. Krug, *Scaling regimes for second layer nucleation*, Europ. Phys. Journ. B **18**(4), 713 – 719 (2000).

[KS65] W. Kohn and L. J. Sham, *Self-Consistent Equations Including Exchange and Correlation Effects*, Phys. Rev. **140**(4A), A1133–A1138 (1965).

[KSCM99] M. Kalff, P. Smilauer, G. Comsa and T. Michely, *No coarsening in Pt(111) homoepitaxy*, Surf. Sci. **426**(3), L447 – L453 (1999).

[LÖ94] H. Löwen, *Melting, freezing and colloidal suspensions*, Phys. Rep. **237**(5), 249–324 (1994).

[LC00] T. C. Lubensky and P. M. Chaikin, *Principles of condensed matter physics*, Cambridge University Press, Cambridge [u.a.], repr. with corr. edition, 2000, P. M. Chaikin ; T. C. Lubensky.

[LdP94] Y. G. Li and A. E. de Pristo, *Potential-energy barriers for interlayer mass-transport in homoepitaxial growth on fcc(111) surfaces - Pt and Ag*, Surf. Sci. **319**(1-2), 141 – 148 (1994).

[LSK+99] E. Lundgren, B. Stanka, W. Koprolin, M. Schmid and P. Varga, *An atomic-scale study of the Co induced dendrite formation on Pt(111)*, Surf. Sci. **423**(2-3), 357 – 363 (1999).

[Lub79] T. Lubensky, *Ill Condensed Matter*, eds. R. Balian, R. Mynard and G. Toulouse, North-Holland, Amsterdam, 1979.

[LV95] J. M. M. Laren and R. H. Victoria, *Perpendicular magnetic anisotropies of (Pt/Co/Pt)/X superlattices*, Appl. Phys. Lett. **66**, 3377–3379 (1995).

[LZCM93] S. Liu, Z. Zhang, G. Comsa and H. Metiu, *Kinetic mechanism for island shape variations caused by changes in the growth temperature*, Phys. Rev. Lett. **71**(6), 2967–2970 (1993).

[Maa99] P. Maass, private communication, 1999.

[Mar96] I. Markov, *Method for evaluation of the Ehrlich-Schwoebel barrier to interlayer transport in metal homoepitaxy*, Phys. Rev. B **54**(24), 17930 – 17937 (1996).

[Mer65] N. D. Mermin, *Thermal Properties of the Inhomogeneous Electron Gas*, Phys. Rev. **137**(5A), A1441–A1443 (1965).

[MHBC93] T. Michely, M. Hohage, M. Bott and G. Comsa, *Inversion of growth speed anisotropy in two dimensions*, Phys. Rev. Lett. **70**(25), 3943–3946 (1993).

[MK04] T. Michely and J. Krug, *Islands, Mounds and Atoms*, Springer, 2004.

[MKKP99] T. Michely, M. Kalff, J. Krug and P. Politi, Phys. Blätter **55**(11), 53 (1999).

[MKWL92] Y.-W. Mo, J. Kleiner, M. B. Webb and M. G. Lagally, Surf. Sci. **268**, 275 (1992).

[MP66] F. Menzinger and A. Paoletti, *Magnetic Moments and Unpaired-Electron Densities in $CoPt_3$*, Phys. Rev. **143**(2), 365–372 (1966).

[MR00] P. A. Mulheran and D. A. Robbie, *Theory of the island and capture zone size distributions in thin film growth*, Europhys. Lett. **49**(5), 617 – 623 (2000).

[MT99] U. M. B. Marconi and P. Tarazona, *Dynamic density functional theory of fluids*, Journ. Chem. Phys. **110**(16), 8032 – 8044 (1999).

[MTM+02] A. M. Moser, K. Takano, D. T. Margulies, M. Albrecht, Y. Sonobe, Y. Ikeda, S. Sun and E. E. Fullerton, *Magnetic recording: advancing into the future*, J. Phys. D: Appl Phys. **35**, R157–R167 (2002).

[MVvdV+95] J. A. Meyer, J. Vrijmoeth, H. A. van der Vegt, E. Vlieg and R. J. Behm, *Importance of the additional step-edge barrier in determining film morphology during epitaxial-growth*, Phys. Rev. B **51**(20), 14790 – 14793 (1995).

[NB99] M. E. J. Newman and G. T. Barkema, *Monte Carlo methods in statistical physics*, Clarendon Press, Oxford [a.o.], 1999.

[NC04] M. Nastar and E. Clouet, *Mean field theories for the description of diffusion and phase transformations controlled by diffusion*, Phys. Chem., Chem. Phys. **6**(13), 3611 – 3619 (2004).

[NDM93] M. Nieswand, W. Dieterich and A. Majhofer, *Density-functional method for lattice-gas problems*, Phys. Rev. E **47**(1), 718–720 (1993).

[Née54] M. L. Néel, *Anisotropie magnetique superficielle et surstructures d'orientation*, J. de Phys. et le Radium **15**(4), 225–239 (1954).

[NKS+98] N. Nakajima, T. Koide, T. Shidara, H. Miyauchi, H. Fukutani, A. Fujimori, K. Iio, T. Katayama, M. Nývlt and Y. Suzuki, *Perpendicular Magnetic Anisotropy Caused by Interfacial Hybridisation via Enhanced Orbital Moment on Co/Pt Multilayers: Magnetic Circular X-Ray Dichroism Study*, Phys. Rev. Lett. **81**(23), 5229–5232 (1998).

[OBWL01] S. Ovesson, A. Bogicevic, G. Wahnstrom and B. I. Lundqvist, *Neglected adsorbate interactions behind diffusion prefactor anomalies on metals*, Phys. Rev. B **6412**(12) (2001).

[PAF01] M. N. Popescu, J. G. Amar and F. Family, *Rate-equation approach to island size distributions and capture numbers in submonolayer irreversible growth*, Phys. Rev. B **6420**(20), 205404–1–13 (2001).

[PC03] P. Politi and C. Castellano, *Irreversible nucleation in molecular beam epitaxy: From theory to experiments*, Phys. Rev. B **67**(7), 075408–1–10 (2003).

[Per82] J. K. Percus, J. Math. Phys. **23**, 1162 (1982).

[PF99] A. Pimpinelli and R. Ferrando, *Reentrant morphological instability of epitaxial islands*, Phys. Rev. B **60**(24), 17016 – 17022 (1999).

[PFS+03] R. Pentcheva, K. A. Fichthorn, M. Scheffler, T. Bernhard, R. Pfandzelter and H. Winter, *Non-arrhenius behavior of the island density in metal heteroepitaxy: Co on Cu(001)*, Phys. Rev. Lett. **90**(7) (2003).

[PGM+00] P. Politi, G. Grenet, A. Marty, A. Ponchet and J. Villain, *Instabilities in crystal growth by atomic or molecular beams*, Phys. Rep. **324**(5-6), 271 – 404 (2000).

[Pot52] R. B. Potts, Proc. Cambridge Philos. Soc. **48**, 106 (1952).

[PR84] M. Plischke and Z. Rácz, *Active Zone of Growing Clusters: Diffusion-Limited Aggregation and the Eden Model*, Phys. Rev. Lett. **53**(5), 415–418 (1984).

[RBBK93] H. Röder, H. Brune, J. P. Bucher and K. Kern, *Changing morphology of metallic monolayers via temperature controlled heteroepitaxial growth*, Surf. Sci. **298**(1), 121–126 (1993).

[RBT97] K. R. Roos, R. Bhutani and M. C. Tringides, *Inter-layer mass transport in a low-coverage, low island-density regime*, Surf. Sci. **384**(1-3), 62 – 69 (1997).

[RD96] D. Reinel and W. Dieterich, *Time-dependent density functional theory in lattice gas problems*, Journ. Chem. Phys. **104**(13), 5234 – 5239 (1996).

[RG84] E. Runge and E. K. U. Gross, *Density-Functional Theory for Time-Dependent Systems*, Phys. Rev. Lett. **52**(12), 997–1000 (1984).

[RM99] J. Rottler and P. Maass, *Second layer nucleation in thin film growth*, Phys. Rev. Lett. **83**(17), 3490 – 3493 (1999).

[Rot99] J. Rottler, *Wachstumsprozesse an Oberflächen und Nukleation der zweiten Lage*, Diploma thesis, Konstanz (unpublished), 1999.

[RS98] C. Ratsch and M. Scheffler, *Density-functional theory calculations of hopping rates of surface diffusion*, Phys. Rev. B **58**(19), 13163 – 13166 (1998).

[RSS97] C. Ratsch, A. P. Seitsonen and M. Scheffler, *Strain dependence of surface diffusion: Ag on Ag(111) and Pt(111)*, Phys. Rev. B **55**(11), 6750 – 6753 (1997).

[RSTH95] P. W. Rooney, A. L. Shapiro, M. Q. Tran and F. Hellman, *Evidence of a Surface-Mediated Magnetically Induced Miscibility Gap in Co-Pt Alloy Thin Films*, Phys. Rev. Lett. **75**(9), 1843–1846 (1995).

[RT98] K. R. Roos and M. C. Tringides, *Prefactor and step edge barrier determination for interlayer diffusion in homoepitaxial systems: Ag/Ag(111)*, Surf. Rev. and Lett. **5**(3-4), 833 – 840 (1998).

[RT00] K. R. Roos and M. C. Tringides, *Determination of interlayer diffusion parameters for Ag/Ag(111)*, Phys. Rev. Lett. **85**(7), 1480 – 1483 (2000).

[RZSV94] C. Ratsch, A. Zangwill, P. Smilauer and D. D. Vvedensky, *Saturation and scaling of epitaxial island densities*, Phys. Rev. Lett. **72**(20), 3194 – 3197 (1994).

[SB95] H. E. Stanley and A.-L. Barabsi, *Fractal concepts in surface growth*, Cambridge University Press, Cambridge [u.a.], 1995.

[Sch69] R. L. Schwoebel, *Step Motion on Crystal Surfaces. II*, J. Appl. Phys. **40**(2), 614–618 (1969).

[Sch98] W. Schweika, *Disordered Alloys: Diffuse Scattering and Monte Carlo Simulations*, volume 141 of *Springer Tracts in Modern Physics*, Springer, Berlin, Heidelberg, 1998.

[Sch02] T. P. Schulze, *Kinetic Monte Carlo simulations with minimal searching*, Phys. Rev. E **65**(3), 036704–1–3 (2002).

[SH95] P. Smilauer and S. Harris, *Determination of step-edge barriers to interlayer transport from surface-morphology during the initial-stages of homoepitaxial growth*, Phys. Rev. B **51**(20), 14798 – 14801 (1995).

[SK38] I. N. Stranski and L. Krastanov, Sitzungsber. Akad. Wiss. Wien **146**, 797 (1938).

[SLP98] Y. Shim, D. P. Landau and S. Pal, *Domain growth and surface roughening in Monte Carlo simulations of $A_{(0.5)}B_{(0.5)}$ film growth*, Phys. Rev. E **58**(6), 7571 – 7579 (1998).

[SM95] C. Sire and S. N. Majumdar, *Coarsening in the q-state Potts-model and the Ising-model with globally conserved magnetization*, Phys. Rev. E **52**(1), 244 – 254 (1995).

[SP94] J. A. Stroscio and D. T. Pierce, *Scaling of diffusion-mediated island growth in iron-on-iron homoepitaxy*, Phys. Rev. B **49**(12), 8522 – 8525 (1994).

[SPT] S. D. Sarma, P. Punyindu and Z. Toroczkai, *Mound formation in nonequilibrium surface growth morphology does not necessarily imply a Schwoebel instability*, e-print cond/mat 9908013 .

[SRT+99] A. L. Shapiro, P. W. Rooney, M. Q. Tran, F. Hellman, K. M. Ring, K. L. Kavanagh, B. Rellinghaus and D. Weller, *Growth-induced magnetic anisotropy and clustering in vapor-deposited Co-Pt alloy films*, Phys. Rev. B **60**(18), 12826 – 12836 (1999).

[SS94] R. Stumpf and M. Scheffler, *Theory of self-diffusion at and growth of Al(111)*, Phys. Rev. Lett. **72**(2), 254 – 257 (1994).

[SZSW96] Z. P. Shi, Z. Y. Zhang, A. K. Swan and J. F. Wendelken, *Dimer shearing as a novel mechanism for cluster diffusion and dissociation on metal (100) surfaces*, Phys. Rev. Lett. **76**(26), 4927 – 4930 (1996).

[TCFJ96] T. A. Tyson, S. D. Conradson, R. F. C. Farrow and B. A. Jones, *Observation of internal interfaces in $Pt_xCo_{1-x}(x \approx 0.7)$ alloy films: A likely cause of perpendicular magnetic anisotropy*, Phys. Rev. B **54**(6), R3702 – R3705 (1996).

[TvdGT94] J. Tersoff, A. W. D. van der Gon and R. M. Tromp, *Critical island size for layer-by-layer growth*, Phys. Rev. Lett. **72**(2), 266 – 269 (1994).

[UUH+02] L. Uba, S. Uba, O. Horpynyuk, V. N. Antonov and A. N. Yaresko, *Influence of the crystal structure and chemical order on the magnetic and magneto-optical properties of equiatomic CoPt alloy*, J. Appl. Phys. **91**(2), 775 – 779 (2002).

[Vak04] V. G. Vaks, *Kinetics of phase separation and ordering in alloys*, Phys. Rep. **391**(3-6), 157 – 242 (2004).

[vdVvPL+92] H. A. van der Vegt, H. M. van Pinxteren, M. Lohmeier, E. Vlieg and J. M. C. Thornton, *Surfactant-induced layer-by-layer growth of Ag on Ag(111)*, Phys. Rev. Lett. **68**(22), 3335–3338 (1992).

[VSH84] J. A. Venables, G. D. T. Spiller and M. Hanbücken, Rep. Prog. Phys. **47**, 399 (1984).

[VSMH01] D. Vasumathi, A. L. Shapiro, B. B. Maranville and F. Hellman, *Growth-induced perpendicular magnetic anisotropy and clustering in Ni_xPt_{1-x} alloys*, J. Magnet. Magn. Mater. **223**(3), 221 – 232 (2001).

[vSWV93] P. ˇ Smilauer, M. R. Wilby and D. D. Vvedensky, *Reentrant layer-by-layer growth: A numerical study*, Phys. Rev. B **47**(7), 4119–4122 (1993).

[VVM+94] J. Vrijmoeth, H. A. Vandervegt, J. A. Meyer, E. Vlieg and R. J. Behm, *Surfactant-induced layer-by-layer growth of ag on Ag(111) - origins and side-effects*, Phys. Rev. Lett. **72**(24), 3843 – 3846 (1994).

[VW26] M. Volmer and A. Weber, Z. Phys. Chem. (Leipzig) **119**, 277 (1926).

[WBG+92] D. Weller, H. Brändle, G. Gorman, C.-J. Lin and H. Notarys, *Magnetic and magneto-optical properties of cobalt-platinum alloys with perpendicular magnetic anisotropy*, Appl. Phys. Lett. **61**(22), 2726–2728 (1992).

[WE91] S.-C. Wang and G. Ehrlich, *Atom incorporation at surface clusters: An atomic view*, Phys. Rev. Lett. **67**(18), 2509–2512 (1991).

[WKA86] P. O. Weir, J. M. Kosterlitz and S. H. Adachi, *Non-universality in the dynamics of the one-dimensional Potts model*, J. Phys. A: Math. Gen. **19**, L757–L759 (1986).

[WLF91] R. Wu, C. Li and A. Freeman, *Structural, electronic and magnetic properties of Co/Pd(111) and Co/Pt(111)*, J. Magnet. Magn. Mater. (1991).

[Wu82] F. Y. Wu, *The Potts model*, Rev. Mod. Phys. **54**(1), 235–268 (1982).

[WWS+94] D. Weller, Y. Wu, J. Stohr, M. G. Samant, B. D. Hermsmeier and C. Chappert, *Orbital magnetic-moments of Co in multilayers with perpendicular magnetic-anisotropy*, Phys. Rev. B **49**(18), 12888 – 12896 (1994).

[YDA+97] S. H. Yang, D. A. Drabold, J. B. Adams, P. Ordejón and K. Glassford, *Density functional studies of small platinum clusters*, J. Phys.: Condens. Matter **9**(5), L39 – L45 (1997).

[ZGGF89] W. B. Zeper, F. J. A. M. Greidanus, P. F. Garcia and C. R. Fincher, *Perpendicular magnetic anisotropy and magneto-optical Kerr effect of vapor deposited Co/Pt-layered structures*, J. Appl. Phys. **65**(12), 4971–4975 (1989).

[ZL94] Z. Zhang and M. G. Lagally, *Atomic-scale mechanisms for surfactant-mediated layer-by-layer growth in homoepitaxy*, Phys. Rev. Lett. **72**(5), 693–696 (1994).